Search for isovector giant monopole resonances

Omslag: Japans karakter (uitspraak 'kyō' of 'hibiki') voor echo, vibratie of geluid, zodanig geschreven dat het een continue echo suggereert. Kalligrafie door Sue Chin Zegers-Kan.

This work was performed as part of the research program of the "Stichting voor Fundamenteel Onderzoek der Materie" (FOM), which is financially supported by the "Nederlandse Organisatie voor Wetenschappelijk Onderzoek" (NWO).

Druk: Stichting drukkerij C. Regenboog, Groningen, September 1999.

RIJKSUNIVERSITEIT GRONINGEN

SEARCH FOR ISOVECTOR GIANT MONOPOLE RESONANCES

PROEFSCHRIFT

ter verkrijging van het doctoraat in de

Wiskunde en Natuurwetenschappen

aan de Rijksuniversiteit Groningen

op gezag van de

Rector Magnificus, dr. D.F.J. Bosscher,

in het openbaar te verdedigen op

maandag 8 november 1999

om 16.00 uur

door

Remco Godfried Theo Zegers

geboren op 10 juni 1972

te Gendringen

Promotor	:	Prof. Dr. M.N. Harakeh
Referent	:	Dr. S. Brandenburg
		Dr. A.M. van den Berg

Day after day, day after day,
We stuck, nor breath nor motion;
As idle as a painted ship
Upon a painted ocean.

Water, water, every where,
And all the boards did shrink;
Water, water, every where,
Nor any drop to drink.

But soon there breathed a wind on me,
Nor sound nor motion made:
Its path was not upon the sea,
In ripple or in shade.

It raised my hair, it fanned my cheek
Like a meadow-gale of spring–
It mingled strangely with my fears,
Yet it felt like a welcoming.

From 'The Rime of the Ancient Mariner' by
Samuel Taylor Coleridge (1772-1834).

aan mijn ouders

Contents

1. Introduction

The first evidence for strong resonant photoabsorption at high excitation energies in nuclei was found in the late 1930's by Bothe and Gentner who were studying absorption in various targets using a 17 MeV photon source [1]. Several years afterwards, in 1944, the first theoretical prediction of electric dipole resonances was given by Migdal [2]. This was confirmed experimentally by Baldwin and Klaiber [3] in the study of yield curves for fission using the (γ,n) reaction.

In 1948 Goldhaber and Teller described these resonances in a semi-classical, hydrodynamical model in which the proton and neutron spheres oscillate out of phase as inter-penetrating but incompressible fluids [4]. Two years later, Steinwedel and Jensen alternatively described the dipole resonance in terms of out-of-phase oscillations of compressible neutron and proton fluids [5]. The description in the hydrodynamical model gave rise to the idea that other collective oscillations of particles in the nucleus are possible and indeed many other giant resonances have been discovered since then. In section 2.1 a brief discussion of the theory behind the hydrodynamical model is given.

Elliot and Flowers [6] and Brown and Bolsterli [7] were the first to use a microscopic framework in the description of the giant resonances, by regarding the dipole resonances as a coherent superposition of one-particle, one-hole (1p-1h) transitions over a major oscillator shell with an excitation energy of $1\hbar\omega$. Since then, many advances have been made in the microscopic description, with the aim to understand and predict details of the properties of (other) giant resonances. In section 2.2 the basic ideas are discussed. Generally speaking, the giant resonances are viewed as coherent 1p-1h excitations over one or more major shells. They obtain their width via coupling to the continuum and two-particles, two-holes (2p-2h) states. The collectivity of a resonance is expressed as the fraction of exhaustion of the sum rule for the one-body operator that induces the resonance excitation. For the giant dipole resonance, this is the famous Thomas-Reiche-Kuhn sum rule [8].

The experimentally best known giant resonances are the above mentioned isovector giant dipole resonance (IVGDR) (See ref. [9] and references therein), the isoscalar giant quadrupole resonance (ISGQR) (See ref. [10] and references therein) and the isoscalar giant monopole resonance (ISGMR) (See Ref. [11] and references therein). In addition to the distinction between isoscalar and isovector modes, which refers to the in-phase and out-of-phase oscillations of the proton and the neutron fluids, respectively, also a distinction can be made based upon whether particles with a certain spin oscillate in phase or out of phase with particles with relative opposite spin. Consequently, the giant resonances are labelled electric or magnetic, respectively. Many giant resonances involving the different types of oscillations have been discovered. Excellent overviews exist and I refer to some of these [9, 11, 10, 12, 13, 14].

The focus of this work is on the isovector giant monopole resonances. For these, few experimental results are available. In the hydrodynamical model they can be described as breathing-mode oscillations. The best known breathing mode is isoscalar in nature (the above-mentioned isoscalar giant monopole resonance) and which, because of its simple structure, is an excellent tool to study nuclear compressibilities [15, 16]. For the non-spin-flip isovector giant monopole resonance (IVGMR) and its spin-flip partner, the spin-flip isovector giant monopole resonance (SIVM), different components of the nuclear matter move out of phase. For the IVGMR, protons move inward while neutrons move outward, and vice versa. In the case of the SIVM, protons with spin-down move out of phase with neutrons with spin-up and similarly neutrons with spin-down move out of phase with protons with spin-up. This is schematically displayed in figure 1.1. Since the first order of the monopole moment is constant and does not lead to intrinsic nuclear excitations, the monopole resonances are of second order. The same holds for the non-spin-flip, isoscalar giant dipole resonance (not shown in figure 1.1); in first order, it corresponds to the translational movement of the nucleus and, therefore, only in second order does such a resonance exist. The other dipole and the quadrupole giant resonances are shown in figure 1.1.

In the shell-model description, the IVGMR and SIVM correspond to collective 1p-1h excitations over two major shells ($2\hbar\omega$). Because neutrons and protons oscillate against each other in the case of isovector giant resonances, such modes are naturally excited through charge-exchange reactions. In this work the (^{3}He,t) reaction will be used for the excitation.

The main interest in studying the IVGMR and SIVM lies in the fact that they play an important role in the understanding of nuclear structure and Coulomb effects and can be linked to volume and surface symmetry energies of nuclear matter. Their strength distributions and decay properties give direct information on their microscopic structure. As an example, the spreading width of well-known isobaric analog state (IAS) is believed to be strongly influenced by the IVGMR through the mixing of states with lower isospin, due to the isospin-symmetry breaking Coulomb force (see chapter 4.4). Furthermore, by studying the influence of the asymmetry between the protons and neutrons in the oscillations of these breathing modes, more insight could be gained on the compressibility of nuclear matter [17]. This is of potential interest for the study of some astrophysical phenomena in which such asymmetries are present, for example neutron stars.

The relative contributions from the SIVM and IVGMR to the monopole cross section at high excitation energies depend on the kinematics of the specific reactions [18, 19]. At high bombarding energies ($E \geq 100$ MeV/A) isovector non-spin-flip transitions are only weakly excited (see sections 3.2.3 and 5.1.1). At lower bombarding energies, contributions from both modes are to be expected in reactions involving particles with spin, and since their strength distributions, as well as the dependence of cross section on scattering angle, are very similar, they can not be disentangled experimentally.

Success in the experimental study of the IVGMR has been achieved in π-charge-exchange reactions [20, 21, 22] and, more recently, in the ^{60}Ni(^{7}Li,^{7}Be+γ) reaction [23]. Since the π-mesons are spinless particles, spin-flip transitions are not excited in

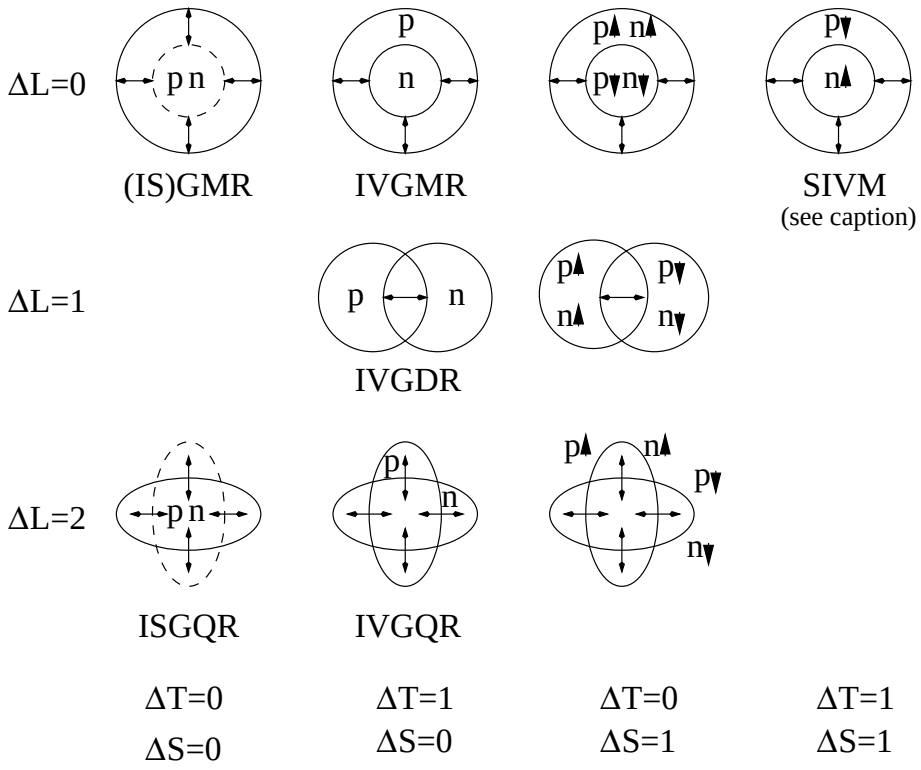

Figure 1.1: Schematic picture of giant resonances in the hydrodynamical model. The small triangles denote spin (either up or down), 'p' refers to protons and 'n' refers to neutrons. The arrows indicate the movement of the various components in each mode. Angular momentum, spin and isospin changes involved in the excitations are also indicated as well as the nomenclature as used in this thesis. For the SIVM only the out-of-phase oscillation of neutrons with spin-up and protons with spin-down is shown. A similar picture can be drawn for the out-of-phase oscillation of protons with spin-up and neutrons with spin-down. ISGQR stands for isoscalar giant quadrupole resonance and IVGQR stands for isovector giant quadrupole resonance. The other abbreviations are explained in the text.

these reactions[1]. Evidence for the presence of the IVGMR was found using the (π^-, π^0) reaction on various targets, but in the case of the (π^+, π^0) reaction, the evidence is not so convincing. By studying the (^{7}Li,^{7}Be+γ) reaction, one is able to distinguish between spin-flip and non-spin-flip modes ([24, 25], see also chapter 4.2) and in the ^{60}Ni(^{7}Li,^{7}Beγ) reaction ($T_z = (T+1)$ channel)at 60 MeV/A [23] evidence for the IVGMR was found, but no isovector spin-flip monopole strength was recovered.

Although in the ^{90}Zr(n,p) [26] and in the (^{13}C,^{13}N) reaction [27, 28, 29] structure at high excitation energies has been found that could possibly be associated with the IVGMR, conclusions with respect to multipolarity could not be drawn from the observed angular distributions and strength.

Indication for the SIVM was first found in the ^{90}Zr(^{3}He,t) reaction at bombarding energies of 600 and 900 MeV [30, 31]. Also, in the (p,n) reactions at 795 MeV on ^{90}Zr and Pb, strength was found that is consistent with a collective spin-flip isovector monopole state [32]. A more complete overview of the status of the search for the IVGMR and the SIVM will be given in chapter 4.

Microscopic calculations for the IVGMR and the SIVM have been performed in the past using a combination of Hartree-Fock theory and the random-phase approximation (RPA) [33, 34, 35, 36]. These calculations will be used for comparison with results presented in this thesis.

As will be discussed extensively in this thesis (chapters 3 and 4), the main problem of the experimental investigation of the IVGMR and SIVM is the combination of two effects: the extremely large widths of these resonances (in the order of 10 MeV) and the presence of a large underlying, non-resonant, continuum background. This continuum is largely due to quasifree processes, and in the case of reactions like (^{3}He,t), also due to breakup-pickup and pickup-breakup mechanisms. Quasifree processes are single-step charge-exchange reactions between the projectile and one of the neutrons in the target, whereas the pickup-breakup and breakup-pickup processes are two-step mechanisms. Therefore, the data from the experiments with charge-exchange reactions, and in particular the (^{3}He,t) reaction, are difficult to interpret and systematic errors in the estimation of the continuum background could lead to misinterpretation.

The main goal of the (^{3}He,t) experiments described in this thesis is to identify the IVGMR and SIVM by separating them from the continuum background by experimental means. The basic idea is the following. By requiring coincidences between ejectile tritons scattered at forward angles (since for monopole transitions the angular distributions of the ejectiles peak at zero degrees) and decay particles (protons or neutrons) emitted at backward angles from the target, one reduces the relative contributions from processes responsible for the continuum background. The tritons that are produced in the processes that contribute to the continuum, are in coincidence with high-energy, strongly forward-peaked protons and the nuclei are left in low-lying neutron-hole states, which are unlikely to decay by particle emission. Therefore, the number of coincidence events between tritons and particles emitted at backward angles, as a result of these processes, is expected to be low. Decay of the giant monopole resonances by particle emission will occur isotropically because the monopole resonances are excited with

[1] This is only true at forward angles. At backward angles, spin-flip transitions are possible due to the interaction between the spin of the target-nucleons and the pion orbital angular momentum.

transferred angular momentum $\Delta L = 0$.

In order to interpret the coincidence data, one must have a good understanding of the mechanisms involved in the decay of an excited nucleus. Statistical decay of the SIVM and IVGMR in heavy nuclei will largely occur through the emission of neutrons, since, for heavy nuclei, emission of protons via this decay mode is strongly inhibited due to the Coulomb barrier. Decay in a direct manner is, however, most likely to occur by emission of protons, which can be qualitatively understood because the SIVM and IVGMR excited in (p,n)-type reactions, such as the (^{3}He,t) reaction in the experiments discussed in this thesis can each be microscopically described as a coherent superposition of 1 proton-particle–1 neutron-hole ($1\pi p$-$1\nu h$) states. Because of the Coulomb barrier, the decay is expected to be dominated by statistical decay. Therefore, in the first experiment, the focus was on coincidences between tritons resulting from the ^{124}Sn(^{3}He,t)^{124}Sb* reaction and neutrons emitted at backward angles. This experiment was performed at Indiana University Cyclotron Facility (IUCF) in November of 1996 and will be discussed in chapter 6.

However, in the decay of ^{208}Bi, excited through the ^{208}Pb(^{3}He,t) reaction, a considerable branching ratio for the direct-decay mechanism has been reported for the Gamow-Teller resonance (GTR) [37, 38] and the spin-dipole resonance (SDR) [39] ((4.9±1.3)% and (13.4±3.9)%, respectively). Such values might also be expected for the SIVM and IVGMR since they are located even further above the Coulomb barrier. Therefore, in the second experiment, the Pb(^{3}He,t)Bi* reaction and the decay by proton emission was studied. This experiment was performed at the Kernfysisch Versneller Instituut (KVI) in May of 1998 and the results are discussed in chapter 7.

In both experiments, a magnetic spectrometer was used for the detection of the tritons at forward scattering angles. The analysis of the data depends strongly on the accurate knowledge of the optical properties of the spectrometers that were used. The methods that used for event reconstruction are, therefore, an important element in this thesis. They will be discussed in chapter 5. In that chapter also the other detection systems and experimental techniques that were used will be treated. For the experiment performed at IUCF, neutrons were detected in liquid scintillators. In the second experiment, at KVI, protons were measured in silicon solid-state detectors. To this end, the so-called 'silicon ball', was designed and constructed at the KVI. This will be further discussed in chapter 5.

2. Theory of Giant resonances

2.1 The hydrodynamical model

The simplest and most descriptive way of depicting giant resonances is through a macroscopic model in which the nucleus is described as a liquid drop which vibrates in different modes around its equilibrium shape. In fact, the theoretical explanation of the first of the giant resonances to be observed, i.e. the isovector giant dipole resonance (IVGDR), was given by Goldhaber and Teller in a macroscopic picture, in which the neutron sphere vibrates against the proton sphere [4]. In this section the hydrodynamical model will be discussed following Bohr and Mottelson [40] and Speth and Wambach [10]. However, for a proper description of the widths of the resonances, surface effects need to be included [41].

When describing vibrations of a liquid drop, two main modes can be distinguished: a surface-vibrational mode and a compressional mode. Generally speaking, a vibrating drop can have a superposition of both modes. Focusing first on the surface-vibrational mode, one usually describes the shape of the surface of a nucleus in terms of an expansion in spherical harmonics in which the normal coordinates $\alpha_{\lambda\mu}$ give the contribution of each component:

$$R(\theta,\phi) = R_0[1 + \sum_{\lambda\mu} \alpha_{\lambda\mu} Y^*_{\lambda\mu}(\theta,\phi)] \quad \lambda = 2,3,... \text{ and } \mu = -\lambda,...,+\lambda. \tag{2.1}$$

Here, R is the distance from the centre of the drop to the surface and R_0 is the equilibrium radius. The term in equation 2.1 with $\lambda = 0$ would represent a compression (or dilatation) without a change of shape, and the terms with $\lambda = 1$ would be associated with a displacement of the drop as a whole. The surface oscillations of lowest order are, therefore, the quadrupole modes ($\lambda = 2$). For the description of monopole excitations one has to add a term independent of θ and ϕ, which changes in time, leading to a breathing mode. When the amplitude is small, the Hamiltonian that describes the surface oscillation takes the relatively simple form:

$$H = \sum_{\lambda\mu} (\frac{1}{2} D_\lambda \mid \dot{\alpha}_{\lambda\mu} \mid^2 + \frac{1}{2} C_\lambda \mid \alpha_{\lambda\mu} \mid^2), \tag{2.2}$$

where D_λ and C_λ are the inertial-mass and restoring-force parameters and depend on the properties of the liquid. The oscillation of every normal mode is simply harmonic with frequency:

$$\omega_\lambda = \sqrt{\frac{C_\lambda}{D_\lambda}}. \tag{2.3}$$

The frequency can now be calculated by inserting the inertial-mass and restoring-force parameters [40]. Assuming that the nucleus consists of two inter-penetrating, incompressible fluids [4] (protons and neutrons or spin-up and spin-down particles) the restoring force must be proportional to the surface (R^2), since a relative displacement of the two components causes the two fluids not longer to overlap near the surface. Since the frequency of the resulting harmonic oscillation is proportional to the square root of force constant over mass parameter, this assumption leads to a behaviour that is linear with $R^{-1/2}$ (or linear with $A^{-1/6}$ since $R = r_0 A^{1/3}$).

The vibrations of a liquid drop can also be expressed in terms of compressional modes which describe density oscillations around the equilibrium density. If it is assumed that the nucleus is clamped, or in other words that the protons and neutrons at the surface have fixed positions with respect to each other, the motion of protons and neutrons in the nucleus will give rise to density changes. The restoring force is proportional to the density gradients. The maximum density change is linear with $1/R$ and thus the restoring force with $1/R^2$. This leads to a $1/R$ (or $A^{-1/3}$) dependence of the frequency [5].

The starting point for a more in-depth description of the compressional modes are the linearised Navier-Stokes equations. These are discussed in detail in ref. [5] and only the results for the isovector non-spin-flip modes will be given here. For the well known isovector giant dipole resonance (IVGDR), the excitation energy is given by $79A^{-1/3}$ MeV ($\lambda = 1, n = 0$). For the isovector giant monopole resonance (IVGMR), the following relation holds ($\lambda = 0, n = 1$):

$$E_x^{IVGMR} = 170A^{-1/3} \text{ MeV}. \tag{2.4}$$

Here, λ describes the multipolarity and n the number of nodes. Both the description in terms of surface oscillations and the description using compressional modes agree reasonably well with the data for the IVGDR [5, 9, 42]. Nowadays, a hybrid model, including both pictures, is applied to fit the experimental data. A systematic study of experimental results for nuclei throughout the periodic system, gives the following excitation energy of the IVGDR as a function of mass [9]:

$$E_x^{IVGDR} = 31.2A^{-1/3} + 20.6A^{-1/6} \text{ MeV}, \tag{2.5}$$

as shown in figure 2.1. (dashed line). In this figure, also the dependence as predicted by using the Navier-Stokes equations ($E_x = 79A^{-1/3}$, full line) is drawn.

Taking only the volume oscillations into account for the description of the IVGMR, one cannot reproduce the ($\pi^{\pm}, \pi^0$) data ([21, 22] see also chapter 4). Therefore, it makes sense to take into account surface effects in the description of the IVGMR, similar to the description of the IVGDR. This was done by Bowman et al. [43] using surface tension and compressibility extracted from the IVGDR. They found for the excitation energy of the IVGMR:

$$E_x^{IVGMR} = 88A^{-1/6}(1 + \frac{14}{3}A^{-1/3})^{-1/2} \text{ MeV}. \tag{2.6}$$

In figure 2.2, the systematics of excitation energy of the IVGMR as function of mass number is shown. The data points are from the π-charge-exchange reactions [21, 22].

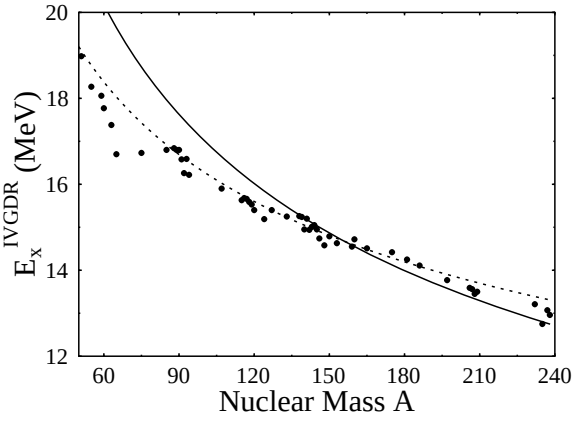

Figure 2.1: Systematics on excitation energy for the IVGDR as a function of mass number. The data is taken from reference [9]. The full line corresponds to the dependence as predicted by a description in terms of compressional modes using the linearised Navier-Stokes equations [5], i.e. $E_x = 79A^{-1/3}$ (see text). The dotted line is the result of description in terms of a combination of surface and compressional modes, equation (2.5).

The experimental results were fitted to a $A^{-1/6}$ dependency of the excitation energy with the result of $E_x = 59.2A^{-1/6}$ (dashed line in figure 2.2). In the figure also the systematics as predicted by using the linearised Navier-Stokes equations, equation (2.4), is shown (full line). The dotted line is the prediction by Bowman et al. [43], equation (2.6).

A nice feature of the macroscopic picture is that a connection to strength functions and sum rules is relatively easily established. This formalism will be discussed in more detail in the next section when discussing the microscopic approach, but it boils down to connecting a deformation of order $\lambda\mu$ to a moment of the same symmetry $\mathcal{M}(\lambda\mu)$. A multipole moment for a particular eigenmode is characterised by the oscillator strength which obeys a sum rule. Specific expressions can be found throughout the literature (e.g. [40, 44]). However, for isovector transitions one encounters the problem of having to take charge-exchange effects into account.

So far in the description of the macroscopic picture, damping of the resonances has not been discussed. This is usually taken into account by including a dissipative term in the equation of motion. It leads to complex wave numbers that depend on the mode through a viscosity coefficient, ν_τ [45]. The subscript τ refers to either an isoscalar ($\tau = 0$) or isovector mode ($\tau = 1$). Posing again the boundary conditions now leads to a set of equations that have to be solved numerically. In reference [45] the following solution for the width Γ is given:

$$\Gamma_{\lambda\tau} = \hbar\nu_\tau(a_{\lambda\tau}A^{-2/3} + b_{\lambda\tau}A^{-1/2}). \tag{2.7}$$

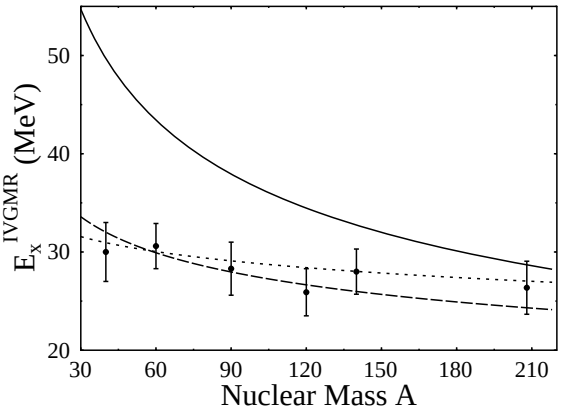

Figure 2.2: Systematics on excitation energy for the IVGMR as a function of mass number. The data is taken from references [21, 22]. The dashed line is a fit to the data, assuming an $A^{-1/6}$ dependence, with the result: $E_x = 59.2A^{-1/6}$. The full line corresponds to the dependence as predicted by a description in terms of compressional modes using the linearised Navier-Stokes equations [5], i.e. $E_x = 170A^{-1/3}$. The dotted line is the result of taking into account surface effects [43], as stated in equation (2.6).

The coefficients a and b have to be fitted to the data. For monopole excitations b is zero [45], due to the spherical symmetry of the density oscillations. Only a term proportional with the inverse of the surface of the nucleus ($R^{-1/2}$ or $A^{-2/3}$) remains.

2.2 Microscopic approach

2.2.1 Sum rules

A giant resonance is defined as a state that exhausts a large percentage of the sum rule connected with the single-particle operator that excites the state. In this section a short theoretical description of sum rules and their bearing on the IVGMR and SIVM will be given. Many good descriptions of sum rules and underlying theory can be found in the literature [10, 40, 42, 44, 46, 47]. They form the basis for the following summary.

First, a *strength function* being the response of a nucleus to an operator F is defined:

$$R_F(E) = \sum_n |< \phi_n \mid F \mid \phi_0 >|^2 \, \delta(E_n - E). \tag{2.8}$$

F connects the ground state ϕ_0 to the excited states ϕ_n. The sum turns into an integral for continuum states. One can characterise the strength by defining moments:

$$m_k(F) = \sum_n (E_n - E_0)^k \, |< \phi_n \mid F \mid \phi_0 >|^2 \quad k = 0, \pm 1, \pm 2, ... \tag{2.9}$$

Generally speaking, every odd-order moment can be rewritten in terms of the operator itself, the Hamiltonian and the ground-state wave function only [47] and so leads to a model-independent description of the strength. Usually the first-order moment is used to characterise giant resonances and is called the energy-weighted sum rule (EWSR). It can be rewritten as:

$$S_F = m_{k=1}(F) = \frac{1}{2} < \phi_0 \mid [F,[H,F]] \mid \phi_0 > . \tag{2.10}$$

Assuming the operator F to be of isoscalar type and moreover velocity-independent one can derive:

$$S_F = \frac{\hbar^2}{2m} \sum_k < \phi_0 \mid [\vec{\nabla}_k F(\vec{r_k})]^2 \mid \phi_0 > . \tag{2.11}$$

This makes it possible to explicitly write down the sum rules for certain types of interactions. This is done by expanding $F(\vec{r_k})$ in spherical multipoles:

$$F(\vec{r_k}) = \sum_{\lambda\mu} f_\lambda(\vec{r_k}) Y_{\lambda\mu}(\Omega_k) \quad \lambda = 0,1,2... \text{ and } \mu = -\lambda,...,+\lambda. \tag{2.12}$$

These resemble very much the electromagnetic transition operators and therefore the description is usually done in terms of these. In the long-wavelength limit, one finds for the electric multipole moment $\mathcal{M}$ (using a continuum charge distribution):

$$\mathcal{M}(E\lambda,\mu) = \int \rho(\vec{r}) r^\lambda Y_{\lambda\mu}(\hat{r}) d\tau, \tag{2.13}$$

If one substitutes the charge distribution $\rho(\vec{r})$ for the point-like protons:

$$\rho(\vec{r}) = \sum_{protons} e\delta(\vec{r} - \vec{r_p}), \tag{2.14}$$

and uses the isospin formalism, the electromagnetic operator can be written as:

$$\tilde{\mathcal{M}}(E\lambda,\mu) = \sum_k e[\frac{1}{2} - t_z(k)] r_k^\lambda Y_{\lambda\mu}(\Omega_k). \tag{2.15}$$

Here:

$$\begin{aligned} t_z \mid p > &= -\frac{1}{2} \mid p > \quad \text{and} \\ t_z \mid n > &= +\frac{1}{2} \mid n > . \end{aligned} \tag{2.16}$$

In equation (2.15) an isovector part, proportional to t_z, and an isoscalar part can be distinguished. The monopole and the isoscalar dipole transitions are special cases since in first order the long-wavelength limit does not give rise to an excitation, so the second term must be included. Taking only this second order term, one finds for the monopole case:

$$\tilde{\mathcal{M}}(E0) = \sum_k e[\frac{1}{2} - t_z(k)] r_k^2. \tag{2.17}$$

Using the above formalism, explicit sum rules can be derived for various types of transitions. For electric isoscalar operators, this can be done using a form factor description [44]. Charge-exchange contributions do not play a role in that case and that makes the calculations relatively simple. Including magnetic transitions requires taking the magnetic transition operators $\tilde{\mathcal{M}}(B\lambda)$ into account. For the SIVM and IVGMR in charge-exchange reactions sum rules have only been developed in a microscopic framework as described in the next section.

2.2.2 Microscopic description including charge exchange

In the present work the isovector giant monopole resonances are studied using a charge-exchange reaction; therefore, transitions with a change of $\Delta t_z = \pm 1$ must be included. This can only be done in microscopic calculations. Here, only the basic ideas of these calculations will be discussed. Siemens and Jensen [48] give a comprehensive overview of the different ingredients for the calculations. Detailed descriptions are, for example, given by Auerbach and Klein [33, 36], Speth et al.[10] and by Osterfeld [19].

The starting point of these calculations is the *independent-particle model* (IPM). In the IPM the nucleons move independently from each other in a mean field generated through the two-body interactions by all the particles. The ground state is determined to lowest order by filling the energetically lowest single-particle states. The Hamiltonian consists of the kinetic-energy operator, a local potential and the spin-orbit potential (charge-independent). There is also the Coulomb potential and a symmetry term (charge-dependent). Empirically, the local independent-particle potential is found to approximate a Wood-Saxon shape.

A large part of the nucleon-nucleon interactions acting on a particular nucleon is now represented by the average field which is included in the one-body part of the nuclear Hamiltonian. The *Hartree-Fock* (HF) method is then applied to determine the single-particle HF-wavefunction, so that the total energy $< \Psi \mid H \mid \Psi >$ is minimised, where Ψ is the A-body Slater determinant and H the Hamiltonian:

$$H = \sum_i \frac{p_i^2}{2m} + \frac{1}{2} \sum_{i \neq j} v(\vec{r_{ij}}). \tag{2.18}$$

It results in a set of so-called HF-equations:

$$\varepsilon_i \phi_i(\vec{r}) = -\frac{\hbar^2}{2m} \vec{\nabla}^2 \phi_i(\vec{r}) + U^D(\vec{r}) \phi_i(\vec{r}) - \int d^3\vec{r'} U^X(\vec{r}, \vec{r'}) \phi_i(\vec{r'}), \tag{2.19}$$

with U^D the local potential, being the average potential of all the particles in the nucleus:

$$U^D(\vec{r}) = \int d^3\vec{r'} V(\vec{r}, \vec{r'}) \rho(\vec{r}, \vec{r'}). \tag{2.20}$$

U^X is the non-local exchange potential, which can be seen as a correction term due to antisymmetrisation of the wave functions. The subscript i runs over all possible (occupied and unoccupied) orbits. Although in principle one could calculate the effective interaction from the bare nucleon-nucleon force (*Brueckner theory* [48]), for the

sake of simplicity, one usually writes the effective force in terms of phenomenological forces. Auerbach and Klein, whose calculations are used for comparison in this work [33, 36], use the *Skyrme* interaction, where the two-body interaction is approximated by a short-range expansion [41]. From the HF ground state one can then construct np-nh states by promoting n particles from states below the Fermi level to states above the Fermi level. The residual interactions are largely absent and the strength function of an operator F then can be written as:

$$S(\omega) = \sum_{m,i} n_i(1-n_m) \mid< m \mid F \mid i >\mid^2 \delta(\omega + \epsilon_i - \epsilon_m), \tag{2.21}$$

where n_i is the occupancy (either 0 or 1) of a certain level. For some operators the 1p-1h transition-strength functions are easy to calculate. However, to describe collective excitations like giant resonances, 1p-1h transitions need to be superposed coherently and one should take properly into account all the residual interactions.

In the RPA model the residual interaction is diagonalised in the space of the 1p-1h excitations or, in other words, it is considered to be a perturbation on the HF picture. In the HF method, one assumes that the nucleus ground state can be approximated by a single Slater determinant of single-particle orbitals. This is not the case for nuclei whose shells are not closed [19, 42] and for these nuclei modifications to the RPA have to be made.

In RPA an excited state is described by a creation operator $Q_f^\dagger$ acting on the ground state:

$$\mid f >= Q_f^\dagger \mid 0 >, \tag{2.22}$$

and the RPA groundstate itself is defined such that:

$$Q_f \mid 0 >= 0. \tag{2.23}$$

In principle, the operator $Q_f^\dagger$ should include all np-nh excitations, but in the lowest-order RPA only 1p-1h excitations are considered, and it can be explicitly written as:

$$Q_f^\dagger = \sum_{m,i} (X_{mi}^f a_m^\dagger a_i - Y_{mi}^f a_i^\dagger a_m). \tag{2.24}$$

Here, $a_m^\dagger(a_i)$ are creation (annihilation) operators. The X_{mi}^f and Y_{mi}^f give the overlap between such a state and the ground state or, in other words, the absolute squares of X_{mi}^f and Y_{mi}^f give the probability of finding the states $a_m^\dagger a_i \mid 0>$ and $a_i^\dagger a_m \mid 0>$ in the excited state $\mid f>$ [19].

In the RPA, the matrix elements become now:

$$< f \mid F \mid 0 >= \sum_{mi} [X_{mi}^f < m \mid F \mid i > + Y_{mi}^f < i \mid F \mid m >]. \tag{2.25}$$

The RPA solution consists of a superposition of many 1p-1h states. If various contributions to the transition matrix element add up coherently, one calls the excited state 'collective'. It exhausts a large part of the available strength for the operator F.

In studying open-shell nuclei the formalism becomes more complicated. This is due to the fact that pairing correlations become more important for these nuclei. In this case, one needs to minimise the ground-state energy with respect to both the HF field as described above, and with respect to the pairing field simultaneously. This means that besides p-p residual interactions, also the p-h residual interactions become important. This is the basis of the *Hartree-Fock-Bogoliubov* (HFB) method.

Using these methods one can construct sum rules and calculate the structure for the IVGMR [33] and the SIVM [36]. The calculations have been done for several nuclei. Results are described by Auerbach and Klein [33, 36] and Goeke and Speth [47]. For other resonances, many groups have performed calculations, using different two-body interactions.

In the discussion above, the final outcome of building collective RPA excitations is a discrete one. One can introduce the full complexity of the unbound-particle space by going to a so-called *continuum RPA* [49]. It is then possible to calculate the escape width $\Gamma^{\uparrow}$, i.e. the possibility that an excited particle can escape to the continuum. The escape width is related to the intrinsic width of the 1p-1h states. In fact, another contribution to the width is also taken into account in this kind of calculations. It is the so-called *Landau damping* (Δ) which arises from the energy distribution of the 1p-1h states and will cause a fragmentation of the transition strength. To calculate the full width, one also needs to consider the mixing of 1p-1h states with door-way states (2p-2h) for spreading into compound states (the spreading width $\Gamma^{\downarrow}$). It basically means that in equation (2.24) not only 1p-1h excitations are considered, but that also a second term consisting of all possible 2p-2h excitations and more complex ones must be included. However, usually only 2p-2h excitations are taken into account. This method is called the *second RPA* and was first formulated by Sawicki [50].

In chapter 4, the existing microscopic calculations which have been performed for the IVGMR and SIVM will be discussed. In the discussion of the results of the experiments performed as part of this thesis, they will be used for comparison.

3. Reaction theory and decay mechanisms.

3.1 The DWBA method

In this work, differential cross sections as a function of scattering angle are calculated using the *distorted-wave Born approximation* (DWBA). In this method the incoming particle is described as an incoming plane wave, which gets distorted by the mean field of the nucleus. The interaction between the particles of the projectile and the particles in the nucleus are described by an effective potential. The outgoing waves are spherical and are again distorted by the mean field of the nucleus. The transition matrix element, whose dependence on the outgoing amplitude of the spherical wave is linear, can thus be determined and its absolute square gives the cross section aside from some constant factors.

After a general formal approach following Jackson [51] and Satchler [52] the method will be discussed in more detail for charge-exchange reactions, extensively described by Madsen [53] and Raynal [54]. The article by Raynal forms the basis of the computer program DW81, which has been used for performing the cross-section calculations in this work.

3.1.1 General formalism

In general, to describe the scattering process one needs a time-dependent formulation. However, one can start from the time-independent Schrödinger equation, using Fermi's golden rule. The interaction is described by a potential V that depends on the relative spatial coordinates of the projectile and target but also on other coordinates, like spin and isospin. The solution must fulfil the boundary conditions that it is finite at the origin and that it has the asymptotic behaviour of an incoming plane wave and an outgoing spherical wave:

$$\psi(\mathbf{k},\mathbf{r}) \overset{r\to\infty}{\longrightarrow} \phi + f(\theta)\frac{e^{ikr}}{r}, \tag{3.1}$$

where ψ is the solution of the Schrödinger equation, $\mathbf{r}$ the spatial vector, $\mathbf{k}$ the wave vector, ϕ a plane wave ($e^{i\mathbf{k}\cdot\mathbf{r}}$), and $f(\theta)$ the scattering amplitude.

In the formal theory described here this is done by converting the Schrödinger equation into an integral equation that incorporates the boundary conditions. The time-independent Schrödinger equation:

$$(E - H_0)\psi(\mathbf{k},\mathbf{r}) = V(\mathbf{r})\psi(\mathbf{k},\mathbf{r}) \tag{3.2}$$

can be rewritten using orthogonality and closure relations into:

$$\psi(\mathbf{k},\mathbf{r}) = \int G_0(\mathbf{r},\mathbf{r}')V(\mathbf{r}')\psi(\mathbf{k},\mathbf{r}')d\mathbf{r}' \tag{3.3}$$

in which:

$$G_0(\mathbf{r},\mathbf{r}') = \frac{1}{(2\pi)^3}\int \frac{\phi(\mathbf{k}',\mathbf{r})\phi^*(\mathbf{k}',\mathbf{r}')}{E-E'}d\mathbf{k}' \tag{3.4}$$

and ϕ is the solution of the Schrödinger equation without any potential V present. E' is the energy eigenvalue of the Schrödinger equation with wave vector $\mathbf{k}'$. Adding to equation (3.3) the plane-wave solution, we obtain the general solution of equation (3.2):

$$\psi(\mathbf{k},\mathbf{r}) = \phi(\mathbf{k},\mathbf{r}) + \int G_0(\mathbf{r},\mathbf{r}')V(\mathbf{r}')\psi(\mathbf{k},\mathbf{r}')d\mathbf{r}'. \tag{3.5}$$

$G_0(\mathbf{r},\mathbf{r}')$ must now be chosen in such a way that equation (3.5) fulfils the boundary conditions. To do so, it is assumed that $V(\mathbf{r}')$ falls off rapidly with $\mid \mathbf{r}' \mid$, so that in the asymptotic region r is much larger than the values of r' which contributes to the integrand and (3.5) can be rewritten as:

$$\psi^{\pm}(\mathbf{k},\mathbf{r}) \stackrel{r\to\infty}{\longrightarrow} e^{\pm i\mathbf{k}\cdot\mathbf{r}} - \frac{\mu}{2\pi\hbar^2}\frac{e^{\pm ikr}}{r}\int e^{\mp i\mathbf{k}\cdot\mathbf{r}'}V(\mathbf{r}')\psi^{\pm}(\mathbf{k},\mathbf{r}')d\mathbf{r}', \tag{3.6}$$

where μ is the reduced mass of the projectile-target system. The '$\pm$' sign arises because besides an asymptotic solution with an outgoing spherical wave and an incoming plane wave there is also an asymptotic solution with an incoming spherical wave and an outgoing plane wave that fulfils the boundary conditions. The latter one describes the time-reversed process and is referred to as the post-form solution. In the detailed description of the charge-exchange process (section 3.1.2) the prior form will be used.

Using Greens-function techniques it is possible to write the general solution equation (3.5) in terms of operators. Identifying $G_0^{\pm}$ with the Greens function of the general solution of the Schrödinger equation with V set to zero and defining $G^{\pm}$ as the solution with V unequal to zero one finds the *Lipmann-Schwinger equation*:

$$\mid \psi^{\pm} > = \mid \phi > + G_0^{\pm}V \mid \psi^{\pm} > . \tag{3.7}$$

From the simple relations between $G_0^{\pm}$ and $G^{\pm}$ the formal solution of this equation can be found:

$$\mid \psi^{\pm} > = \mid \phi > + G^{\pm}V \mid \phi > . \tag{3.8}$$

Since we only know $G^{\pm}$ in terms of the eigenvalues of the full Hamiltonian this is not of much help. However, $G^{\pm}$ can be expanded into a series:

$$G^{\pm} = \sum_{n=0}^{\infty}(G_0^{\pm}V)^n G_0^{\pm}. \tag{3.9}$$

Using only the first term of this series in equation (3.8) gives the Born approximation to first order:

$$\mid \psi^{\pm} > = \mid \phi > + G_0^{\pm}V \mid \phi > . \tag{3.10}$$

This approximation can be interpreted as cutting off the scattering process of the wave (which is propagated by the Green's function $G_0^{\pm}$ from scattering point to scattering point) after the first scattering. Under this assumption we can define the transition operator $T^{\pm}$ as:

$$T^{\pm} = V + VG_0^{\pm}V. \tag{3.11}$$

Combining (3.10) and (3.11) and defining the transition matrix element as:

$$T_{fi} =< \phi \mid T^{+} \mid \phi >=< \phi \mid V \mid \psi^{+} >, \tag{3.12}$$

it follows that:

$$f(\theta, \phi) = \frac{-\mu}{2\pi\hbar^2} T_{fi}. \tag{3.13}$$

So far V has been taken the difference between H_0 and H. Often, and in particular for the DWBA, V is split up:

$$V = U + W. \tag{3.14}$$

This is done in such a way that the scattering problem with the potential U alone has a known solution $|\chi>$. In the case of DWBA, U describes the elastic scattering of the projectile from the target and W contains residual interactions that are not included in the average potential U. The $|\chi^{\pm}>$ are the so-called distorted waves, and, in Born approximation to first order, can be expressed as (compare with equation (3.10)):

$$\mid \chi^{\pm} >=\mid \phi > + G_U^{\pm} U \mid \phi >, \tag{3.15}$$

where G_U is the Green's function belonging to the Hamiltonian in which U is included. These can then be used in the expression of the solutions of the complete Hamiltonian, which includes W:

$$\mid \psi^{\pm} >=\mid \chi^{\pm} > + G_U^{\pm} W \mid \psi^{\pm} > . \tag{3.16}$$

The transition matrix element can now be written as:

$$T_{fi} =< \phi \mid T^{+} \mid \phi >=< \phi \mid U + W \mid \psi^{+} > . \tag{3.17}$$

After some algebra and realising that $G_U^{-} = (G_U^{+})^{\dagger}$ [51] one finds:

$$T_{fi} =< \phi \mid U \mid \chi^{+} > + < \chi^{-} \mid W \mid \psi^{+} > . \tag{3.18}$$

Usually the initial and final states are not connected by U and so the first term of 3.18 drops out, but U can still be used to determine the distorted waves $\mid \chi^{\pm} >$.

3.2 The DWBA in charge-exchange reactions

3.2.1 From formalism to cross section

Based on the general description of subsection 3.1.1, we now go into more detail for the charge-exchange reaction [53, 55]. Two-step (or more-step) processes are not taken into account and nucleons of the projectile and target are assumed to be non-identical. Moreover, target and projectile nuclei are treated equally except for the excitation process: it is inelastic for the target and elastic for the projectile. The initial and final channels have definite isospins. Also, it is assumed that the internal wave function of the projectile has zero orbital angular momentum. For the reaction:

$$projectile(p) + target(T) \longrightarrow ejectile(e) + residual(R), \tag{3.19}$$

the Hamiltonian in prior form is:

$$H = H_p + H_T + T_{pT} + V_{pT}. \tag{3.20}$$

H_p and H_T are the internal Hamiltonians for the projectile and target, T_{pT} is the kinetic energy of the relative motion of projectile and target and V_{pT} the interaction potential. Following the reasoning of subsection 3.1.1, V_{pT} is split up in two parts: U_{pT}, the distorting potential which also includes the Coulomb interaction and $W_{pT} = V_{pT} - U_{pT}$. U_{pT} can be looked upon as an average interaction for which an optical potential will be used (see subsection 3.2.4). Next, we define χ_i^- and χ_f^+ as the incoming and outgoing waves that are distorted by the mean field of the target. As such, they are solutions of the Hamiltonians containing only T and U for each of the channels.

In addition to the spatial coordinates, spin and isospin are taken into account. The following notations are used. For the target nucleus j, m_j and t_z are the quantum numbers of the single-particle shell-model states representing angular momentum, its projection and isospin projection, respectively. For the projectile the z-components are denoted as m_j' for spin and t_z' for isospin. J_i and M_i (J_f and M_f) denote total angular momentum and its projection of the target nucleus (residual nucleus). J_i', M_i', T_i' and $M_i^{T'}$ (J_f', M_f', T_f' and $M_f^{T'}$) denote total angular momentum, its projection, and isospin and its projection, respectively, for the projectile (ejectile). The parameters $\vec{r}$, $\vec{\sigma}$ and $\vec{t}$ denote spatial, spin and isospin coordinates; i and 1 label initial states; f and 2 final states. In figure 3.1 the spatial coordinates are defined. The transition matrix element can now be written as [53]:

$$T_{fi} = < \chi_f^+(\vec{k_f}, \vec{R'}) \mid F(\vec{R'}) \mid \chi_i^-(\vec{k_i}, \vec{R'}) > . \tag{3.21}$$

It consists of the incoming and outgoing distorted waves and a part that describes the interaction between the projectile and the nucleons in the target given by the form factor $F(\vec{R})$. It is the folding of the transition density, i.e. the overlap between initial and final states of the nucleus, with the projectile-nucleus interaction:

$$\begin{aligned} F(\vec{R'}) = < \Phi_{J_f}^{M_f}(\vec{r}, \vec{\sigma}, \vec{t}) \Phi_{J_f' T_f'}^{M_f' M_f^{T'}}(\vec{r'}, \vec{\sigma'}, \vec{t'}) \mid (V_{pT} - U_{pT}) \mid \\ \mid \Phi_{J_i}^{M_i}(\vec{r}, \vec{\sigma}, \vec{t}) \Phi_{J_i' T_i'}^{M_i' M_i^{T'}}(\vec{r'}, \vec{\sigma'}, \vec{t'}) > . \end{aligned} \tag{3.22}$$

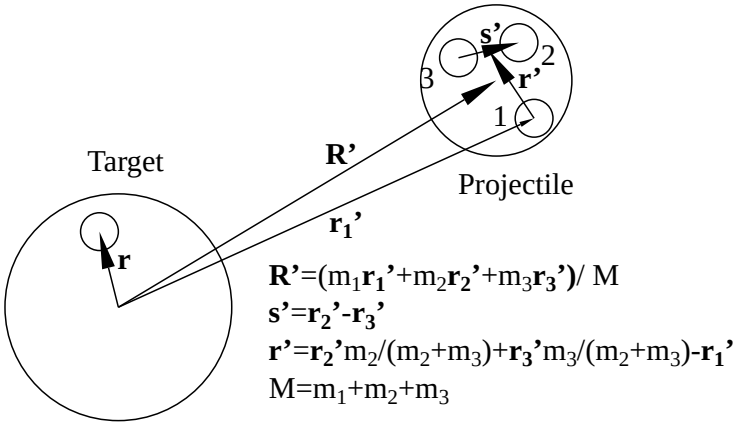

Figure 3.1: Coordinate definitions for the DWBA formalism in charge-exchange reactions.

$\Phi_J^{M_i}$ and $\Phi_{J'T'}^{M'M_i^{T'}}$ are the wave functions of target and projectile, respectively. These are eigenfunctions of the internal Hamiltonians only. Since U_{pT} is of isoscalar type, with no isospin dependence (it describes the elastic scattering), it drops out because it does not connect initial and final states in charge exchange reactions. V_{pT} represents the sum of all two-body interactions between individual projectile and target nucleons:

$$V_{pT} = \sum_{i,j} V(\mid \vec{r_i'} - \vec{r_j} \mid, \vec{\sigma_i'}, \vec{\sigma_j}, \vec{t_i'}, \vec{t_j}). \tag{3.23}$$

As already mentioned, it is assumed that the projectile carries no orbital angular momentum ($L = 0$)and so its internal wave function can be seen as a multiplication of a function depending only on spatial coordinates ($f(\vec{r_i'})$) and a function depending on spin and isospin coordinates ($\phi_{J'T'}^{M'M^{T'}}(\vec{t'}, \vec{\sigma'})$). It is then possible to express the form factor as:

$$F(\vec{R'}) = \sum_{\substack{j_1 j_2 m_1 m_2 t_{z_1} \\ t_{z_2} m'_{j_1} m'_{j_2} t'_{z_1} t'_{z_2}}} [< \Phi_{J_f}^{M_f} \phi_{J'_f T'_f}^{M'_f M_f^{T'}} \mid a^\dagger_{j_2 m_2 t_{z_2}} a_{j_1 m_1 t_{z_1}} c^\dagger_{m'_{j_2} t'_{z_2}} c_{m'_{j_1} t'_{z_1}} \mid \Phi_{J_i}^{M_i} \phi_{J'_i T'_i}^{M'_i M_i^{T'}} > \times$$
$$< \phi_{j_2 m_2 t_{z_2}}(\vec{r_1}) \phi_{m'_{j_2} t'_{z_2}} \mid V_{eff} \mid \phi_{j_1 m_1 t_{z_1}}(\vec{r_1}) \phi_{m'_{j_1} t'_{z_1}} >], \tag{3.24}$$

in which V_{eff} is the effective interaction between a projectile nucleon (at $\vec{r'}_j$) and a target nucleon (at $\vec{r}$):

$$V_{eff}(\vec{R'}, \vec{r}, \vec{\sigma}, \vec{t}, \vec{\sigma'}_j, \vec{t'}_j) = \int d\vec{r'} d\vec{s'} f_f(\vec{r'}, \vec{s'}) f_i(\vec{r'}, \vec{s'}) V(\mid \vec{r'}_j - \vec{r} \mid, \vec{\sigma}, \vec{t}, \vec{\sigma'}_j, \vec{t'}_j). \tag{3.25}$$

It describes the interaction and is only dependent on spatial coordinates. The rest of the form factor contains the information about the target and projectile; $a^\dagger$ and a are creation and annihilation operators that act on the internal target wave function to describe the interacting nucleons; $c^\dagger$ and c have a similar function for the projectile.

To actually calculate the form factor and transition matrix element a multipole expansion is used for the different components [54]. From the transition matrix element it is easy to find the differential cross section:

$$\frac{d\sigma}{d\Omega} = (\frac{\mu}{2\pi\hbar^2})^2 \frac{k_f}{k_i} \mid T_{fi} \mid^2, \tag{3.26}$$

in which k_i and k_f are the incoming and outgoing wave numbers, respectively, and μ is the reduced mass.

3.2.2 Distorted waves; the optical model

As mentioned in subsection 3.2.1 the distorted waves are solutions of the Schrödinger equation containing the kinetic energy term T and a distorting potential U:

$$(T + U)\chi = E\chi. \tag{3.27}$$

This equation has to be solved separately for the incoming and outgoing channels and so, for inelastic reactions, two different distorting potentials have to be used. The distortions are described with the so-called optical model whose parameters for a specific reaction channel are usually found experimentally, but in principle can also be calculated from the free nucleon-nucleon interaction. It is a phenomenological model that describes the interaction between target and projectile (or ejectile) [51, 52]. For ^{3}He particles and tritons with an energy of around 200 MeV the following form has been found to give good agreement with the data [56]:

$$U(r) = V_C(r) + V_0 f(x_v) + iW_0 f(x_w), \tag{3.28}$$

with V_0 and W_0 the real and imaginary well depths and $V_C(r)$ the Coulomb interaction:

$$\begin{aligned} V_C(r) &= Z_p Z_T e^2/r \quad \text{for } r > R_C, \\ V_C(r) &= Z_p Z_T e^2(3 - r^2/R_C^2)/2R_C \quad for\ r < R_C, \end{aligned} \tag{3.29}$$

where $R_C = r_C A^{1/3}$ and r_C is the reduced Coulomb radius; $f(x_i)$ is the Woods-Saxon potential:

$$f(x_n) = \frac{1}{1 + e^{x_n}} \quad \text{and} \quad x_n = (r - r_n A^{1/3})/a_n, \tag{3.30}$$

where r_n is the radius and a_n is the diffuseness. The subscript n refers to either v for the real part of the optical potential, or w for the imaginary part of the potential. Note the absence of a spin-orbit term in this particular case.

For the (^{3}He,t) reaction it was found [55, 57] that by taking the well depths for the outgoing-triton channel 85 percent of the incoming ^{3}He channel and keeping the other parameters equal to the ^{3}He parameters a good description of the data is achieved. In this thesis, the same procedure is used for determining the optical-model parameters for the triton.

3.2.3 The effective projectile-target interaction

In order to calculate T_{fi} one needs to know the effective interaction which describes the interaction between a nucleon in the target and the projectile. Generally speaking, such a calculation is very complicated because it depends on many parameters such as incident projectile energy and specific properties of the target. For every reaction the calculation should be done again starting with the free nucleon-nucleon interaction V_{NN} [19]. The effects of the nuclear medium then have to be taken into account. For high incident energies (larger than 100 MeV per nucleon) taking the free nucleon-nucleon interaction is a good approximation. One assumes that the particles in the target and in the projectile are distinguishable and the interaction is being referred to as *local*. In the energy region of interest for this work (60-70 MeV per nucleon) it is doubtful whether this is still the case. To be fully correct one would have to include non-locality effects and the interaction would have to be fully antisymmetrised for particles in the nucleus and the projectile [18]. However, throughout literature and also in this work, this is omitted.

Two-step processes have also been neglected in the present analysis. It has been shown [58] that this assumption has merely an effect on the amplitude of the interaction and not so much on the angular distribution.

The effective interaction is usually presented in the following way, where the coordinate definitions of figure 3.1 have been used. Defining the projectile density as:

$$\rho(\vec{r'}) = \int d\vec{s'} f_i(\vec{r'}, \vec{s'}) f_f(\vec{r'}, \vec{s'}), \tag{3.31}$$

the expression (3.25) changes into:

$$V_{eff}(\vec{R}, \vec{r}) = \int d\vec{r'}_j \rho(\vec{r'}_j) V_{12}(\mid \vec{r} - \vec{r'}_j \mid). \tag{3.32}$$

The free nucleon-nucleon interaction is written in a parametrised form containing central, spin-orbit and tensor parts:

$$\begin{aligned} V_{12}(r) \quad = \quad & V_0(r) + V_\sigma(r)\vec{\sigma_1} \cdot \vec{\sigma_2} + V_\tau(r)\vec{\tau_1} \cdot \vec{\tau_2} + V_{\sigma\tau}(r)(\vec{\sigma_1} \cdot \vec{\sigma_2}) \cdot (\vec{\tau_1} \cdot \vec{\tau_2}) + \\ & V_{LS}(r)(\vec{L} \cdot \vec{S}) + V_{LS\tau}(\vec{L} \cdot \vec{S}) \cdot (\vec{\tau_1} \cdot \vec{\tau_2}) + \\ & V_T(r) S_{12} + V_{T\tau}(r) S_{12}(\vec{\tau_1} \cdot \vec{\tau_2}), \end{aligned} \tag{3.33}$$

where:

$$S_{12} = \frac{(\vec{\sigma_1} \cdot \vec{r})(\vec{\sigma_2} \cdot \vec{r})}{r^2} - \vec{\sigma_1} \cdot \vec{\sigma_2}. \tag{3.34}$$

The ^{3}He-n interaction is written in the same form as the free nucleon-nucleon interaction and for doing the numerical calculations it is very convenient to express the interaction coefficients in terms of Yukawa functions: $Y(r/R) = e^{-r/R}/(r/R)$ and r^2 times these Yukawa functions. Therefore, to describe the (^{3}He,t) reaction (in which case one only keeps terms with explicit isospin dependence) we find:

$$\begin{aligned} V_{eff}(r) \quad = \quad & [V_\tau Y(r/R_\tau) + V_{\sigma\tau} Y(r/R_{\sigma\tau})(\vec{\sigma_1} \cdot \vec{\sigma_2}) \\ & + V_{LS\tau} Y(r/R_{LS\tau}) \vec{L} \cdot \vec{S} + V_{T\tau} r^2 Y(r/R_{T\tau}) S_{12}] \vec{\tau_1} \cdot \vec{\tau_2} \end{aligned} \tag{3.35}$$

Here, the subscript '1' refers to acting on a target nucleon and the subscript '2' refers to acting on the projectile. The ranges that appear in the Yukawa potentials are chosen as to reproduce the long-range one-pion exchange potential (OPEP) behaviour. Shorter-range components (arising from ρ-meson or two-pion exchange) lead, when averaged over the ^{3}He particle, to ranges near to the OPEP values [59]. Usually the effective potential is projected on the different spin-isospin states [55, 60]. Since the ^{3}He-n system only has a bound state (the ^{4}He ground state) for $S = 0$, the $V_{\sigma\tau}$ component should be of opposite sign with respect to the V_τ component, so that the central force is only active in the $S = 0$ channel, and of such magnitude that the ^{4}He ground-state binding energy (approximately 20 MeV) is reproduced [57].

For natural-parity ($\Delta\pi = (-1)^J$) non-spin-flip isovector transitions, like the IVGMR, only the V_τ and the $V_{LS\tau}$ terms remain. However, it is predicted that the $V_{LS\tau}$ term hardly contributes when the momentum transfer is low [18]. Experimental data show this is indeed the case [55, 59]. For unnatural-parity ($\Delta\pi = (-1)^{J+1}$) isovector transitions, like the SIVM, V_τ does not contribute at all. In these cases it is $V_{\sigma\tau}$ and $V_{T\tau}$ that carry most strength. The latter one cannot be neglected except if the momentum transfer is very close to 0 fm^{-1}. $V_{LS\tau}$ is again small below 1 fm^{-1} [18].

In figure 3.2 the dependence of the magnitude of the central components of the effective nucleon-nucleon force in momentum space ($v_i(q)$) on bombarding energy is shown [18] in the limit of zero momentum transfer ($\vec{q} = (\vec{k_i} - \vec{k_f}) = 0$). By performing the Fourier transformation from momentum space to configuration space, it can be checked that, in this limit the following relation holds between V_τ and $V_{\sigma\tau}$ in the Yukawa potentials (equation (3.35)) and the effective force in momentum space:

$$v_i(q = 0) = 4\pi R_i^3 V_i, \tag{3.36}$$

where V_i is either V_τ or $V_{\sigma\tau}$, R_i is the range of the corresponding Yukawa potential and $v_i(q = 0)$ is the effective force in momentum space at zero momentum transfer.

3.2.4 Wave functions

For the calculation of differential cross sections in this work, the computer code DW81 [54, 61] is used. The wave functions that are used by this code are to be projected on a 1p-1h basis. The specific particle-hole operator O^μ_{JM} for a certain type of resonance connects the initial $|0\rangle$ and final $|JM\rangle$ states. Generally speaking, one can write O^μ_{JM} as:

$$O^\mu_{JM} = r^\lambda [\vec{\sigma} \otimes \vec{Y}_L]^J_M t_\mu, \tag{3.37}$$

where $\vec{J} = \vec{L} + \vec{S}$. The term $\vec{\sigma}$ is dropped for non-spin-flip transitions. λ normally equals L, but for the IVGMR and SIVM λ equals 2. The decomposition into 1p-1h excitations is written as:

$$|JM\rangle = \sum_{ph} X^{JM}_{ph} [a^\dagger_p a_h]_{JM} |0\rangle, \tag{3.38}$$

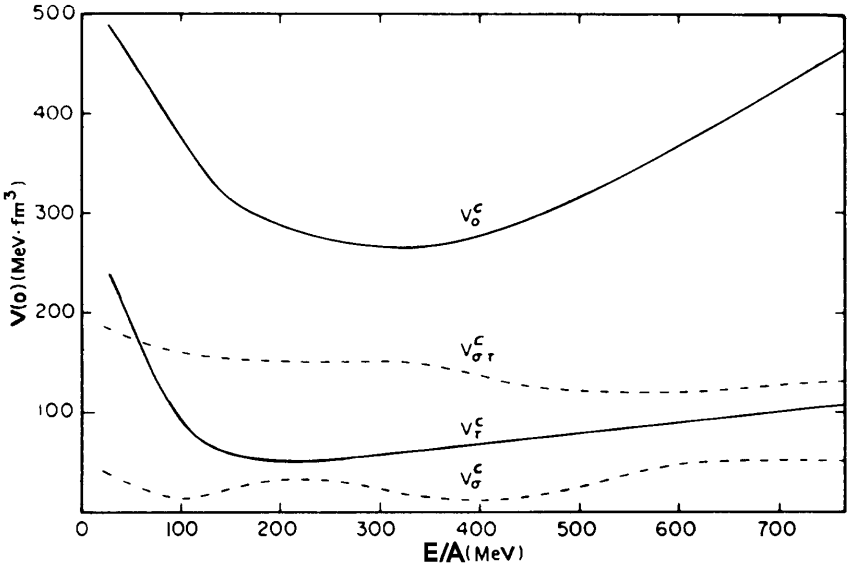

Figure 3.2: Dependence of the strength of different components of the effective force on the incoming proton energy at zero momentum transfer ($q = 0$) [18, 19]. The superscript c refers to 'central' and is omitted in the text.

where:

$$X_{ph}^{JM} = \frac{\langle JM|O_{JM}^{\mu}|0\rangle}{\sqrt{\sum_{ph}|\langle ph;JM|O_{JM}^{\mu}|0\rangle|^2}}. \tag{3.39}$$

The wave function constructed in this so-called *normal-modes formalism* [62] can be shown to exhaust the full strength associated with the operator O_{JM}^{μ} that is contained in the particle-hole basis; it exhausts 100% of the non-energy-weighted sum rule (NEWSR).

The computer code NORMOD [63] is used to construct the wave functions. The single-particle states serve as input. For open-shell nuclei one needs to take into account occupation numbers. States below the last closed shells are completely filled and the sum of occupation numbers of states above the last closed shell must be equal to the available particles. In this thesis, calculations have been done for ^{124}Sn and ^{208}Pb. For the protons, these are both closed-shell nuclei. For the neutrons, only ^{208}Pb is closed. The occupation numbers for the neutrons in ^{124}Sn are taken from the literature. One has:

$$n_j = (2j+1)V_j^2, \tag{3.40}$$

where n_j is the occupation number and V_j^2 is the fullness of a state with total angular momentum j. The following normalisation holds:

$$\sum_{j_{valence}} \frac{n_j}{N-Z} = 1, \tag{3.41}$$

i.e. the summation is over states in the valence shells only. Note that, by using the experimentally determined occupation numbers for neutron-shells in ^{124}Sn, part of the groundstate correlations are taken into account.

3.3 Decay by particle emission from excited nuclei

Since the experiments described in this work are of coincidence character it is important to understand the mechanisms involved in the decay of the target nuclei by particle emission.

3.3.1 The different decay modes

In the description of the decay mechanisms, a distinction is made between direct decay and decay after the formation of a so-called compound nucleus: statistical decay. In the direct mechanism, the excited nucleus decays by particle emission (from the first step) due to a strong overlap between the 1p-1h excited state and the ground or single-hole state of the residual nucleus coupled to a particle in the continuum. Information on the overlap of the wavefunction of the excited state and the residual state is gained from the measurement of the emitted particles. It is most interesting to study giant resonances by investigating the direct decay by particle emission, because part of the microscopic structure of the giant resonances is revealed in this way. In principle, measured branching ratios for the direct decay of a giant resonance could serve as a quantitative test of part of the wave functions that are input for microscopic calculations. The width associated with the direct-decay mechanism is called the escape width ($\Gamma^{\uparrow}$).

If the excited state couples to more complex states (2p-2h, 3p-3h,...,np-nh configurations), all the information about the initial excitation mechanism is lost. A so-called compound nucleus is formed. Decay by emission of a particle is therefore independent of the way the excited state was formed. Different decay channels will compete and emission will occur statistically. Of course, the quantum numbers must be conserved, which is reflected in the angular correlations. This statistical decay mode, for which the associated width is referred to as the spreading width ($\Gamma^{\downarrow}$) is well understood and a general formalism which forms the basis for calculations done in this work is described in the next subsection.

Decay in an intermediate or pre-equilibrium manner is also possible, but not often considered and usually included in the spreading width. If a distinction is made between decay by statistical and pre-equilibrium emission of particles (see e.g. [64]), the width associated with the first is referred to as $\Gamma^{\downarrow\downarrow}$ and the latter is referred to $\Gamma^{\downarrow\uparrow}$ [65]. Also, the fragmentation of strength due to the energy distribution of the 1p-1h states

(described by the Landau term Δ) is usually neglected in the analysis of experimental data. The total width of a giant resonance can thus be described by:

$$\Gamma_{tot} = \Gamma^{\uparrow} + \Gamma^{\downarrow} + \Delta = \Gamma^{\uparrow} + \Gamma^{\downarrow\uparrow} + \Gamma^{\downarrow\downarrow} + \Delta. \tag{3.42}$$

Microscopic theories of giant resonances, shortly discussed in the previous chapter, have been reasonably successful in the description of the various damping mechanisms. Knöpfle and Wagner [10] sum up the progress achieved by stating that the damping mechanisms of giant resonances have been included individually and are under control, but that the simultaneous treatment of escape and spreading phenomena is more difficult. Calculations on the direct decay mechanism can be found in the following references [49, 66, 67, 68, 69, 70]. On second RPA calculations, in which 2p-2h configurations have been included with the aim to explain the spreading width, excellent review articles exist [71, 72] and I refer to those and references therein. More recently, efforts have been made to describe spreading and escape widths of various resonances simultaneously. In the work by Colò et al. [73, 74, 75], this is done in a continuum RPA framework in which a set of doorway states is used to describe the basic escape and damping mechanisms, which for the IAS and the Gamow-Teller resonance (GTR) leads to satisfactory agreement with experimental results [74], but for the isoscalar and isovector monopole resonances [73, 75] the situation is less clear. The authors of references [73, 75] suggest that this is due to limited accuracies in the study of nuclear structure arising from uncertainties in the effective nuclear force and the level of approximation in treating the nuclear dynamics. Furthermore, for the isovector monopole resonances, comparison between theory and data is difficult due to the lack of experimental data. In the work by Urin et al. [76, 77, 78] the continuum RPA is extended by a phenomenological description of the doorway state coupling to many-quasiparticle configurations with reasonably good agreement for the IAS, GTR and spin-dipole resonance (SDR). Again, for the isoscalar monopole resonance the calculations are less successful. The authors attribute this to the fact that some of the parameters, that play an important role in the calculations, are not known with a sufficiently high accuracy. Calculations by the same group have been performed for the escape width of the IVGMR in ^{208}Bi [79] which will be used in the discussion of the experiments presented in this thesis.

The decay of giant resonances has been studied extensively in the past, focusing on statistical and direct decay mechanisms (see for an extensive overview reference [10]). For the decay by direct particle emission this type of studies is difficult since it is not easy to distinguish kinematically between direct decay and contributions from quasifree and breakup-pickup or pickup-breakup processes since in both cases single-hole states are populated. Still, considerable success in the experimental study of decay properties of giant resonances has been achieved (see e.g. [55, 64, 80, 81, 82, 83, 38, 84, 85]).

3.3.2 Statistical decay

This subsection will deal with the statistical decay of a compound nucleus. The computer code CASCADE [86, 87] is used for doing the statistical-decay calculations in this work.

A compound nucleus is in a quasi-stationary state and decays eventually through the emission of a nucleon (or cluster) or a de-exciting photon.

$$C^* \rightarrow b + B. \tag{3.43}$$

Of course, nucleus B may also be in an excited state forming again a compound nucleus which will decay. The lifetime of the compound nucleus is related to its width by the relation:

$$\Gamma = \hbar/\tau. \tag{3.44}$$

The theory described here is based on the Hauser-Feshbach formalism [88]. Descriptions of statistical computer codes based on this formalism are given by Pühlhofer [86] (CASCADE, which is used in this work) and Grover and Gilat [89]. The decay probabilities to the various decay channels are calculated from the statistical weight of the final states and the barrier penetrabilities. Only decay by emission of α-particles, protons, neutrons and γ-rays are considered. Other decay channels like fission or decay by emission of a deuteron are not expected to play a role in the present work but can be turned on easily in the computer-code CASCADE [86]. After doing the calculations for the initial compound nucleus, the daughter nuclei are investigated. It is assumed that no decay occurs before statistical equilibrium has been reached or in other words the memory of formation has been lost completely except for the conservation of total energy, parity and angular momentum. The energy is then distributed over all degrees of freedom.

The partial cross section for the formation of a compound nucleus of spin J and parity π from a target nucleus with spin J_T and a projectile with spin J_P is:

$$\sigma(J,\pi) = \pi\lambda^2 \frac{2J+1}{(2J_P+1)(2J_T+1)} \sum_{S=|J_P-J_T|}^{J_P+J_T} \sum_{L=|J-S|}^{J+S} T_L(E), \tag{3.45}$$

where $\vec{S}$ is the channel spin ($\vec{J_P} + \vec{J_T}$), E the centre-of-mass energy and T_L are the transmission coefficients. In the formalism they are only depending on the orbital angular momentum L and the energy. Since parity must be conserved, the summation over L is restricted by:

$$\pi = \pi_P \pi_T (-1)^L. \tag{3.46}$$

Note that equation (3.45) is not relevant when the calculation is performed for a decay cascade starting from a certain specified state (as is the case in this thesis (see chapter 7)).

The *reciprocity theorem* [51, 52] states that the amplitude for a certain process is the same as for the time-reversed process and this is invoked to calculate the particle-emission probability by detailed balance. The rate $R_x d\epsilon_x$ for the decay of a particle x from the compound nucleus (excitation energy E_1, spin J_1, parity π_1) to form the product nucleus (excitation energy E_2, spin J_2, parity π_2) is [90, 91]:

$$R_x d\varepsilon_x = \frac{1}{\hbar}\Gamma_x(\varepsilon_x) = \frac{\rho_2(E_2,J_2,\pi_2)}{2\pi\hbar\rho_1(E_1,J_1,\pi_1)} \sum_{S=|J_2-s_x|}^{J_2+s_x} \sum_{L=|J_1-S|}^{J_1+S} T_L^x(\varepsilon_x) d\varepsilon_x, \tag{3.47}$$

in which ε_x is the kinetic energy of particle x being the difference between the excitation energies of compound and daughter nuclei minus the separation energy; s_x is the spin of the emitted particle x, L its orbital angular momentum and $\vec{S}$ is the channel spin $(\vec{s}_x - \vec{J}_2)$. The transmission coefficients belonging to particle x scattering off the product nucleus are found using the optical model where average parameters are used.

A similar formula can be written down for γ-rays. In that case one uses energy-dependent strengths instead of transmission coefficients [89].

In addition to the transmission coefficients (or energy-dependent strengths) one needs the level densities for a full description of the statistical decay process. The total excitation-energy range is divided into four regions. For the lowest excitation energies (region 1), where the level density is low, experimentally known levels can be used [92]. For slightly higher energies (region 2), up to around 10 MeV, the density of levels $(\rho(E,J))$ is calculated using a *back-shifted Fermi-gas model*. This description was first introduced for lighter nuclei [93]. It differs from the conventional shifted Fermi-gas model [94] in the assumption that the shift in excitation energy because of pairing is corrected for to give a better description of the data. Since this correction is in the opposite direction from the original shift in excitation energy due to pairing it is referred to as a back shift. Here, the description by Vonach and Hille will be used [95].

The level density is given by:

$$\rho(E,J) = \frac{1}{24\sqrt{2}} \frac{(2J+1)}{\sigma^3 a^{1/4}} \frac{\exp[2(a(E-\Delta))^{1/2} - J(J+1)/(2\sigma^2)]}{(E-\Delta+t)^{5/4}}, \tag{3.48}$$

where E is the excitation energy and Δ the back-shift parameter. The thermodynamic temperature (t) is then defined by:

$$E - \Delta = at^2 - t, \tag{3.49}$$

where a is the level-density parameter and σ is the spin cut-off parameter that describes the spin distribution. At higher excitation energies this cut-off parameter approaches a value of $I_{rigid}t/\hbar^2$ [90], where I_{rigid} is the rigid-body moment of inertia $(\frac{2}{5}MR^2)$. At lower excitation energies the spin cut-off parameter may drop to 50 percent of the rigid-body value. The level-density parameter and the shift Δ are fitted to data. An extensive library of values is available [96].

Finally, if the excitation energy is very high (in this work, higher than $120 * A^{-1/3}$) it is assumed that all nuclei behave as predicted in the liquid-drop model (region 4). In this region the level-density parameter is taken $A/8$ (MeV^{-1}) and the fictive ground state (Δ) is calculated under the assumption that the virtual ground state for the level density in this region should coincide with the ground-state energy of a spherical liquid drop (i.e. including an even-odd mass term [97]). The moment of inertia, needed to find the spin dependence, is found using the deformation parameter δ. The level densities in region 3 are obtained by a smooth interpolation between regions 2 and 4.

3.4 Isospin structure

Since we are looking into reactions of isovector type, it is important to understand the isospin picture well. In figure 3.3 a schematic diagram of the states excited by the

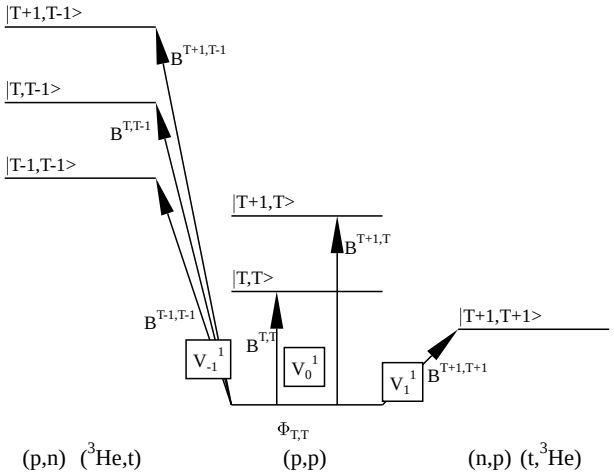

Figure 3.3: Isospin picture of excited states. $\Phi_{T,T}$ refers to the target-nucleus whose isospin and its projection on the z-axis equal T. The B's are the excitation strengths for the different isospin components and the V's refer to different isovector monopole operators (see text).

isovector monopole operator (denoted V^1_μ for this moment) is shown. $\mu = -1$ refers to a change of the z component (t_z) of the isospin by -1 and thus refers to (p,n)-type reactions. Similarly, $\mu = 0$ refers to no change in t_z ((p,p')-type) and $\mu = 1$ refers to a change of t_z with +1, ((n,p)-type). In figure 3.4 an abstract schematic of the different reactions belonging to the different operators is given.

Since the isovector monopole operator can only create states with isospin equal to or higher than the z-component of the target-nucleus isospin, there is only one possible transition in the $\mu = 1$ case, and in the $\mu = 0$ case only two. Clearly, if the excess of neutrons is high, as is the case for heavier nuclei, the phase space for V^1_1 transitions becomes small. This channel is thus preferably studied in lighter nuclei.

One can write the excitation strength B for the different isospin components in terms of reduced transition matrix elements h^{T+1}, h^T and h^{T-1}, thereby taking out the explicit dependence on the isospin quantum numbers. One finds [42, 98]:

$$B^{T+1,T-1} = \frac{|h^{T+1}|^2}{(T+1)(2T+1)}, \qquad B^{T+1,T} = \frac{|h^{T+1}|^2}{T+1}, \qquad B^{T+1,T+1} = \mid h^{T+1} \mid^2,$$

$$B^{T,T-1} = \frac{|h^T|^2}{T+1}, \qquad B^{T,T} = \frac{T}{T+1} \mid h^T \mid^2,$$

$$B^{T-1,T-1} = \frac{2T-1}{2T+1} \mid h^{T-1} \mid^2 . \tag{3.50}$$

It is evident that for reactions of (p,n)-type, states with isospin (T-1) carry most of the isovector strength followed by, respectively, T-states and (T+1)-states. One can estimate macroscopically the reduced transition probabilities in terms of the mass (A),

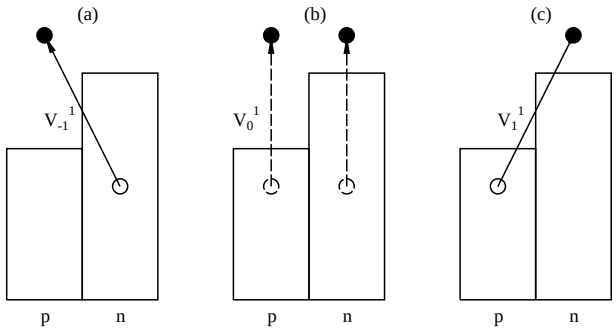

Figure 3.4: p-h excitations induced by (a) V^1_{-1}, (b) V^1_0 and (c) V^1_1 isovector monopole operators. The dashed lines in (b) indicate either a proton or a neutron makes the transition.

isospin (T) and charge (Z) using a simple operator mechanism where it is assumed that the lower moments of proton and neutron distributions are equal [98]. This leads to an additional bias with respect to component with different isospin (in ^{208}Pb, one finds, $h^{T+1} : h^T : h^{T-1} \approx 0.8 : 1.0 : 1.2$). Combining these results with equations (3.50) one finds for nuclei with large neutron excess:

$$B^{T,T} \gg B^{T+1,T} \quad \text{and} \quad B^{T-1,T-1} \gg B^{T,T-1} \gg B^{T+1,T-1}. \tag{3.51}$$

The transition to the $\mid T-1, T-1 >$ state is usually indicated with $T_<$ and the one to the $\mid T, T-1 >$ state with $T_>$. So for heavy nuclei, most strength will go to the $T_<$ state.

Focusing now on the V^1_{-1} transitions, one finds that the levels with different isospin have different excitation energies. This is due to the symmetry splitting, most easily described in terms of the *semi-empirical mass formula*. The difference in binding energy for states in the same nucleus having different values of T is given by the symmetry energy. In the simplest model this symmetry term goes with T^2 [99], but if one includes neutron-proton exchange interactions an additional term linear in T is also expected [42]. By fitting the parameters of the liquid-drop model for the potential energy of the nucleus to a large database of experimental values [100] this is indeed confirmed. This $T(T+1)$ dependence leads to the splitting. As shown in figure 3.3, the level with isospin equal to $T-1$ is lowest in excitation energy.

From this picture it is easy to understand the reason why the widths of the IVGMR and SIVM in a V^1_{-1}-type of transition are large. Most strength will go into the $T_<$ state (for heavy nuclei) and since this will be embedded in a region with a high density of 2p-2h states with equal isospin to which the IVGMR and SIVM can couple to, strength will be strongly spread (i.e. the spreading width is large).

Besides the symmetry term also the Coulomb energy term, giving the energy difference between *isobaric analog states* (same isospin T, but different T_z) is of importance. It describes the interaction between a proton and the other protons in the nucleus

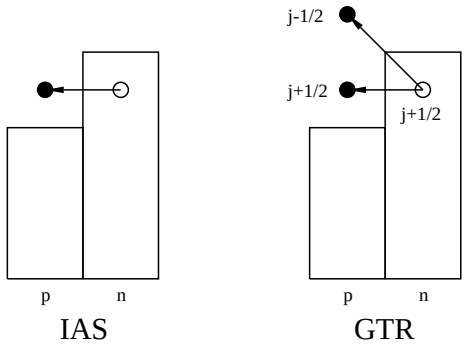

Figure 3.5: p-h configuration of IAS (left) and GTR (right). In the latter case, the total angular momenta are indicated.

leading to a term with a $Z(Z-1)$ dependence [42]. The Coulomb interaction does not conserve isospin and is partly responsible for the width of the *Isobaric Analog State* (IAS) since it causes mixing between the IAS and the IVGMR (see chapter 4).

3.5 Comparison of the IVGMR with the IAS

The structure of the IVGMR is very similar to that of the IAS. Focusing on the $t_z = -1$ channel, the transition that transforms the target ground state into the isobaric analog state basically leaves the wave function intact and merely exchanges a neutron for a proton, as schematically depicted in figure 3.5. There is no spin-flip involved and there is no change in angular momentum. A very simple model-independent sum rule exists for the IAS [101]:

$$S_{\beta^-} - S_{\beta^+} = (N - Z). \tag{3.52}$$

If the initial state has good isospin the strength is concentrated in one state because of isospin conservation (this is not really true, see section 4.4) and S_{β^+} has to vanish.

The main difference with the IVGMR is that, for the IVGMR, the principal quantum number of the proton is raised by one compared to the corresponding neutron making the transition in the target nucleus. The excitation energy is thus much higher but the structure is essentially the same. The angular distributions for the IAS and IVGMR are very similar and for this reason the IAS can be used as reference.

Using the excitation energies of the IVGMR calculated from the hydrodynamical model or RPA calculations and the energy of the symmetry term, one can write down for the excitation energy of the $T_<$ component of the IVGMR with respect to the IAS [40]:

$$E_x^{IVGMR}(T-1) - E_x^{IAS}(T) = V_0 A^{-1/3} - (T+1)V_1 A^{-1}, \tag{3.53}$$

where the constants V_0 and V_1 depend on the model used.

A similar comparison exists between the GTR and the SIVM. In these cases, spin-flip is also involved. Most of the GT strength is concentrated in $T_< = T - 1$ states and thus has a large width since it is surrounded with states of equal isospin $(T - 1)$. The appearance in the excitation energy spectra is therefore less pronounced than the IAS. As will be shown later, the angular distributions of the GTR and SIVM have a similar shape as those of the IAS and IVGMR, since also $L = 0$ transfer is involved, but are somewhat flatter due to the coupling with spin.

3.6 Contributions from the GTR at high excitation energies

The GTR is located in excitation energy somewhat above the IAS (by approximately 0.5 MeV in ^{208}Bi) and has a width of about 4 MeV in heavy mass nuclei. In figure 3.5, the GTR is schematically depicted. Due to the spin-flip, a neutron in an orbit with total angular momentum $(j + 1/2)$ is exchanged for a proton in an orbit with total angular momentum $(j - 1/2)$ or $(j + 1/2)$. The GTR has been studied extensively using the (p,n) reaction, predominantly at IUCF [102, 103] at 200 MeV, but also in the (^{3}He,t) reaction. The GTR was first predicted by Ikeda, Fujii and Fujita [101]. They developed a model-independent sum rule for the GTR similar to that of the IAS:

$$S_{\beta^-}(GT) - S_{\beta^+}(GT) = 3(N - Z). \tag{3.54}$$

In this case, however, S_{β^+} is non-vanishing, but in heavy nuclei it will be very small because of Pauli-blocking. In contrast to the IAS, only around 60% of the sum-rule strength has been discovered in the low excitation-energy region [103]. It has been proposed that this quenching of the GT-strength at low excitation energies is due to shifting of GT-strength to higher excitation energies. Two mechanisms are suggested to describe this effect.

The first one is the admixture of the $\Delta(1232)$-isobar nucleon-hole (Δ-h) into the 1p-1h GT state resulting in a part of the GT-strength being moved to the Δ-excitation energy region [104]. This would invalidate the above sum rule and part of the strength would then be located at $\sim$300 MeV excitation energy. In this case, no interference with the IVGMR or SIVM would be expected.

The second mechanism to describe the quenching was put forward by the Tokyo group [105, 106, 107], who claim that it is caused by configuration mixing. The 1p-1h states mix with 2p-2h states via the strong tensor interaction which shifts the strength to excitation energies of up to 50 MeV, i.e. including the excitation-energy region of the SIVM and IVGMR. This idea was worked out in a RPA framework by Osterfeld et al. [108] who showed that the Δ-isobar mechanism was not really needed to understand the spectra.

In fact, Wakasa et al. [109] reported sufficient GT strength in the excitation-energy region above the GTR bump and up to 50 MeV in ^{90}Zr to fulfil the sum rule, using a full multipole decomposition of the (p,n) spectra, suggesting evidence for the second mechanism. Although this procedure has it problems (see section 4.3), we have to

take into consideration the possibility in the present work that indeed GT strength is underlying the SIVM and IVGMR.

3.7 The continuum background in charge-exchange reactions

The problem with studying the IVGMR, or any other resonance at high excitation energies, is the presence of a large non-resonant continuum background. Generally speaking, it consists of quasifree, breakup-pickup and pickup-breakup processes. In the case of quasifree processes the incoming particle as a whole interacts with one of the nucleons in the target. Focusing on the (^{3}He,t) reaction these are the one-step charge-exchange knock-on reactions:

$$^3\mathrm{He} + n \rightarrow p + t. \tag{3.55}$$

These types of processes can be differentiated from mechanisms that involve more steps in their reaction dynamics. The simplest breakup-pickup process in the (^{3}He,t)-case consists of two steps:

$$\begin{aligned} ^3\mathrm{He} &\rightarrow d + p, \\ d + n &\rightarrow t \end{aligned} \tag{3.56}$$

and similarly for the pickup-breakup mechanism:

$$\begin{aligned} ^3\mathrm{He} + n &\rightarrow \alpha^*, \\ \alpha^* &\rightarrow t + p. \end{aligned} \tag{3.57}$$

For the (^{3}He,t) reaction the mechanism of (3.57) is unlikely since the α-particle is relatively stable, as confirmed experimentally by Aarts et al. [111].

In addition to the above processes higher order processes can contribute: formation of more complex particles and their sequential breakup or mechanisms that involve two - and/or more - step excitations. Depending on the reaction studied and parameters such as incoming energy and scattering angle, the relative contributions from different components will change. Because of the large number of channels and many degrees of freedom only few systematic studies have been attempted.

Aarts et al. [110, 111] studied the reaction mechanisms in ^{3}He-induced projectile-breakup at an incoming energy of 52 MeV. They used the plane-wave impulse approximation (PWIA) to describe the quasifree process where one of the proton in the projectile acts as a spectator. They concluded that the largest contribution to the continuum background is due to one-step processes between the deuteron and a neutron in the nucleus (so-called 'breakup-transfer') and that the breakup-pickup process only plays a minor role.

The same process was described phenomenologically at $E(^3\mathrm{He})$=130 MeV in references [112, 113] where it was found to have a Gaussian-like dependence on triton energy with a centroid of around 2/3 of the incoming energy and a FWHM of around

1/3 of the incoming energy. The authors concluded that the two-step process is the most important one.

Following Aarts et al., Jänecke et al. [114] estimated the breakup-pickup contribution to the total continuum background to be rather small (≈5%) and conjectured that the largest contribution stems from quasifree processes. Bergqvist et al. [115] gave a description of the continuum at medium and high incoming energies (600 MeV to 2 GeV) in terms of quasifree, one-step processes only. Prout et al. [116] reported a distinct behaviour of the quasifree-peak positions as a function of momentum transfer for (^{3}He,t) reactions compared to (p,n) reactions from which it might be concluded that indeed more complex processes do play a role and cannot be completely neglected.

Often a phenomenological description is used for the description of the total continuum background. It was first described by Erell et al. [21] for the π charge-exchange reactions and later also used in (^{3}He,t) reactions [114, 117]. For the (^{3}He,t) case it has the following form:

$$\frac{d^2\sigma}{d\Omega dE} = N\frac{1-\exp((E-E_0)/T)}{1+[(E-E_{QF})/W_L]^2}. \tag{3.58}$$

The centroid energy E_{QF} of a Lorentzian distribution is shifted relative to the energy of the free process, $E_t(free)$, by the proton binding energy S_p, the excitation energy E_{xn} of the neutron-hole state, and the Coulomb barrier B_{Coul} for the proton:

$$E_{QF} = E_t(free) - (S_p + E_{xn} + B_{Coul}). \tag{3.59}$$

The energy E_{xn} is zero only if the neutron is removed from the orbit nearest to the Fermi level. The width W_L is due to the Fermi motion inside the nucleus and the exponential term results from the Pauli blocking. The cut-off energy E_0 is given by:

$$E_0 = E_t(g.s.) - S_p. \tag{3.60}$$

T acts as a temperature parameter. When studying pronounced resonances, like the Gamow-Teller resonance or the IVGDR/SDR this description can be useful. For less pronounced resonances, however, using this description will lead to large systematic errors especially since the normalisation is more or less free to choose. Since it is chosen in such a way that it corresponds to the full cross section at high excitation energies, this procedure will lead to an overestimation of the continuum background because at high energies various resonances are expected.

Because of the poor systematic knowledge of the continuum background one is left with two options to study the extremely broad IVGMR and SIVM. One chooses a reaction in which the continuum background is relatively small in the hope that by investigating the angular behaviour one can distinguish the resonance (e.g., the π charge-exchange reactions as discussed in chapter 4), or one tries to distinguish between continuum background and resonances experimentally. The latter method forms the basis for this work. It is based on the idea that the quasifree and breakup-pickup processes both result in the ejection of a proton in the forward direction. By requiring a coincidence between the tritons and emitted particles (neutrons or protons) at backward angles, the continuum background will be separated from other processes, such as the resonant excitation of the SIVM and IVGMR.

The coincidence with neutrons is certainly more selective in this sense than the coincidence with protons. Only more complex and thus less likely processes that are part of the continuum background could lead to a coincidence between tritons at forward angles and neutrons at backward angles. The ^{3}He probes the surface of the nucleus. The quasifree reaction with a neutron could lead to a second step, in which the fast ejected proton knocks out another neutron or proton.

For the protons, both the quasifree and breakup-pickup processes result in the ejection of a fast proton. Only because the phase space for these processes gets smaller at backward angles, requiring a coincidence between tritons and backward-emitted protons leads to a distinction between the continuum background and resonances.

The behaviour of the quasifree contribution in the (^{3}He,t) reaction can be estimated in PWIA, as was done previously for the (α,α'n) reaction [80, 118]. In chapter 7, this procedure, refered to as quasifree knockout, will be used to compare with the data.

The triple differential cross section is written as:

$$\frac{\partial^3\sigma}{\partial\Omega_t\partial\Omega_p\partial E_t} = \rho P(q)\frac{\partial^2\sigma(\theta_t, E(t))}{\partial\Omega_t\partial E_t}, \tag{3.61}$$

in which ρ is the three-body phase-space kinematical factor:

$$\rho = \frac{cp_3(cp_5)^2E_3E_5E_6}{(2\pi\hbar c)^6(cp_5E_6 + E_5(cp_5 + cp_3\cos(\theta_3 - \theta_5) - cp_1\cos\theta_5))}\mathrm{MeV}^{-2}\mathrm{fm}^{-6}, \tag{3.62}$$

where c is the velocity of light and p_i is the momentum in MeV/c, θ_i is the laboratory angle and E_i is the total energy of particle i; the subscript i refer to: 1 for the incoming particle, 2 for the target nucleus, 3 for the inelastically-scattered projectile, 5 for the particle that is knocked out and 6 for the recoiling daughter nucleus. $P(q)$ is the momentum distribution in the target nucleus of the knocked-out particle. In this work it is approximated to be the square of a harmonic-oscillator wave function in momentum space as was done by Borghols et al. [80]. In the calculations performed in this thesis it is also assumed that only neutrons in the outer shells of the target nucleus take part in the process. Moreover, the charge-exchange process is also neglected.

The double-differential cross section in equation (3.61) stems from the free elastic scattering cross section of the projectile from the knocked-out particle. Although the ^{3}He(n,p)t reaction has been measured [119], no absolute calculation for the quasifree contribution in the coincidence spectra has been attempted in this work and the angular distribution of the tritons produced through the ^{3}He(n,p)t reaction is assumed to be flat near 0°.

To describe the quasifree process one uses the fact that the continuum background can not be distinguished from the sequential decay process. In the latter case, after the reaction, the nucleus is excited (E_x) and has a recoil momentum p_r. After the decay, both the remaining nucleus and the emitted proton have a momentum q_{cm} in the recoil centre-of-mass system (RCM). In the quasifree process, the incoming particle only interacts with the neutron that is knocked out and the residual nucleus after knock-out will thus have a momentum distribution opposite to that of the neutron before it was knocked out ($\vec{q}_{res} = -\vec{q}$). Since the quasifree process and sequential decay are

indistinguishable, the momentum of the residual nucleus should be the same for both processes:

$$\vec{q}_{cm} + \frac{M_{res}\vec{p}_r}{M_p + M_{res}} = -\vec{q}, \tag{3.63}$$

$$q^2 = q_{cm}^2 + p_r^2 \frac{M_{res}^2}{(M_p + M_{res})^2} + 2q_{cm}p_r \frac{M_{res}}{M_p + M_{res}} \cos(\theta_{cm}), \tag{3.64}$$

where M_{res} is the mass of the residual nucleus and M_p the mass of the knocked-out particle. θ_{cm} is the angle between $\vec{q}_{cm}$ of the emitted particle and $\vec{p}_r$. Therefore, by deriving the needed momentum of the knocked-out neutron inside the target nucleus to match the experimental observables and by calculating the probability of a neutron with such a momentum, the quasifree cross section can be obtained.

4. Status of the search for the IVGMR and SIVM

In this chapter, the current status of study of the Isovector Giant Monopole Giant Resonance (IVGMR) will be discussed. After a short overview of the theoretical work on the IVGMR, the experimental work will be reviewed.

Extensive theoretical efforts have been devoted to the description of the IVGMR, especially in the 1970's and early 1980's. In 1972 Auerbach [98] dealt with the isovector monopole strength based upon the scheme shown in figure 3.3 and equation (3.50). Hydro-dynamical calculations were done by Auerbach and Yeverechyahu in 1975 [45]. Auerbach and Klein [33, 34] presented microscopic calculations in 1983, in particular for the π charge-exchange reactions. Sum rules for different moments were calculated as well as strength distributions. An extension to these calculations was performed by Adachi and Auerbach in the same year [35]. They calculated the widths of the IVGMR for several nuclei. Since the calculations are complex, so far only closed-shell nuclei have been considered. The basic ideas of these calculations have been described in chapters 2 and 3.

For the SIVM, hydrodynamical calculations are more complex because of the spin degree of freedom. The result can be expected to be similar to that for the IVGMR, since still two fluid components take part in the vibrations: one proton spin-up, neutron spin-down component and one proton spin-down, neutron spin-up component. Auerbach and Klein performed calculations for the SIVM in the HF-RPA framework [36], concluding that the strength distributions of the IVGMR and SIVM are very much alike.

The first proposal for experimentally detecting the IVGMR was given in 1958 by Danos [120]. He suggested to use inelastic electron scattering. In fact, in 1972 Fukuda et al. [121] reported some structure in the appropriate excitation-energy region in inelastic electron scattering on ^{90}Zr. However, it was not possible to prove the monopole character. In 1983 the IVGMR was clearly established using the (π^-, π^0) reaction, triggering theoretical efforts. The results are summarised in section 4.1. After that more attempts using different reactions have been used to explore the IVGMR. They will be discussed in section 4.2.

Experimental work on the SIVM is mainly performed using the (p,n) and (^{3}He,t) reactions at high bombarding energies. The description is done using a full multipole decomposition of the experimental spectra. This will be further discussed in section 4.3.

One can also study properties of the IVGMR in an indirect manner, namely by investigating the width of the IAS. The underlying ideas and experimental results using such a method will be discussed in section 4.4.

The main problem in the experimental study of the IVGMR and SIVM is the presence of a large non-resonant continuum background as described in section 3.6. Moreover, one should also expect interference from other resonances. The isovector giant quadrupole resonance (IVGQR) is expected at approximately the same excitation energies as the IVGMR and SIVM [10]. In the π charge-exchange experiments, however, no cross section was found that could be contributed to the IVGQR even though theory predicted that a sizeable quadrupole contribution should be present [21].

The double giant dipole resonance (DGDR), expected in the same excitation-energy range as the IVGMR, has been reported in high-energy heavy-ion experiments [122, 123], in which case the Coulomb excitation is dominant over the nuclear interaction [124], and double-charge-exchange experiments ((π^+,π^-) and (π^-,π^+) reactions [125]). It is, however, not excited through the (^{3}He,t) reaction and thus does not have to be taken into account in the analysis.

4.1 Investigation of IVGMR via $(\pi^{\pm}, \pi^0)$ reactions.

In 1983 Bowman et al. reported the observation of the IVGMR using the $(\pi^{\pm}, \pi^0)$ reactions on ^{90}Zr and ^{120}Sn at an incident energy of 165 MeV at the Los Alamos Meson Physics Facility (LAMPF) [126]. Clear evidence was found in the (π^-, π^0) reaction ($\triangle T_z = +1$ transition). Evidence was less clear for the $\triangle T_z = -1$ transition, i.e. via the (π^+, π^0) reaction. Soon afterwards both transitions were more extensively studied using the same reactions and incident energy on ^{40}Ca, ^{60}Ni, ^{90}Zr, ^{120}Sn, ^{140}Ce and ^{208}Pb [20]. In 1986 the IVGMR was studied at different incident energies, namely 120 and 230 MeV [22]. These experiments were reviewed and compared with theory by Erell et al. [21], based on microscopic calculations by Auerbach, Klein and Adachi [34, 35]. An overview of the results are shown in figure 4.1. An important result was that the excitation energy as a function of mass followed $59.2A^{-1/6}$ MeV. This is considerably lower than expected from the hydrodynamical model which predicts $170A^{-1/3}$ MeV, as shown in figure 2.2.

The success in finding isovector monopole strength in π-charge-exchange reactions is due to the relatively low continuum background as compared to charge-exchange reactions induced by nuclear probes. There are two reasons for this. First of all, breakup-pickup and pickup-breakup reactions are not possible and thus do not contribute to the continuum background. Secondly, the π-particle does not carry spin. There is thus no spin-flip contribution to the continuum background.

There are also several reasons why one would expect it to be easier to find evidence for the IVGMR in reactions which have ($\triangle T_z = +1$). It is definitely the case for the π charge-exchange reactions, where the evidence for the IVGMR in the (π^-, π^0) reaction is more convincing than in the (π^+, π^0) case.

For reactions of the (n,p) type all IVGMR strength is concentrated in the $(T + 1)$ component. There is no splitting of strength to the T and $(T - 1)$ components as is the case for (p,n)-type reactions. Although the splitting is strongly reduced in heavy nuclei (equation (3.51)), a large width can still be expected because in the (p,n)-case levels are shifted up in excitation energy due to the Coulomb displacement. Since at

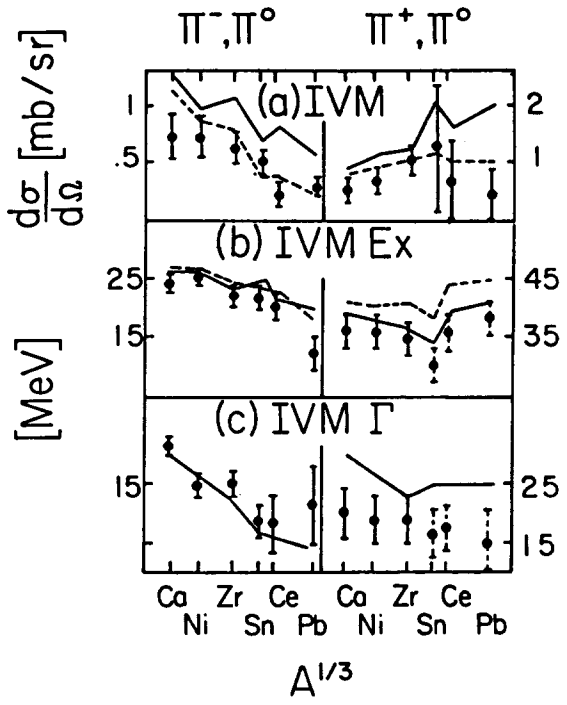

Figure 4.1: Comparison of $(\pi^{\pm}, \pi^0)$ data and theory [21]. Top: cross sections, centre: excitation energies relative to the target ground state and bottom: widths. The curves show the results of theoretical predictions (see text).

higher excitation energies the level density increases rapidly, spreading is enhanced.

Also, for the reactions with $(\triangle T_z = -1)$ one can expect more interference from the high-energy tail of the GDR. In the $(\triangle T_z = +1)$ case, transitions due to the GDR ($1\hbar\omega$ excitation) will, relatively, be stronger blocked, because of the Pauli principle, than transitions of IVGMR type which are $2\hbar\omega$ excitations.

Furthermore, since the π-mesons do not carry spin, the spin-flip giant dipole resonance (SDR) will be completely absent in the $(\pi^{\pm}, \pi^0)$ reactions. Possible interference between dipole and monopole transitions is therefore less likely, which is especially important for the $(\pi^{\pm}, \pi^0)$ reactions, since the resolution achieved is poor (6 MeV).

It must be noted that this resolution, and the phenomenological description used for the continuum background, makes the analysis of the π-charge-exchange data very difficult. Especially in the case of the (π^+, π^0) reaction conclusions on strength and position of the IVGMR [21] can be questioned.

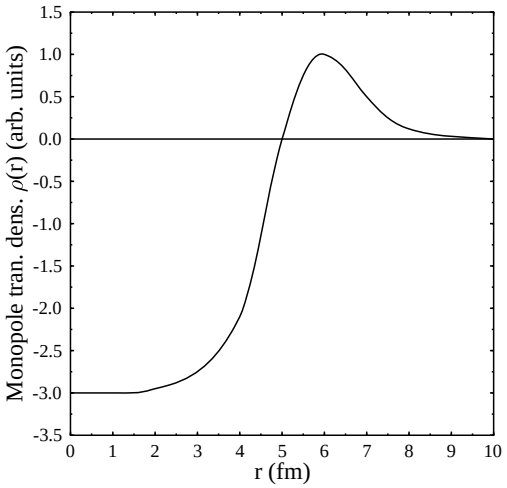

Figure 4.2: A typical shape of a breathing-mode monopole transition density [127].

4.2 Investigation of the IVGMR using other reactions.

The successes with the $(\pi^{\pm}, \pi^0)$ reaction triggered more research on the IVGMR using other reactions. In 1987 Ford et al. [26] reported resonance structures in the ^{90}Zr(n,p) reaction at 65 MeV at the excitation energy of the ($\triangle T_z = +1$) IVGMR found in the π-charge-exchange reactions. However, conclusions with respect to the multipolarity could not be drawn from the observed shape and strength.

To study the IVGMR in the $\triangle T_z = -1$ direction using the (p,n) reactions is difficult. Because the bombarding energy should be low (<60 MeV) in order to excite non-spin-flip modes rather strongly with respect to spin-flip modes, the momentum mismatch gets very high, since the IVGMR is located at high excitation energies. The cross section will thus get small compared to the continuum and other excitations. There is a second reason why one would expect to be less sensitive to monopole transitions in (p,n) reactions. The transition density of any monopole excitation has a very characteristic shape with a node near the nuclear surface as a consequence of mass conservation and the spherical symmetry of the motion [40]. Because of the opposite signs of the transition density inside and outside the nuclear surface (see figure 4.2), the volume integral will cancel for a particle that probes the entire nuclear volume. This is more so the case for protons than for light ions or heavy ions and thus protons are not the best choice to study the IVGMR. The effect is seen by comparing monopole strength in (p,n) spectra and (^{3}He,t) spectra for similar targets at the same energy per incoming

nucleon, as was done by Auerbach et al. [31, 127]. The enhancement for monopole transitions between the (^{3}He,t) and (p,n) reactions is almost a factor of ten, indicating that they are strongly excited via the former reaction and not via the latter.

Resonance structure in the excitation-energy range expected for the IVGMR have been found using the (^{13}C,^{13}N) reaction [27, 29, 28]. This reaction selects the $\Delta T_z = +1$ component. The excitation energies found for various nuclei show reasonable agreement with the (π^-, π^0) data, but as in the case of the (n,p) reaction, the shape and strength do not allow any conclusion with respect to multipolarity.

Investigating the IVGMR via reactions induced by electrons, as was first attempted by Fukuda and Torizuka [121], seems to have the disadvantage that electrons sample the entire nuclear volume, even more so than protons. The integral of the monopole transition density over the whole nucleus is reduced because of the above-mentioned cancellation effects. Also, by investigating giant resonances through inelastic electron scattering, one will excite isoscalar as well as isovector modes [10]. Furthermore, $\Delta L = 0$ and $\Delta L = 2$ transitions (as well as isoscalar $\Delta L = 1$ and $\Delta L = 3$ transitions [128]) have very similar dependence on momentum transfer, q, whereas all other L-components can be distinguished since the form factors are strongly L-dependent. Finally, a strong background due to the radiative tail of elastically-scattered electrons makes investigation of the IVGMR even more difficult.

More recently, isovector monopole resonances at high excitation energies in the $T_z = T + 1$ channel were studied using the (^{7}Li,^{7}Be) reaction [23, 24, 25]. In these experiments it is imperative to measure coincidences between the ^{7}Be ejectile and γ-rays since this provides the opportunity to distinguish between spin-flip and non-spin-flip transitions. The (^{7}Li,^{7}Be) has reaction channels to two particle-stable states; the groundstate and the first excited state at 0.43 MeV. These channels have spin-selectivities of $\Delta S = 0, 1$ and $\Delta S = 1$, respectively, and thus by measuring a coincidence between ^{7}Be and 0.43 MeV γ-rays one can separate the two channels. Indeed, isovector non-spin-flip monopole strength was found using the ^{60}Ni(^{7}Li,^{7}Be+γ) reaction. Still, interpretation was hampered due to the continuum background, possibly resulting in the failure to identify isovector spin-flip monopole strength.

4.3 Experimental investigation of the SIVM

Indication for the spin-flip partner of the IVGMR was first found in the ^{90}Zr(^{3}He,t) reaction at very high incoming energies (600 and 900 MeV) [30, 31]. At these bombarding energies, non-spin-flip transitions are very much suppressed (see figure 3.2). At excitation energies around 35 MeV (ΔS=1, ΔL=0) $J^\pi = 1^+$ strength was found consistent with $2\hbar\omega$ collective states of spin-parity 1^+ [129] that were predicted by RPA calculations performed in a complete $2\hbar\omega$ space (also calculations in $4\hbar\omega$-space were performed). The analysis was performed using a multipole decomposition of the singles spectra. The underlying idea is that all transitions in this excitation energy region, including the continuum background, can be described in a 1p-1h (and higher-order) space. All L=0 strength is then contributed to the SIVM and, possibly, high-lying Gamow-Teller strength (shifted up in energy due to the tensor interaction). Besides

the experimental difficulties to perform this kind of analysis, one can certainly argue about the validity of this procedure, since it neglects the fundamental difference between processes that are considered to be part of the continuum background and the above mentioned resonances.

Also, in the (p,n) reaction on ^{90}Zr and ^{nat}Pb at 795 MeV possible spin-flip isovector monopole strength was found [32]. Although the protons probe the nucleus as a whole, it has been argued [130] that because the interaction between a proton and the nucleus becomes stronger at higher incoming energies, observing monopole transitions at these energies using the (p,n) reaction becomes more likely. Still, in these experiments resonances could also not be distinguished from continuum background. Although a multipole analysis of the singles (p,n) spectra is more reliable than for the (^{3}He,t) reaction, since the continuum background is considerably reduced, higher-order processes in the continuum background might still interfere.

In the ^{208}Pb(n,p)^{208}Tl reaction at 458 MeV, also an indication for the SIVM was found [131], but the signal-to-noise ratio was not very good in this case and strong conclusions could not be drawn.

The SIVM, just like the IVGMR, has never been seen in (n,p) and (p,n) reactions at lower incoming energies. Still, in principle both components should contribute because V_τ and $V_{\sigma\tau}$ are of comparable size at a bombarding energy around 60 MeV.

4.4 The width of the IAS; an indirect way to study the IVGMR

Isospin is to a large extent a good quantum number. The most important reason for isospin mixing is associated with the Coulomb force between nucleons. Smaller components contributing to the symmetry breaking are the proton-neutron mass difference and charge-dependent components in the strong nucleon-nucleon interaction [42]. Especially in heavier nuclei, where the Coulomb field is relatively strong, one would expect that isobaric symmetry is strongly broken. This is not the case because the Coulomb field changes only slowly over the nuclear volume and therefore individual proton wave functions are hardly affected and the symmetry breaking is rather weak. For higher excitation energies, the breaking becomes more apparent, since more states with different isospin but with same spin and parity are closely packed together. For the IAS (with isospin T), mixing with states of lower isospin ($T-1$) of a few percent is expected [42, 132, 133].

Similar to the width of giant resonances, the width of the IAS can be seen as a combination of different components: the escape width ($\Gamma^\uparrow$), which is due to proton decay from components with $T_>(=T)$ and the spreading width ($\Gamma^\downarrow$) resulting from the mixing with states of lower isospin. For heavy nuclei the contributions from the two components are comparable [134].

The IVGMR is believed to be dominant in the mixing of states with $T_< = T-1$ into the IAS in heavier nuclei [132, 98], because the microscopic structure of the IAS and IVGMR are so similar (see section 3.5). In other words, the spreading width is directly related to the width and excitation energy of the IVGMR. Mekjian [132], Auerbach et

al. [133], MacDonald and Birse [135], and Jänecke et al. [134] describe the dependence in the following way:

$$\Gamma^{\downarrow} \approx V_{CD}^2 \frac{\Gamma_{IVGMR}}{(\Delta E)^2 + (\frac{1}{2}\Gamma_{IVGMR})^2}, \tag{4.1}$$

where V_{CD} is the charge-dependent matrix element that causes the mixing between the $T_<$ component of the IVGMR and the IAS and ΔE is the difference in excitation energy between the two and is given by equation (3.53).

Jänecke, Harakeh and Van der Werf [134] use this reasoning to obtain information about the width and excitation energy of the IVGMR by studying data from many experiments on the spreading widths of the IAS. Basically two approaches are possible to find the spreading width of the IAS. Decay of the the $T_<$ component of the IAS is dominated by statistical emission of neutrons. Measuring coincidences between the ejectile and neutrons emitted from the IAS thus gives direct information on the spreading width. Since the escape width $\Gamma^{\uparrow}$ is associated with direct decay by proton emission one could alternatively find the spreading width indirectly by subtracting the escape width found via a coincidence experiment with proton decay from the total width. The preferable method depends on the type of target [134].

By studying a large database of experimental results on the IAS, V_0 and V_1 in equation (3.53) were determined and found [134] to be in reasonable agreement with RPA calculations by Auerbach and Klein [33]. To describe the spreading width of the IAS across the mass table, including the mass regions of strong deformation, Harakeh [136] postulated a coupling between the IVGMR and the β-vibrations due to the isovector giant quadrupole resonance in deformed nuclei. To do so, a deformation parameter β is used. This induces a splitting of the IVGMR strength, thereby increasing the width of the IVGMR considerably, up to a factor of two, relative to the hydrodynamical calculation.

In conclusion, it can be said that only in the (π^-, π^0) and ^{60}Ni(^{7}Li,^{7}Be+γ) experiments evidence has been found for the $(\triangle T_z = +1)$ component of the IVGMR. Results with respect to the $(\triangle T_z = -1)$ component of the IVGMR, obtained via the (π^+, π^0) reaction are less convincing. Other attempts gave indications for resonances at the expected energies for the IVGMR but failed to reproduce the strength and angular distribution expected for the IVGMR. Several theoretical models are available that describe the strength, excitation energy and width of the IVGMR. The available data and theoretical predictions will be used in this work to predict the excitation energy and width for the current reactions studied.

Some indication for the SIVM has been found at high incoming energies using (p,n) and (^{3}He,t) reactions, but the multipole decomposition of the spectra could lead to a misinterpretation of the data because of the continuum background.

Nevertheless, the results from the (^{3}He,t) experiments at higher energies indicate that the (^{3}He,t) reaction is a good candidate to study monopole transitions. Distinguishing the continuum background from resonances by means of a coincidence measurement between tritons and neutrons and/or protons at backward angles should help

to remove the ambiguity in the analysis. This procedure forms the basis for this work.

Using heavier particles than ^{3}He to study the IVGMR, seems to have the disadvantage that more complex reaction mechanisms will start to play a role. Using the (p,n) reaction, especially at low energies, is difficult from an experimental point of view and because the proton will probe the nucleus as a whole thereby reducing the observed monopole strength because of cancellation of surface and volume terms of the integral of the monopole transition potential.

5. Experimental methods

As already discussed in previous chapters, it is a logical step to try to distinguish between genuine nuclear excitations, like the isovector monopole transitions, and quasifree and breakup-pickup processes by requiring a coincidence between the ejectile and particles emitted at backward angles (in the centre of mass). The quasifree and breakup-pickup processes will be strongly suppressed in this manner. The (^{3}He,t) reaction is a good candidate for such an experiment, since, at lower bombarding energies, it probes the breathing-mode monopole resonances strongly in comparison to (p,n) reactions and the reaction mechanism is still relatively simple compared to those of heavier-ion reactions.

In this chapter the experimental tools that are used to investigate the (^{3}He,t) reaction and the subsequent decay of the target nucleus by particle emission are treated. The first part will deal with some considerations concerning the beam energy and the production of the beam. The second part will go into more details about the detectors used and the way the data are interpreted.

For this work two experiments have been performed; the first one at *Indiana University Cyclotron Facility* (IUCF) in which the ^{124}Sn(^{3}He,t) reaction was measured in coincidence with neutrons emitted at backward angles. The experiment was performed in November of 1996. The second experiment was performed at KVI in May of 1998, where coincidences between tritons and protons were measured. The target used was ^{nat}Pb. The second part of this chapter will discuss the methods of detecting charged particles in magnetic spectrometers, focusing on ray-tracing methods and a comparison between the *K600 Spectrometer* at IUCF and the *Big-Bite Spectrometer* at KVI. After that the detectors used for detecting the decay particles will be discussed; liquid-scintillator detectors for neutron and γ-ray detection in the experiment at IUCF and silicon detectors for proton detection in the experiment at KVI.

5.1 Beam energy and production

5.1.1 Beam energy

There are two aspects that play a role when choosing an appropriate beam energy to search for isovector monopole strength. First of all, the strengths V_i of the nucleon-nucleon (NN) effective interaction (see section 3.2.3) are dependent on bombarding energy. Secondly, for monopole transitions, the momentum transfer should be as low as possible in order to have a good matching between the incoming and outgoing waves and consequently a strong excitation.

As can be seen from figure 3.2, the dependence of the effective NN interaction at zero momentum transfer ($v_i(q = 0)$) on beam energy is different for the various

components. For non-spin-flip isovector transitions, the beam energy has to be chosen as low as possible in order to have a strong excitation. For spin-flip isovector transitions, the behaviour is more or less flat. Therefore, in order to study spin-flip transitions only, a high beam energy would be appropriate.

In order to excite monopole transitions strongly, the momentum transfer must be low. This can be understood easily from a classical picture. The preferential multipole excited in a reaction is given by:

$$L = \vec{q} \times \vec{R}_{int}, \tag{5.1}$$

where ($\vec{q} = \vec{k_i} - \vec{k_f}$) and $\vec{R}_{int}$ is the interaction radius. In this argument, distortions due to Coulomb and nuclear potentials are neglected. It is clear that for a finite excitation energy choosing the beam energy as high as possible, and thus ensuring a low momentum transfer, will favour monopole transitions more.

Since the $V_{\sigma\tau}$ component of the effective potential does not change strongly as a function of bombarding energy, increasing the bombarding energy would lead to a steady increase of cross section since the momentum transfer drops. For the IVGMR, a balance must be found between the two factors. In figure 5.1 cross-section estimations are given for the IVGMR excited through the ^{208}Pb(^{3}He,t) reaction. Calculations were performed for 0° and a reasonable estimate for the IVGMR excitation energy was chosen (35 MeV). Calculations have been performed in a classical framework (using equation (5.1) and requiring that L should be lower than 0.5 to excite monopole transitions), in a plane-wave approximation and using the DWBA. The maxima of the first two are normalised to the maximum of the DWBA calculation. Optical potential parameters obtained at a bombarding energy of 217 MeV [56] were used (see also chapters 7 and 8). Therefore, deviations from the calculations at lower beam energy and higher beam energies are expected. However, the trend of the calculations shows a maximum around 200 MeV, indicating that this is the appropriate energy to investigate the IVGMR. It was therefore decided to perform the experiments around this energy (200 MeV for the experiment at IUCF and 177 MeV for the experiment at KVI).

5.1.2 Cyclotron facilities

In figure 5.2 [137] a floor plan of the experimental area at IUCF is shown. Particle acceleration at IUCF is done using a dual cyclotron setup where the first cyclotron, with a bending limit K=15 MeV (T_{max}=KZ^2/A), acts as a injector for the main (K=200 MeV) cyclotron (4 and 5 in figure 5.2). There are several experimental areas, the largest being the Electron Cooled Storage Ring (13). There is also a special section for proton-therapy eye treatment (6). The beam can be split, so that more users can work at the same time. The K600 spectrometer, used for the (^{3}He,t) experiment described in this work, is positioned at the end of a long beam line (11). A large bending magnet brings the beam into the spectrometer experimental room. The $^3He^{++}$ beam that was used to perform the experiment had an energy of 198.8 MeV.

The $^3He^{++}$ beam that was used for the experiment at KVI, was accelerated with the super-conducting cyclotron AGOR (K=600 MeV) to an energy of 177 MeV. Since July of 1996, beam is available for experiments. The extraction of a 177 $^3He^{++}$ beam

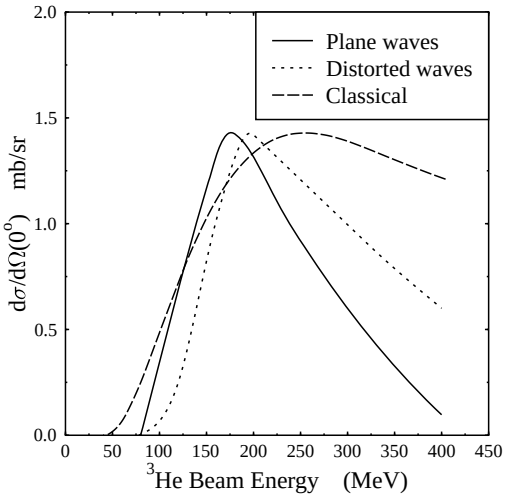

Figure 5.1: The dependence of cross section of the IVGMR in ^{208}Bi on incoming ^{3}He-energy in different approximations.

was an accomplishment in itself, since it is outside the original operating diagram of the cyclotron [138]. In figure 5.3 a floor plan of the cyclotron area and experimental areas at KVI is shown. The *Big-Bite Spectrometer* (BBS), used for the experiment, is located in the top right corner. Next to it is the *Small-Angle Large-Acceptance Detector* (SALAD). There is a separate room for radio-biological research and possibly for future proton therapy for medical treatment.

5.2 Focal-plane detectors and data interpretation

5.2.1 Ray tracing

The tritons resulting from the (^{3}He,t) reaction were detected in the focal plane of the spectrometer (either the K600 at IUCF or the BBS at KVI). To relate the measured quantities to parameters of the reaction one has to understand the optical properties of the imaging system. Generally speaking, the transfer function of an ion-optical system can be described by a transfer matrix (T) that connects parameters at the object (the target, referred to using the subscript '1') and at the image (the detection system, subscript '2'.) The matrix elements of T are the coefficients of a five-fold Taylor expansion about the central reference trajectory:

$$\alpha_1 = \sum (\alpha \mid x^{\chi}\theta^{\mu}y^{\lambda}\phi^{\nu}\delta^{\eta}) x_2^{\chi}\theta_2^{\mu}y_2^{\lambda}\phi_2^{\nu}\delta_2^{\eta}, \tag{5.2}$$

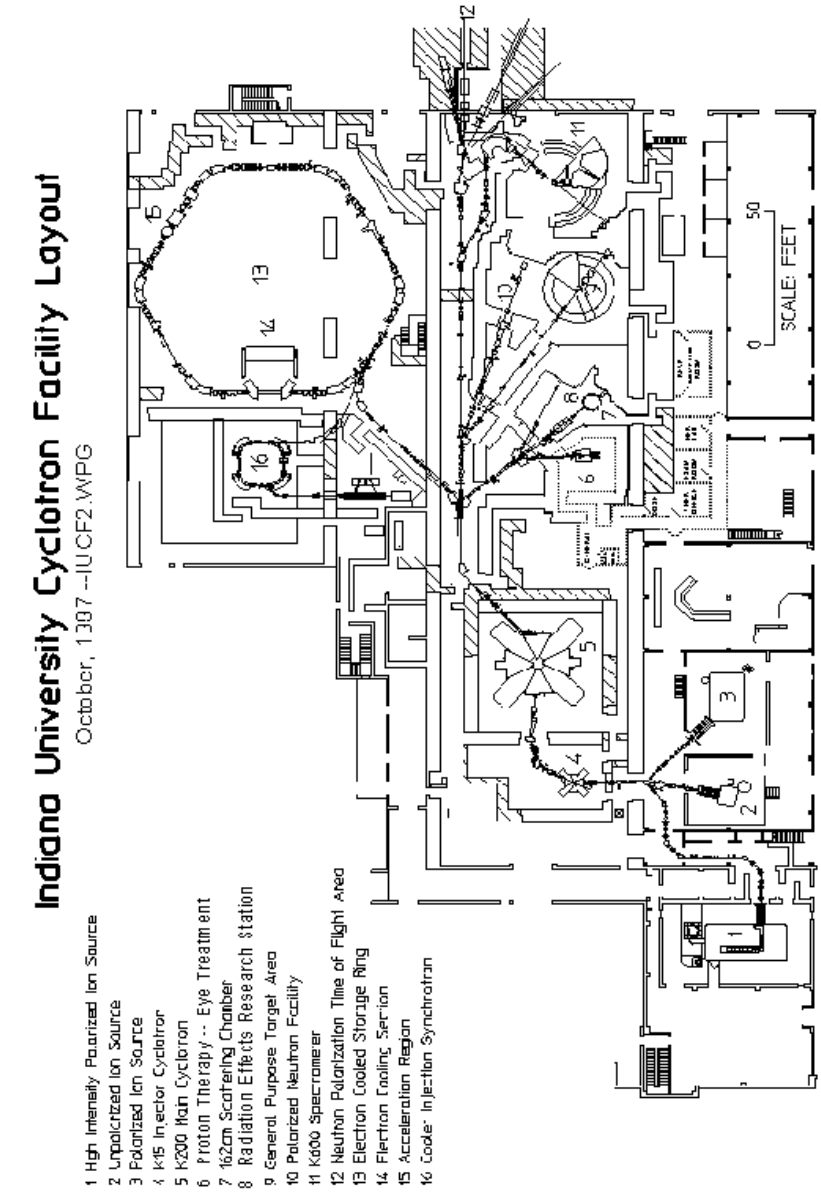

Figure 5.2: Floor plan of IUCF experimental area [137].

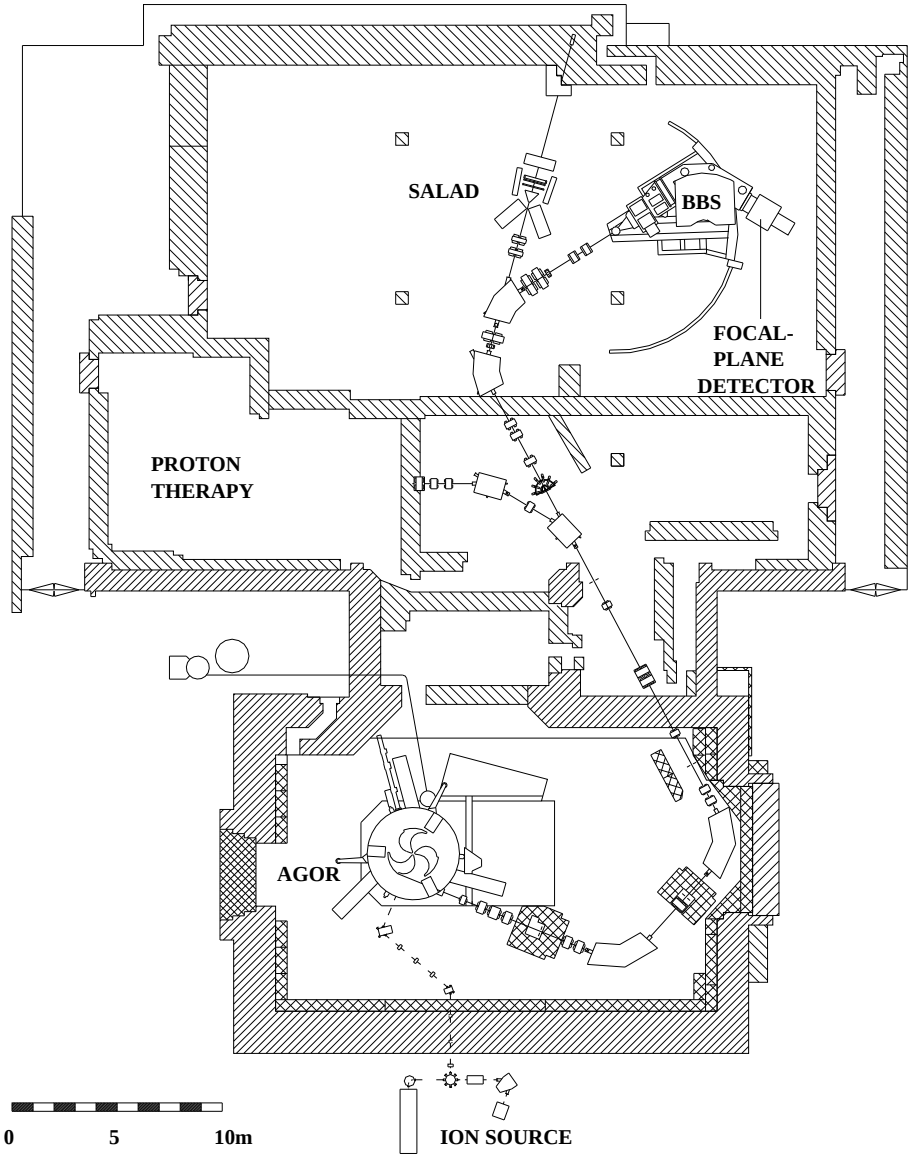

Figure 5.3: Floor plan of KVI experimental area.

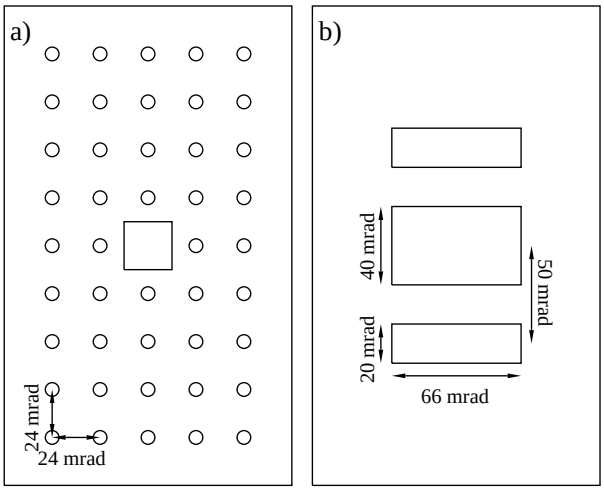

Figure 5.4: a) Sieve slit used for ray-trace calculations and b) angle-defining aperture used for the Pb(^{3}He,t)Bi experiment at KVI (see paragraph 5.2.3).

where α can be x, y, θ, ϕ or δ. The parameters x and θ are distance and angle in the horizontal direction and y and ϕ similarly in the vertical direction. The relative momentum deviation δ is given by $(p - p_0)/p_0$ where p is the incoming momentum and p_0 the central momentum. The order of the expansion is given by $\chi + \mu + \lambda + \nu + \eta$. Matrix elements of the type $(\alpha\,|\,\alpha)$ give the (angular) magnifications and $(x\,|\,\delta)$ is called the dispersion D, usually given in cm/%. Symmetries in the ion-optical system give some constraint conditions on the matrix elements. As a results, some terms become zero because of symmetry considerations with respect to the median plane.

Magnitudes of transfer coefficients are altered by magnetic fields of a multipole of order equal to that of the coefficient. One can introduce various multipole elements into a magnetic system. In this way it is possible to correct for aberrations caused by, for example, inhomogeneities of the magnetic dipole field and for kinematic correlations, like momentum spread of the beam at the object and angular correlation with δ at the object. Curved entrance and exit boundaries of (dipole) magnets also give rise to fixed multipole components, which in turn can be used to improve the optical properties of a spectrometer.

In order to get accurate information about the optical properties of a spectrometer, one has to perform calibration measurements, in which one determines experimentally the matrix T. After such a measurement one is able to trace all events from the detection system back to the target. The calibration measurements are performed using a sieve slit, that is placed in front of the entrance of the imaging system (see figure 5.4(a) for the sieve slit used at KVI). The image of the holes in the sieve slit, of which the positions and angles are exactly known, combined with the knowledge of the exact momentum for certain states, allows the elements of the transfer matrix to be calculated. It is assumed

that the beam spot on the target is very small, so that x_1 and y_1 are zero. This is a reasonable assumption, as long as improvement of energy resolution by means of dispersion matching is not applied (which was the case for both experiments described in this work). In figure 5.5 results before and after software corrections are shown. The data are taken from the experiment at KVI, where the calibration measurements have been performed using the ^{12}C(^{3}He,t) reaction. In figure 5.5(a), the horizontal angle measured at the detector is plotted against the horizontal position measured at the detector. Lines that correspond to groups of holes with the same horizontal position in the sieve slit (see figure 5.4(a)) can be distinguished. A similar plot is shown in figure 5.5(b), but now for the vertical position at the detector versus the horizontal position at the detector. The vertical position is the main ingredient for the polynomial that is used to calculate the vertical angle at the target, since the sensitivity for determining the vertical angle at the target via the vertical angle at the detector is very poor. One can see that the lines (each of which corresponds to groups of holes with the same vertical position in the sieve slit) converge at around -20 cm. At this point, the cross over of the so-called *bow-tie*, there is no sensitivity for determination of the vertical scattering angle via the vertical position measured in the focal plane. Also, at around 20 cm, one can see a diagonal band where no events have been registered. This is due to a failing strip in one of the position-sensitive detectors (see section 5.2.3). In figure 5.5(c) the image of the sieve slit in the right-hand side of the focal plane has been traced back to the target. In principle, it should be an exact copy of the slit in figure 5.4(a). One can see that parts of the phase-space are cut (some holes are missing) and that there are still some slight deviations. This is due to the fact that the polynomial (equation 5.2) has been truncated and the lack of sensitivity in the vertical angle at the focal plane, so that certain elements of the transfer matrix could not be determined. In figure 5.5(d) the $|Q|$-value spectrum is displayed after ray-tracing and calibration. The first two peaks correspond to the ground state and first-excited state (0.96 MeV) of ^{12}N. The peaks at high $|Q|$, around 60 MeV, correspond to deuterons from the ^{12}C(^{3}He,d)^{13}N reaction. In all four spectra, one can see some remaining background. A detailed description of the ray-trace analysis of the data taken at KVI can be found in reference [139]. A similar procedure was followed for the data taken at IUCF. Some specific details about the two spectrometers are given in the next two section.

5.2.2 The K600 spectrometer at IUCF

In figure 5.6 the K600 spectrometer, which came into operation in 1986, is displayed [140]. Since then several improvements have been made. Most significant for this work was the preparation of the transmission mode in 1990 and 1991 [141, 142] which allowed experiments at scattering angles below 3°. In table 5.1 the design parameters of the K600 spectrograph are given for the normal dispersion mode. The K600 consists of a hexapole, a quadrupole and two dipole magnets. The quadrupole magnet modifies matrix elements of first order and the hexapole magnet is used to change second-order components. In addition two dipole pole-face current windings (the H and K coils) are installed for 'hardware' aberration corrections. The operation of these current windings is explained in figure 5.7 (in figure 5.7(a) for the K-coil and in figure 5.7(b)

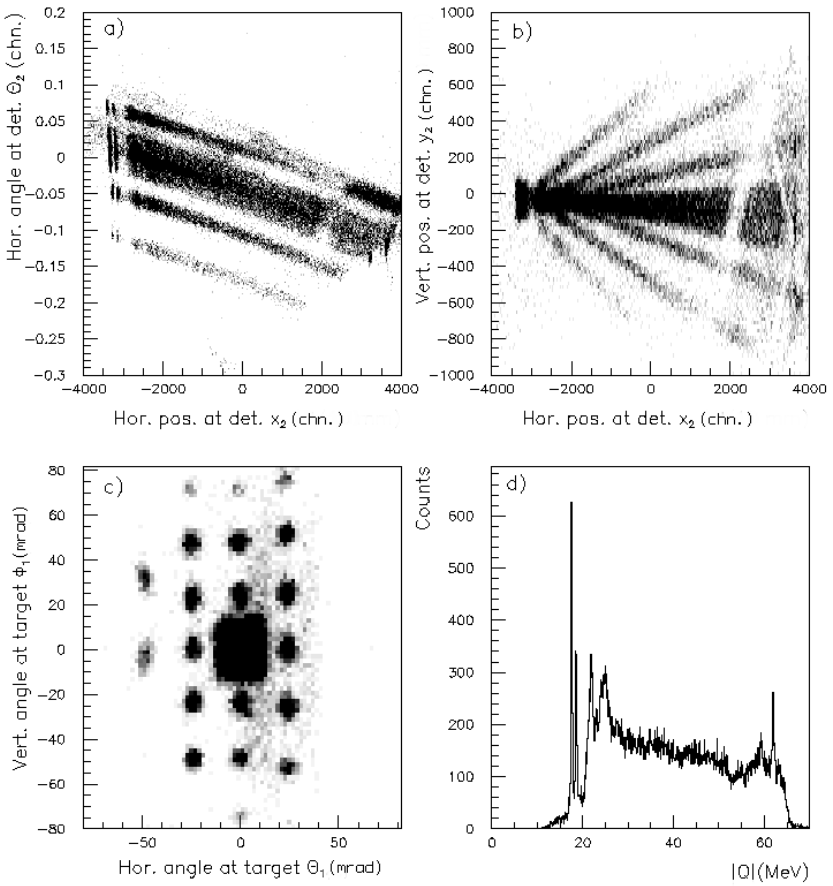

Figure 5.5: Panels a and b: Data from ^{12}C(^{3}He,t) at E(^{3}He)=199 MeV, used for ray-trace calculations. One channel on the x-axes corresponds to 0.1 mm. Panels c and d: results after software corrections. Figures are explained in the text.

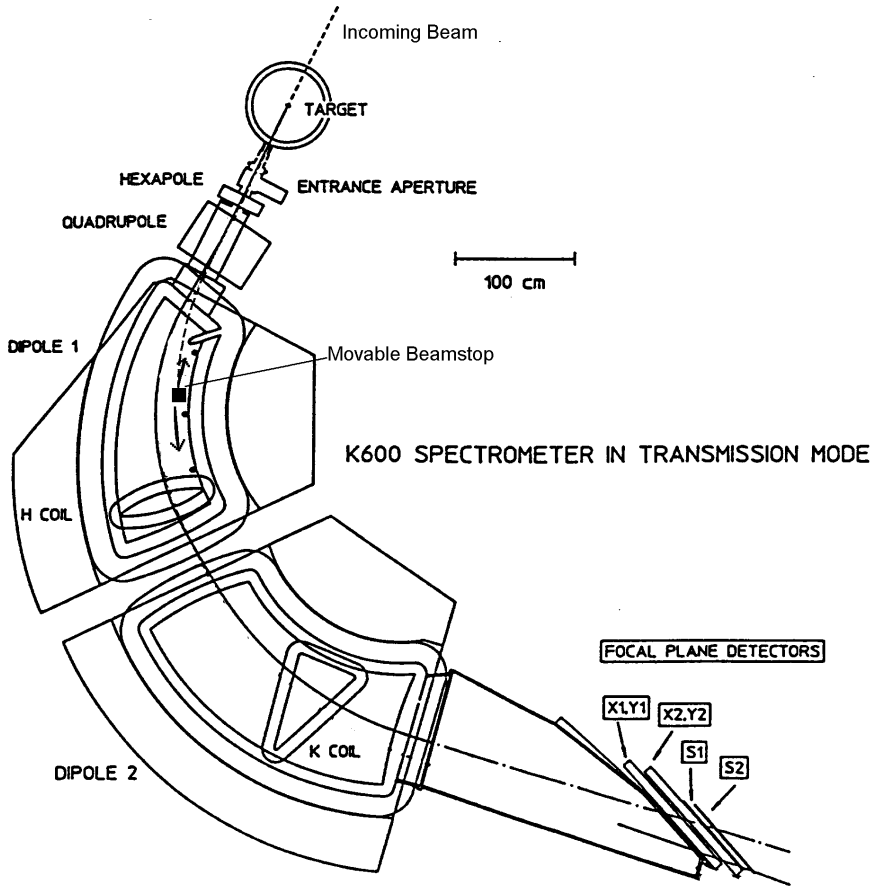

Figure 5.6: A schematic view of the K600 spectrometer

Table 5.1: Design parameters for the K600 spectrometer at IUCF in transmission mode.

Maximum Solid Angle	6.1 msr
Maximum horizontal opening angle	88 mrad
Maximum vertical opening angle	88 mrad
Momentum bite $\frac{\Delta p_{max}}{p_0}$	9.7 %
Dispersion (D)	8.1 cm/%
Horizontal Magnification (M_x)	-0.53
Vertical Magnification (M_y)	-5.7
Bending Limit (K)	600 MeV
Optimum resolution $\frac{\Delta E}{E}$	$1.4*10^{-4}$
Radius of curvature (both dipoles)	210 cm
Ratio of magnetic fields of dipoles	1
Distance target-entrance aperture	78 cm

for the H-coil). The pictures on the left-hand side show the current flow in the coils. The coordinate 'z' is the beam direction and 'x' is the horizontal direction. The centre graphs show the resulting total magnetic fields. On the right hand side it is shown how these resulting fields can be divided up into a dipole and a quadrupole contribution in the case of the K-coil and a dipole and a hexapole contribution in the case of the H-coil. The K-coil is used to correct for the kinematic image broadening due to a correlation between δ and θ_1 at the object point. The kinematic factor K is defined as:

$$K \equiv \frac{1}{p}\frac{dp}{d\theta}, \tag{5.3}$$

and is not equal to zero ($K < 0$ for positive θ, in direction of increasing reaction angle) unless θ=0. This causes the image plane to move downstream (upstream) for $K > 0$ ($K < 0$). For $K = 0$, $(x \mid \theta) = 0$ and for $(K \neq 0)$ $(x \mid \theta) + (x \mid \delta)K = 0$ holds [143]. Besides the moving of the image plane, the image line in the xz plane rotates with respect to the central ray. This results in a modification of the horizontal magnification and the dispersion D. The moving of the image plane can be solved by introducing a quadrupole field (in case of the K600 by the K-coil) because it changes the first-order components that are involved. To correct for the tilting of the image line in the xz plane higher-order multipole fields are needed. More details on the ion-optical properties of the K600 spectrometer can be found in the notes by Schwandt [144, 145].

The focal-plane detection system [146] of the K600 consists of a wire-chamber array and a scintillator stack (see figure 5.8). The wire-chamber array consists of two *vertical drift chambers* (VDC's) and four *horizontal drift chambers* (HDC's). The VDC's measure position and angle in the horizontal direction and similarly in the vertical direction for the HDC's. The first VDC is placed more or less in the horizontal focal plane of the spectrometer.

Each VDC has 160 gold-plated tungsten sense wires of 20 μm diameter that act as anodes. Between two sense wires there are two (50 μm, Berrilium-Copper) guard wires,

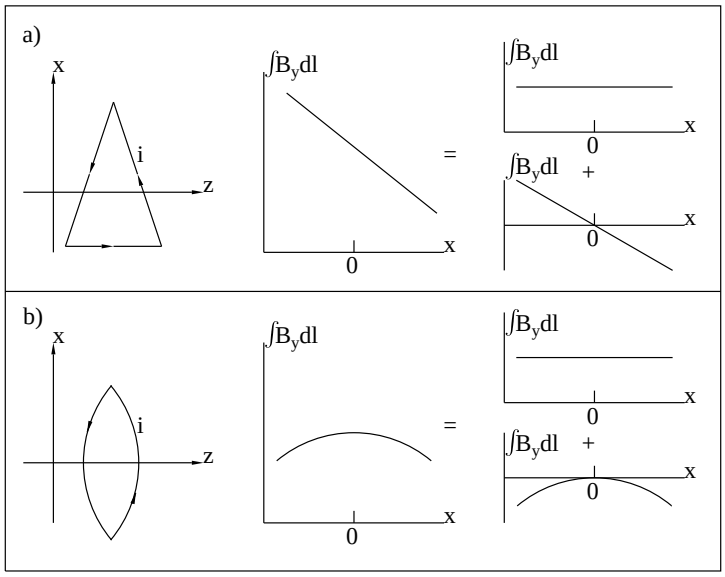

Figure 5.7: Magnetic fields caused by dipole pole-face current windings: a) the K-coil and b) the H-coil. The arrows in the figures on the left-hand side indicate the direction of the current (i).

which are kept at ground potential, and that shape the electric field in the chamber. The wire distance is 2 mm and hence the distance between the sense wires is 6 mm. The wires are mounted between two graphite-coated cathode foils which are biased at -4.5 kV. An ionising particle that passes through the chamber will create electrons (from the gas molecules in the VDC) which will drift along the electric field lines to the sense wires. The cathode voltage should be high enough to make the electron drift-velocity saturate. The drift time of the electrons is then proportional to the distance that the electrons traveled from the point where they were created. Measuring the drift time for neighbouring sense wires gives the path of the ionising particle and hence via a simple calculation the position in the focal plane up to an accuracy of 150 μm. Although using one wire frame only is enough to calculate the angle of incidence, a more accurate value can be found by combining the positions found in two wire frames. The gas that is used is a mixture of argon (50%) and ethane (50%) at atmospheric pressure.

The HDC's are based on the same principle. There are now eight anode sense wires that are strung horizontally. In between these wires only one cathode guard wire is put which is kept at the same potential as the cathode plains. Every HDC consists of two chambers in which the position of guard and sense wires are reversed. This is necessary to resolve the ambiguity regarding to which side of the wire the particle passed, since the particles will travel almost parallel to the dipole faces.

The scintillator stack consists of a thin scintillator (1/8") and a thick one (1/2"). It serves several purposes. It provides the event trigger, the start time for the drift-time measurement of the VDC's and HDC's and also the stop signal for the time-of-flight measurement of the particles passing through the spectrometer with respect to the RF-frequency of the cyclotron. Furthermore, it is used to identify the particles that pass through the detector system by ΔE-E measurement and, if necessary, to exclude instrumental background. The scintillator paddles are read out by phototubes at both ends of each scintillator. During the experiment a 1/16" steel plate and a 1/16" aluminium plate were put between the two scintillators to stop singly-charged ^{3}He particles (beam particles that have picked up an electron in the target) from reaching the second scintillator. Since for a 'good' event both paddles need to fire, this procedure reduced the count rate strongly and thereby the dead time. The tritons were not stopped by the extra plates.

For this (^{3}He,t) experiment, the beam was stopped inside the first dipole magnet. The beam stop is movable and can be put in advance at exactly the right position to stop the beam. It also serves as an integrator of the collected charge, which is needed for the determination of the absolute values of cross sections.

Because the momentum bite of the K600 is not large enough to cover the excitation-energy range of interest for this experiment, two magnetic-field settings, overlapping in excitation energy, were used. To define the solid angle, a circular aperture was used with an angular diameter of 70 mrad. The spectrometer was put at a scattering angle of -10 mrad (-0.57°), i.e. the beam entered the spectrometer along its shorter curvature.

Ray-tracing measurements were performed at a scattering angle of 20° using elastically scattered $^3He^{++}$ particles from a ^{197}Au target. Since the actual experiment was done by detecting tritons near 0°, the dipole field had to be increased by a factor of two. In order for the calculated ray-trace coefficients to remain valid, the fields of the quadrupole and hexapole magnets, as well as the currents in the correction coils were scaled accordingly. A correction to the scaling had to be performed, however, since the magnetic field that is needed to bend the high-energy tritons is so high that the dipole magnet ran into saturation. In the analysis it turned out that this scaling and correction was insufficient to correctly reproduce the focusing conditions in the vertical direction of the lower field setting, possibly due to higher-order aberration effects. Therefore, the vertical position, and thus the vertical angle, could not be used in the analysis. The FWHM found for the horizontal scattering angle of particles passing through one of the holes in the sieve slit was found to be 5.1 mrad. Taking the width of the holes in the sieve slit into account, this gives a resolution in the horizontal scattering angle of 2.6 mrad. The energy resolution was 300 keV FWHM ($\Delta p/p = 7.5 * 10^{-4}$).

5.2.3 The Big-Bite Spectrometer

In figure 5.9 a drawing of the BBS [147] (K=430 MeV) is shown. In contrast to the K600 spectrometer at IUCF it has one dipole magnet. Two quadrupole magnets behind the scattering chamber are used to change focusing conditions. There are no correction

Table 5.2: Design parameters for the Big-Bite Spectrometer at KVI in mode B.

Maximum Solid Angle	9.2 msr
Maximum horizontal opening angle	66 mrad
Maximum vertical opening angle	140 mrad
Momentum bite $\frac{\Delta p_{max}}{p_0}$	19%
Dispersion (D)	2.54 cm/%
Horizontal Magnification (M_x)	-0.45
Vertical Magnification (M_y)	-10.1
Bending limit (K)	430 MeV
Optimum resolution $\frac{\Delta E}{E}$	$4*10^{-4}$
Radius of curvature	220 cm
Maximum magnetic field of dipole	1.4 T
Distance target-entrance aperture	81.7 cm
Distance target-entrance Q1	1.14 m

coils or higher-order magnets present. Correction for aberrations is done purely by software.

There are three modes which differ in the position of the quadrupole doublet with respect to the scattering chamber and the entrance of the dipole. The closer the doublet is to the scattering chamber, the larger the solid angle and the lower the momentum acceptance. In the present experiment, the intermediate mode B was used. The design parameters for the BBS in this mode are given in table 5.2 [147].

Several focal-plane detection systems exist for use with the BBS. For this work the light-ion detection system, designed and constructed at the *Institut de Physique Nucléaire* (IPN) in Orsay, France [148] was used. The position-sensitive detectors are of the so-called *cathode-strip chambers* (CSC) type and are placed in a vacuum tank that is mounted behind the BBS (see figure 5.9). A segmented scintillator stack is mounted behind this tank and serves the same purposes as the stack of the K600 spectrometer. The first scintillator layer has four segments of 2 mm thickness each, which are separately read out. The second scintillator layer has two segments which are 5 mm thick each.

In figure 5.10 a schematic view of one CSC is given. When particles pass by the anode wires which are put at high voltage, an electron avalanche will be created. This avalanche induces an image charge on the cathode strips. The charge signals from the strips are amplified by preamplifiers (2 strips per preamplifier) and subsequently read out. The centroid of the charge distribution is calculated on-line by a digital signal processor (DSP). There is a U and a V plane whose strips are at right angles with each other and at 45° with the horizontal plane. The cathodes consist of 128 gold strips of 6 mm wide and a pitch of 6.4 mm. The anodes consist of gold-plated tungsten wires with a diameter of 20 μm and with a pitch of 3.2 mm. The central cathode decouples the U and V parts of the chamber and the electric field in each part are shaped by the anode and two cathodes. The distance between an anode and the corresponding cathode is 6 mm. The distance between each of the anodes and the central cathode is

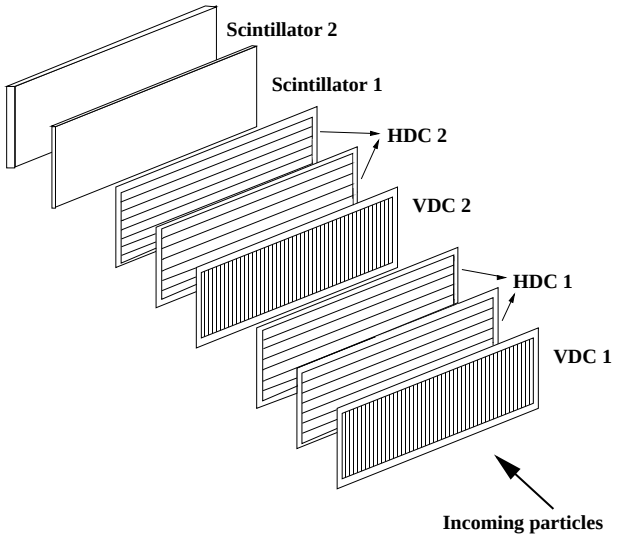

Figure 5.8: A schematic description of the K600 focal-plane detection system.

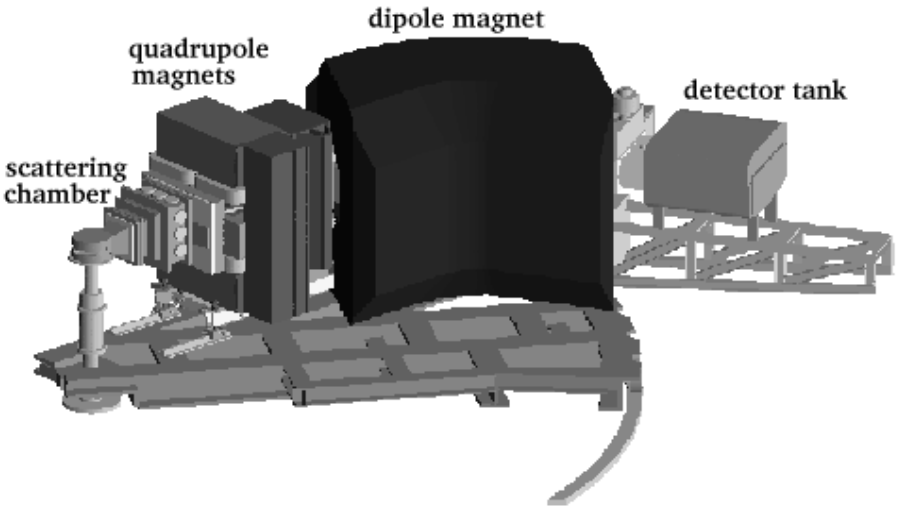

Figure 5.9: The Big-Bite Spectrometer.

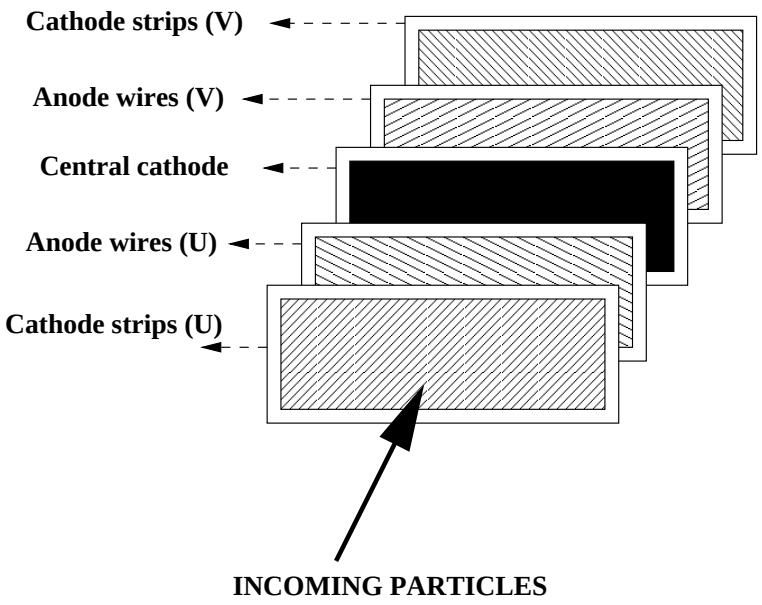

Figure 5.10: A schematic view of a cathode-strip chamber.

8 mm. The total surface of the detection area is 974×250 mm.

From the U and V coordinates so found, the horizontal and vertical positions in the detectors can be calculated. Combining the results of the two CSC's which are present in the vacuum tank, one can also find the horizontal and vertical angles.

The detector gas of the CSC's is an argon-ethane mixture (80%/20%) and for light ions it is kept at a pressure of 1 bar. Since also experiments are performed where heavier particles are to be detected, the CSC's are put into a vacuum tank. At the exit of the tank a thin pressure foil is mounted in order to enable the particles to reach the scintillators.

Because of the large momentum-bite of the BBS, a large enough excitation-energy range can be covered using one magnetic field setting. To avoid problems with the tracing of parameters in the vertical direction as encountered in the experiment performed at IUCF, ray-trace measurements were performed at 0° using the tritons themselves, instead of the procedure followed at IUCF. A special sieve-slit, with a large hole in the centre (see figure 5.4(a)) to allow the beam to pass through, was made for this purpose.

The cross over of the bow tie was put on the left-hand side of the focal plane. Therefore, good vertical-position resolution (and thus good vertical-scattering-angle resolution) was obtained for $|Q|>$ 27 MeV. Moving the cross over of the bow tie even further to the left would mean that the covered vertical angular acceptance would be cut due to the limited height of the detector. The range was limited to $|Q|$=48 MeV by a broken strip (figure 5.5(b)).

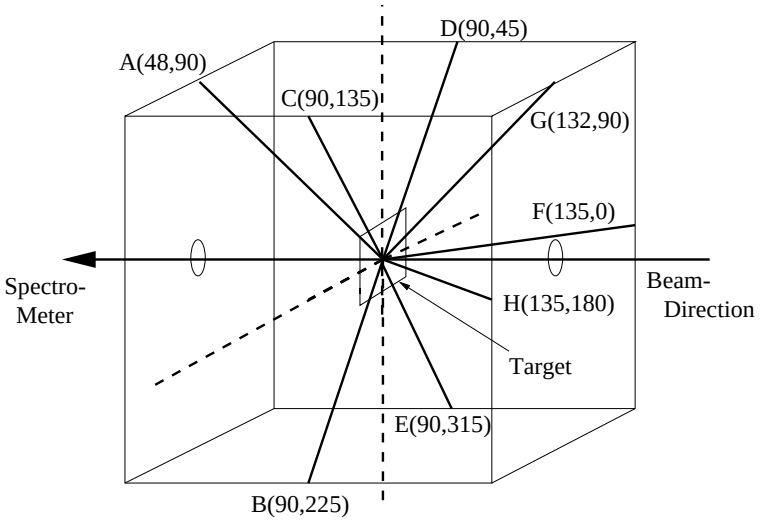

Figure 5.11: Schematic view of the position of the neutron detectors. The detectors are positioned along the thick black lines. (x,y) gives θ and ϕ for every detector.

For unambiguous interpretation of the data, the angle calibrations need to be very reliable and it was decided to use a special angle-defining slit (see figure 5.4(b)). The openings in this special aperture were chosen to coincide with extrema in the angular distribution of the IVGMR and SIVM (see figure 7.4). The spectrometer was put at -1°.

Taking the width of the holes in the sieve slit into account, the angular resolution in the horizontal direction was found to be 3.7 mrad (FWHM) and in the vertical direction (in the $|Q|$-value range between 27 and 48 MeV) 4.6 mrad (FWHM). The energy resolution was 250 keV (Δp/p=7.5*10^{-4}) if the difference in energy loss of the ^{3}He particles and tritons is taken into account. Without this correction the resolution was 360 keV (Δp/p=1.0*10^{-3}).

5.3 Neutron detection

5.3.1 Setup and pulse-shape discrimination

For the experiment performed at IUCF, coincidences were required between tritons in the focal plane of the spectrometer and neutrons at backward angles. To this end, eight liquid scintillators were placed around the target. A schematic view of the setup is displayed in figure 5.11. Two types of liquid scintillators were used: four NE213 and four NE230 detectors. This was done to compare the low-energy neutron-detection performance of the two scintillators. These were chosen because of their reportedly good neutron-γ discrimination capability. The NE213 detectors are made of aromatic Hydrocarbon (H:C=1.212). The NE230 scintillator consists of deuterated benzene

(D:H=114.1, D:C=0.99).

The scintillating liquids are contained in cylindrical metal tubes whose axes are positioned along the directions shown in figure 5.11. The scintillating material in each tube has dimensions 5 cmø×5 cm and is coupled optically to a photomultiplier. Photons are created from transitions made by valence electrons of the molecules in the liquid. The weak current of photoelectrons created at the photocathode is amplified by an electron-multiplier cascade. A base delivers the high voltage for the potential ladder.

The distance between the detector faces and the target was chosen small (78.5 mm) in order to cover a large solid angle. This makes energy determination for the neutrons and discrimination between neutrons and γ-rays by means of time-of-flight measurement impossible, except for the lowest-energy neutrons. However, the interest is not so much in the energy of the neutrons as in their presence. The neutron-γ discrimination is done using a combination of pulse-shape discrimination and time-of-flight measurement (the latter for the lowest-energy neutrons only). The procedure is shown in figure 5.12. In figure 5.12(a) the difference in pulse shape between neutrons and γ-rays is shown (for NE213 scintillating material, [149]). The difference arises from the fact that the neutron is detected through the recoil proton from the (n,p) scattering process in the scintillating material as well as smaller contributions arising from (in)elastic scattering from carbon, whereas the γ-ray interacts through the photo-electric, Compton and pair-production processes.

The pulse structure can thus be examined by comparing the total integrated pulse (E) due to a particle passing through the detector and the integration over the tail (E_{tail}) of the pulse. This is shown in figure 5.12(b) where E_{tail}/E has been plotted against E. Clearly, starting from channel 30, neutrons and γ-rays can be distinguished. For lower E this is not possible.

In figure 5.12(c) the time structure of the coincidences with respect to the RF of the cyclotron is shown for all coincidences between one detector and tritons in the focal plane. Clearly, the prompt peak and three random peaks can be distinguished. The RF frequency was 33.5 MHz, but in order to be able to separate prompt and random coincidences, only one out of every three bunches of particles from the source was injected into the cyclotron. Therefore, every 90 ns a burst of beam particles arrived at the target.

In figure 5.12(d) the same, slightly expanded, picture is shown, but now for coincidences belonging to events with E<30 chn. in figure 5.12(b). Although there is still some overlap in time between neutrons and γ-rays, a rather good cut can be made. Also, the first random peak is shown, where the same structure can be seen. In the analysis of the data we make the first discrimination using spectra like figure 5.12(b) per detector and use the time information to discriminate particles with low E.

5.3.2 Neutron detection efficiency

The neutron-detection efficiency is dependent on the energy of the neutrons. As discussed above, no information is available about the energy of the neutrons experimentally. In the analysis, however, we must fold the multiplicity calculations with the

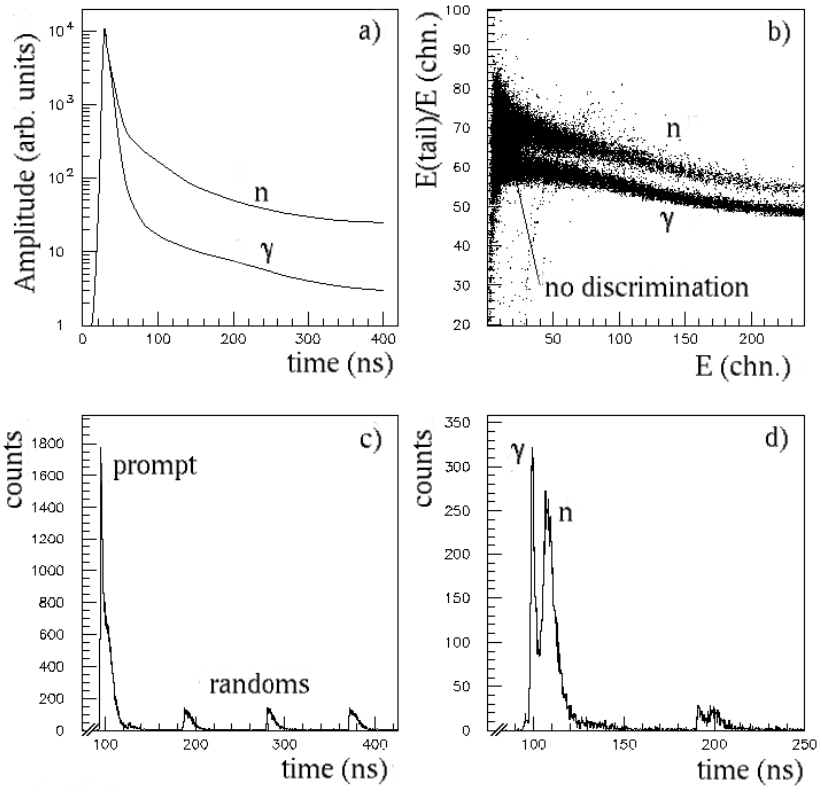

Figure 5.12: Procedure for neutron-γ discrimination. (a) the difference in pulse shape between γ-rays and neutrons for the NE213 scintillator [149]. (b) Integrated tail of pulse (E_{tail}) divided by integrated total pulse (E) versus integrated total pulse (E). (c) Time structure of coincidences showing a large prompt peak and several smaller random peaks. (d) Same as (c) but for particles in the area in (b) where pulse-shape discrimination is not possible. Discrimination using time-of-flight is now possible.

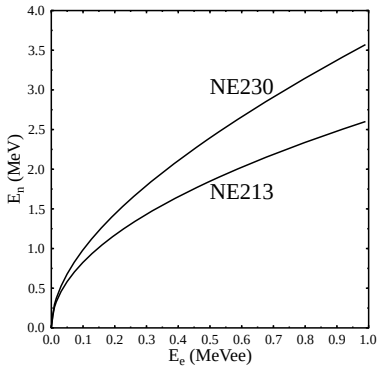

Figure 5.13: Relation between light output for electrons and neutrons for NE213 and NE230 [152]

efficiency in order to be able to interpret the data. The efficiency is strongly dependent on the threshold of the detectors. Since neutrons that are emitted statistically have low energies ($E_n < 6$ MeV) with a maximum in the evaporation spectrum at $E_n \approx 600$ keV, the threshold was put as low as possible. In order to do the efficiency calculations the threshold had to be determined and this was done using the 59.5 keV photopeak from a ^{241}Am source and the Compton edges of the 0.511 MeV and 1.275 MeV γ-rays from a ^{22}Na source (at 0.341 MeV and 1.061 MeV). The location of the position of the Compton edge in the measured spectra is a matter of discussion [150] and could give rise to systematic errors in the determination of the threshold. In the present work we followed Dietze and Klein [150] who found that the position of the Compton edge is at the channel whose height is 2/3 of the maximum in the Compton spectrum.

When using liquid scintillators, one actually measures light output (L). The light output is linear with incoming energy for electrons and is given by:

$$L = E_e - E_0 \tag{5.4}$$

where E_0 is a threshold parameter and has been taken 15 keV following Olsson et al. [151]. Therefore, the light output is usually expressed in electron-equivalent units (e.g. keVee). This can then be translated into neutron energies via a procedure which depends on the scintillating material used. For NE230 and NE213 this is shown in figure 5.13 (based on Smith et al. [152]).

For the NE230 detectors, efficiency measurements were available for almost the same setup as used for this work [153] and have been used. For the NE213 detectors, Monte-Carlo calculations were performed using the code NEFF7 [154]. In this code the light-output functions and the cross sections for the various processes that contribute serve as input, as well as the detector geometry. This code has been shown to work very well for NE213 detectors [151]. In figure 5.14 efficiency curves are shown for

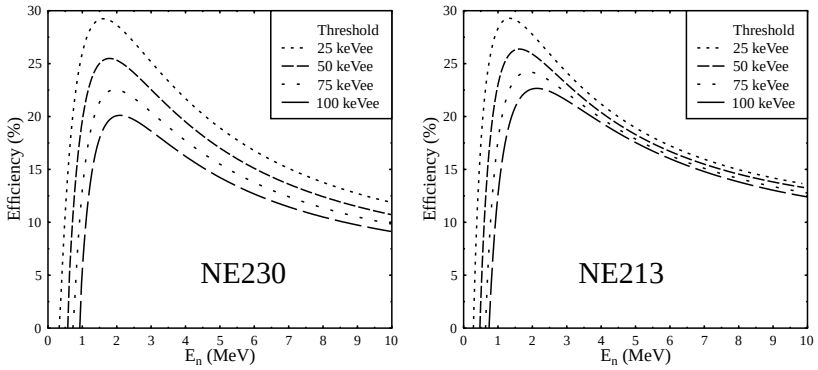

Figure 5.14: Efficiency curves for different thresholds for a NE230 detector (left) and a NE213 detector (right)

NE213 and NE230, for thresholds between 25 keVee and 100 keVee. The two look similar, although at higher neutron energies the efficiencies for the different thresholds for NE213 converge more and are slightly higher than for NE230. The thresholds were determined per detector using the above-described method and were found to vary from 30 keVee to 80 keVee. Also, two sets of calculations had to be performed since the detectors were switched off between the measurements with low and high magnetic dipole field settings, causing the thresholds to change. For one detector the gain fluctuated frequently during the experiment and thus was not used in the analysis. For another detector the threshold had shifted up so high during the experiment that for part of the runs no useful data was obtained.

5.4 Proton detection

For the experiment at KVI coincidences were required between tritons in the focal plane of the BBS and protons at backward angles. For detecting the protons a new detector system, the so-called *Silicon Ball* was designed and constructed. In figure 5.15 a picture of the Silicon Ball is shown. The Silicon Ball consists of up to 20 Lithium-drifted Silicon (Si(Li)) detectors each of which has a thickness of 5 mm and an effective area of 450 mm^2. They were obtained from *Lawrence Berkeley National Laboratory*. The operating voltage is 600 V. Four detectors can be put on one of the arms of the ball. On each arm the detectors can be placed between -20° and +40° out-of-plane angle. The arms can be put at any angle around the target. The distance between the centre of the ball and the front of each detector is 100 mm. For 20 detectors, the covered solid angle is 0.9 sr. The frame of the ball is cooled by alcohol that flows through the upper and lower rings. The detectors are cooled by conduction in order to reduce the noise in the detectors. The temperature can be measured using temperature-dependent resistances that are screwed into the frame. The material of the frame and detector

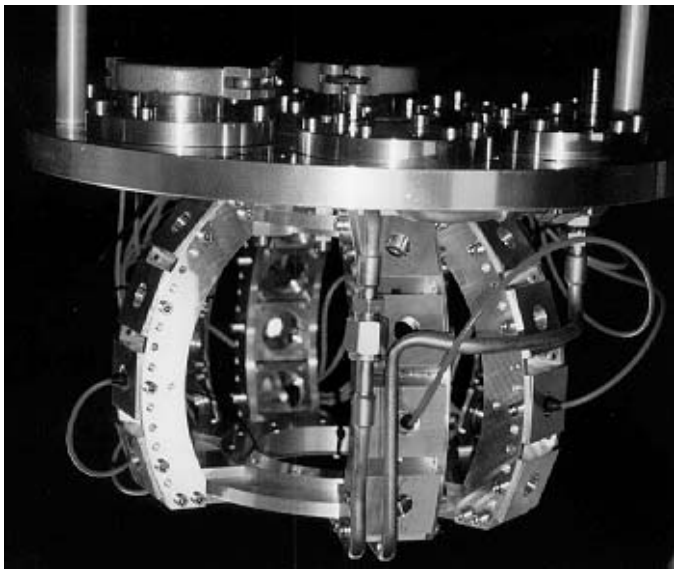

Figure 5.15: Picture of the *Silicon ball*, connected to the lid of the scattering chamber. For details, see text.

holders is MIC-6, which was chosen because of its good heat conductivity and because it is easy to handle. The whole construction is connected to the lid of the scattering chamber. The lid, which contains the necessary connectors as well as the alcohol inlets, was especially designed and constructed for use with the silicon ball. In figure 5.15 one can see the tubes for the flow of liquid alcohol from the upper to the lower ring. Also, some of the cables, connecting the detectors (which have rear-mount, 93Ω connectors) to the feedthroughs in the lid can be seen.

In figure 5.16, a drawing of the the Silicon ball is shown, in the configuration as it was used during the (^{3}He,tp) experiment described in chapter 7 of this thesis. The detectors are positioned at backward angles. One position, in the central arm, is left open to allow for the beam to pass through.

The cooling properties of the ball and the effect of temperature on energy resolution of the detectors were studied thoroughly [155] using a mixed α-source (^{239}Pu, ^{241}Am, ^{244}Cm). A resolution of typically 30 keV FWHM for E_α=5 MeV was found at -30° (figure 5.17) as compared to a resolution of 100 keV at room temperature.

Signal read-out is done through *MICROTEL* preamplifiers that are placed in a copper box to reduce the noise pick-up. It was decided to use the electronics of the neutron detector EDEN for the experiment performed at KVI since the data-acquisition for coincidence experiments using the Orsay focal-plane detector and EDEN was already existent. To this end the silicon detectors had to be read out using charge integrators and this was done as show in figure 5.18. The signal from the detectors is split after the preamplifier into a timing branch and an energy branch. The timing branch serves a double purpose; it gives a signal that is used for the time-of-flight measurement of

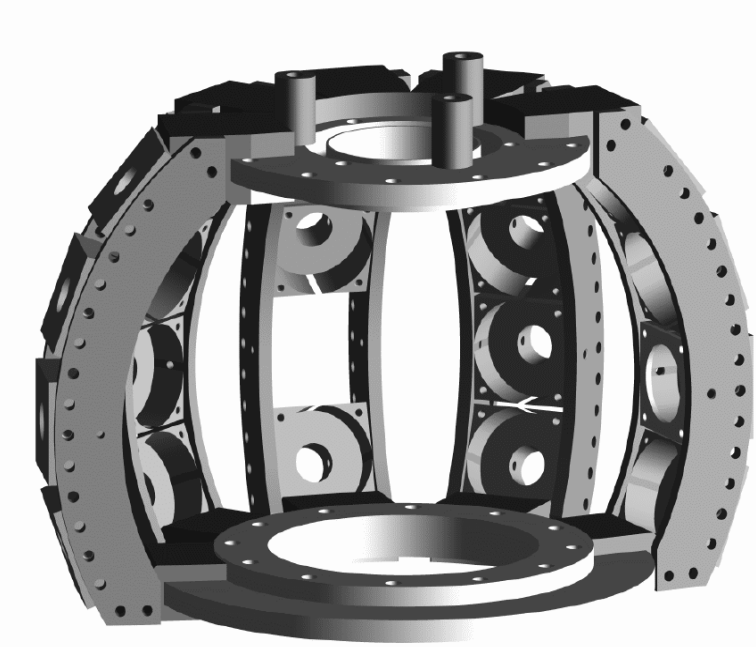

Figure 5.16: Drawing of the Silicon Ball charged-particle detector in the configuration as used in the experiment. The silicon detectors themselves are not shown. One position is left open for the beam to pass through.

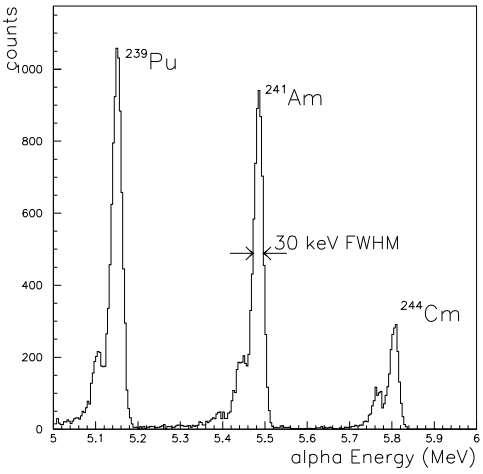

Figure 5.17: Resolution measurement of one silicon detector at -30° using a source with various α-particle emitters.

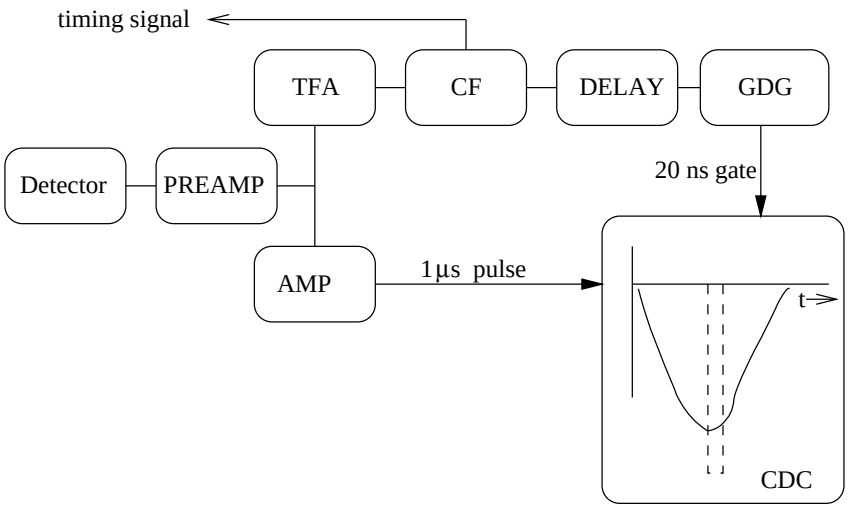

Figure 5.18: Electronics setup for reading out one Silicon detector using a charge-to-digital converter from. PREAMP: preamplifier, AMP: main amplifier, TFA: timing-filter amplifier, CF: constant-fraction discriminator, GDG: gate and delay generator and CDC: charge-to-digital converter

the protons with respect to the RF of the cyclotron and it provides a small gate that defines the integration period for the charge-to-digital converter (CDC). By an adjustable delay this gate is positioned exactly over the top of the signal from the main amplifier in the energy branch. The gate was set to 20 ns because of the limited range of the CDC. The resolution in the energy signal was found to be similar, if not better, to results where the energy is read out through an analog-to-digital converter. This indicates that almost no time jitter was present.

For the experiment, the main interest was in decay by proton emission at very high excitation energies ($E_x \sim 30 - 50$ MeV). Therefore, a fraction of the emitted protons will have such a high energy that they will punch through the detector and thus deposit less energy in it. This effect has been simulated using the Monte-Carlo code TRIM90 [156]. The result is shown in figure 5.19(a). Up till an energy of 30 MeV the protons are stopped in the detector. Above 30 MeV they punch through and deposit energy with a certain spread, as indicated by the dotted lines.

In figure 5.19(b) the time of flight of the protons with respect to the time of flight of the tritons is shown. Due to the varying time of flight of the tritons and the protons and the fact that a burst of particles arrived at the target every 27 ns (the cyclotron RF frequency was 37 MHz), the random-peak structure is completely washed out (the width of the prompt peak is 40 ns). In principle this can partly be corrected for, but this was not necessary in the present work.

It can also be seen that the number of randoms right from the prompt peak is slightly higher that the number of randoms on the left-hand side. It was observed, by comparing proton-energy spectra in time ranges left and right of the prompt peak that

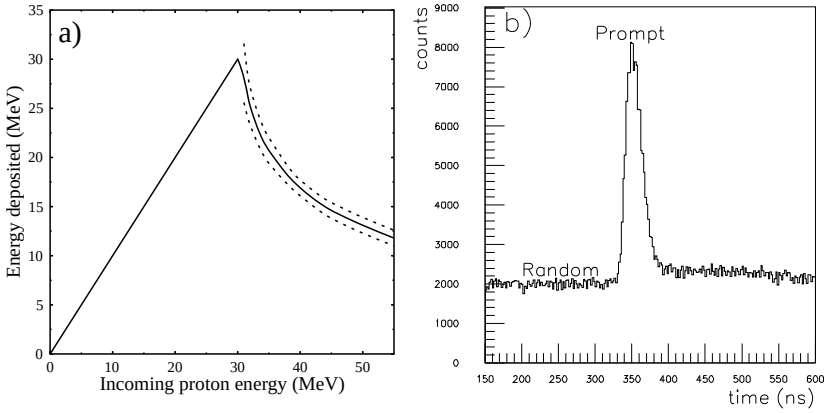

Figure 5.19: a) Simulation of punch-through effect for the silicon detectors. At 30 MeV the protons are not completely stopped and deposit only a fraction of their total energy. The dotted lines indicate the FWHM of the proton-energy distribution. b) Time of flight of protons with respect to time of flight of the tritons. See also text.

the extra counts on the right-hand side all correspond to additional low energy protons. This could be caused by scattering from the entrance slit of the BBS or the beam pipe. Such an additional contribution was not present in the time range of the prompt peak and left of the prompt peak and, therefore, a time-range left of the prompt peak has been chosen to create random spectra.

6. The ^{124}Sn(^{3}He,tn) experiment at IUCF

In this chapter, the experiment performed at IUCF will be discussed. First, predictions given by the various models concerning position, magnitude and width of the strength distributions will be discussed. After that the singles and coincidence spectra are described, together with the procedures for taking the detection efficiency and neutron multiplicity into account.

The *XSYS* data-acquisition system and graphical analysis package was used for the online and offline analysis. This system, originally based on the MBD-11 CAMAC-branch controller, was developed at *Triangle Universities Nuclear Laboratory* (TUNL) and has been extended and upgraded for application at IUCF [157]. For use with the K600 spectrometer, the MBD-11 was replaced by a VME-crate. The routines were written by Stephenson [158]. The original routines for the processing of the data from the neutron detectors were written by Roberts and Jänecke [159].

6.1 Predictions

In the (^{3}He,t) reaction three components with different isospin ($T-1$, T and $T+1$) of the SIVM and IVGMR are excited. In heavy nuclei, most of the strength goes to the $T-1$ component. Estimating the excitation strengths B (see section 3.4) from the isospin-coupling (Clebsch-Gordan) coefficients gives a ratio for $B^{T+1,T-1} : B^{T,T-1} : B^{T-1,T-1}$ in ^{124}Sb of $1 : 25 : 299$. If the estimates for the reduced transition probabilities are used (equation (3.50) [98]), the $T-1$ component is relatively even more enhanced. The ratio is then $1 : 31.5 : 448$. It is therefore logical to use the excitation energy of the $T-1$ component as centroid of the resonances. Equation (3.53) can then be used to calculate the centroid for the IVGMR. The parameters V_0 and V_1 of equation (3.53) have been determined in various ways with slightly different outcome. This results in different values for the expected excitation energy. In table 6.1, a summary of the different values for V_0 and V_1 is given. Generally speaking, the value of V_1 is strongly quenched with respect to the single-particle symmetry potential ($V_1 \approx 100$ MeV [40]) because of the repulsive residual p-h interactions in the collective states. From the values listed, one finds an excitation energy for the IVGMR of 36 ± 3 MeV, except when using the simple shell-model estimate, which gives a much lower value. This can be understood from the fact that the residual p-h interaction for isovector excitations is repulsive and, as a consequence, the isovector resonances will be located above the unperturbed energy of $2\hbar\omega$. For isoscalar transitions the residual p-h is attractive and isoscalar resonances are, therefore, located below the unperturbed energy.

For the SIVM the excitation energy is not expected to differ very much from that of the IVGMR. Experimental data for the IVGMR in the tin region for the $T_z = -1$

Table 6.1: Summary of predictions for V_0 and V_1 in equation (3.53).

Method	V_0 [MeV]	V_1 [MeV]	Ref.
Simple shell model	82		
Hydrodynamical model (volume)	170		[40]
Displacement of dipole isodoublets		60	[160]
Fit on HF-RPA calculations	155	55[a]	[33]
Analysis of data on dipole excitations		58±5	[161]
Residual ph-interaction (2p-2h) in IVGMR		60±9	[162]

[a]For ^{208}Pb a value of 72 MeV is found.

Table 6.2: Summary of values for the width of the IVGMR in ^{124}Sb.

Method	Γ [MeV]	Ref.
Dissipative term in Euler eq. (eq. 2.7)	5.2	[45]
Width of the IAS, $\beta = 0$ (section 4.4)	6.5	[134]
Width of the IAS, $\beta \neq 0$ (section 4.4)	10.8	[134]
HF-RPA approach	25	[33]
(π^+, π^0) data on ^{120}Sn	16±4[a]	[21]

[a]Cross section is consistent with zero [21]

direction are only available from the (π^+,π^0) reactions on ^{120}Sn [21]. Complications in these data have already been discussed in section 4.2. For the IVGMR excited through the $^{120}Sn(\pi^+,\pi^0)^{120}Sb$ reaction, the authors report an excitation energy of 30±3 MeV and a width of 16±4 MeV, but the cross section itself is consistent with zero. These values should, therefore, be taken with caution.

For the widths of the IVGMR and SIVM the situation is much less clear. In table 6.2, various estimates for the width of the IVGMR in ^{124}Sn are given. It is difficult to draw any conclusion.

Finally, one can estimate the strengths of the IVGMR and SIVM. HF-RPA calculations for the IVGMR in ^{120}Sn were performed by Auerbach and Klein [33]. Although they performed similar calculations for the SIVM, results for ^{120}Sn were not published. In this work, calculations have been performed in a normal-mode framework, using the code NORMOD [63] (see section 3.2.4), which gives an upper limit to the transition strength; the most collective configuration of the excitation is calculated.

In appendix A (tables A.1 to A.3), the wave functions projected on the 1p-1h basis and their amplitudes (equation (3.39)) are given. The occupation numbers for the neutrons in the last major shell are not equal to one and the values that are used are taken from the literature [163]. They are given in table 6.3.

The results for the total transition strength are listed in table 6.4. For completeness, also the calculated strengths for the Gamow-Teller resonance (GTR), isovector dipole resonance (IVGDR), the three components of the spin-dipole Resonance (SDR) and isovector quadrupole resonance (IVGQR) are given. When multiplied by 4π, the

Table 6.3: Occupation numbers for neutron shells in last major shell [163].

Neutron Shell	Occupation number
$1d_{3/2}$	0.69
$2s_{1/2}$	0.80
$0h_{11/2}$	0.63[a]
$1d_{5/2}$	0.94
$0g_{7/2}$	0.80[a]

[a]These values are estimated based upon occupation numbers of lower-mass Sn isotopes [163], such that equation 3.40 is fulfilled.

Table 6.4: Transition strengths calculated for various resonances excited via the ^{124}Sn(^{3}He,t)^{124}Sb reaction, using a normal-mode procedure (column 2). They are compared with the results from HF-RPA calculations by Auerbach and Klein [33] (column 3) and by Kuzmin and Soloviev [164] (column 4).

Resonance	Normal modes	HF-RPA	
		[165, 33, 36][a]	[164]
IAS	1.907		
GTR	6.003		
IVGMR	755.4 fm^4	429 fm^4	
SIVM	2266 fm^4		
IVGDR	193.6 fm^2	126.2 fm^2	
SDR 0^-	82.2 fm^2		67.7 fm^2
SDR 1^-	220 fm^2		181.3 fm^2
SDR 2^-	318 fm^2		276.7 fm^2
IVGQR	9623 fm^4	8006 fm^4	

[a]The values taken from the literature have been re-calculated to match the operator definition of equation (3.37).

normal-mode strength of the IAS nicely reproduces the Fermi sum rule as given in equation (3.52). For the GTR, the normal-mode strength is approximately 75 (when multiplied by 4π). It can be understood that this is slightly higher than 3(N-Z)=72, because the second term, S_+^β, of the Ikeda-Fujii-Fujita sum rule (equation (3.54)) is small, but non-zero. In table 6.4, also the result from RPA calculations by Auerbach and Klein [33] for the IVGMR in ^{120}Sb and for the SDR in ^{124}Sb by Kuzmin and Soloviev [164] are given. For the IVGMR the normal-modes calculation gives a much higher value than the HF-RPA calculations.

The reason for this difference between estimates is similar to the difference between HF-RPA and Tamm-Dancoff (TD) calculations, as discussed by Auerbach and Klein [36]. The HF-RPA calculations take ground-state correlations into account, in contrast to the normal-mode and TD formalisms (Note that for (semi) open-shell nuclei (like ^{124}Sn) part of the groundstate correlations are taken into account by using experimentally deduced occupation numbers). This will affect the predicted strength for the various transitions. For the dipole and quadrupole resonances, this effect makes

up for the difference of approximately 20% between the normal-mode calculations and the HF-RPA calculations [33, 36]. For the IVGMR and SIVM the difference is larger; approximately 40%. Further differences arise from the fact that non-energy-weighted calculations like these, are model dependent.

6.2 Singles data

6.2.1 Full spectrum

Data were taken with the K600 spectrometer at IUCF, which was set at an angle of -10 mrad (i.e. the beam entered the spectrometer along its shorter curvature). A circular aperture with a diameter of 70 mrad was used to define the opening angle. The target was enriched ^{124}Sn (97.2%) of 7.7 mg/cm^2 thickness. The electronics live-time was approximately 99%. The focal-plane detection efficiency was approximately 85%, obtained by comparing accepted events to the number of triggers from the scintillator detectors. Two series of data with different magnetic-field settings were taken in order to cover a large excitation-energy range. Coincidences and singles data were taken simultaneously, the latter were downscaled by a factor of 10.

Measurements to obtain ray-trace parameters were performed for the elastic and inelastic scattering of the $^{3}He^{++}$ beam at a scattering angle of 20°. However, as explained in chapter 5, the calibration in the vertical direction could not be used in the analysis of the data obtained at 0° because in order to bend the tritons stemming from the (^{3}He,t) reaction the magnetic field had to be so high that the dipole magnet was running into saturation, causing a change of the magnetic-field distributions. Therefore, only the horizontal-angle information could be used in the analysis. Energy calibration for the high magnetic-field setting was done using a $^{12}C(^{3}He,t)^{12}N$ spectrum and the $^{124}Sn(^{3}He,t)^{124}Sb$ spectrum itself. In the latter case, peaks due to the $^{3}He^{+}$ particles (which were not stopped by the extra plates between the two scintillators) and the IAS, of which the excitation energy is well known (E_x=12.187 MeV [134]), were used. For the low magnetic-field setting calibration was done by taking into account the change in the dipole field with respect to the high magnetic-field setting. It turned out that the excitation energy spectra at the low and high magnetic-field settings were overlapping nicely if it was assumed that due to the saturation, the dipole field for the latter setting was 0.5% lower than the set value.

There was a non-negligible amount of instrumental background in the singles data, due to scattering from the beam stop. Therefore, several runs with an empty target frame were taken and subtracted from the singles spectra (the current integrator was used for scaling). The beam stop could not be seen by the neutron detectors because they were shielded from the beam stop by the dipole magnet and, therefore, virtually no instrumental background in the true coincidences was found.

In figure 6.1, the singles spectrum is displayed as a function of excitation energy. The instrumental background has already been subtracted. The ground state Q-value of the $^{124}Sn(^{3}He,t)^{124}Sb$ reaction is -0.636 MeV. At Q=0 there is a small remainder of $^{3}He^{+}$ particles due to atomic charge exchange by picking up an electron in the target. They then have the same magnetic rigidity as the tritons. The spectra taken at the

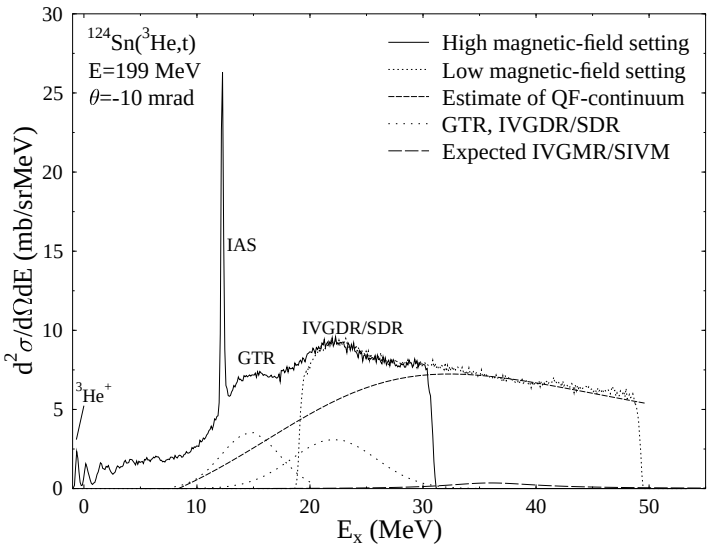

Figure 6.1: Singles excitation-energy spectrum from the ^{124}Sn(^{3}He,t) experiment. See text for more details.

different magnetic-field settings overlap well. Clearly, the IAS can be seen, as well as the GTR and IVGDR/SDR resonances. At higher excitation energies the spectrum is more or less structureless.

In the spectrum an estimation of the quasifree continuum is drawn. This curve has been calculated using equations (3.58) to (3.60) and furthermore $E_t = E_{projectile} - Q$. The parameters that were used are given in table 6.5. Jänecke et al. [114] and Erell et al. [21] performed fits of equation (3.58) to the data to find the various parameters. The parameters that are used in this work are either taken from or very similar to the ones by Jänecke et al. [114]. The parameter N was chosen as is usually done (section 3.7), namely by fitting the quasifree continuum to the full cross section at high excitation energies (in this case at 37 MeV). It can be seen that the estimate of the quasifree continuum above an excitation energy of 30 MeV describes the data reasonably well. For studying resonances at lower excitation energies, such as the GTR and IVGDR/SDR, this is a useful method (and for that purpose has also been used here), although it will lead to an underestimation of their cross sections. In principle, however, we do expect resonances at high excitation energy and thus choosing N so high is incorrect.

There is little indication for a contribution from two-step breakup-pickup processes to the continuum, assuming the phenomenological description of the quasifree contri-

Table 6.5: Values of parameters used in equation 3.58 to describe the quasifree continuum curve displayed in figure 6.1.

Parameter	Value
$E_{projectile}$	198.8 MeV
$E_t(g.s.)$	198.164 MeV
$E_t(free)$	199.56 MeV
S_p	7.088 MeV
B_{Coul}	12 MeV
E_{xn}	2 MeV[a]
$S_p+B_{Coul}+E_{xn}$	21.088 MeV[b]
W_L	22 MeV[c]
T	100 MeV[c]
N	44

[a]This value was calculated under the assumption that only the excess neutrons participate. On average they are approximately 2 MeV below the Fermi surface (using a harmonic-oscillator model).

[b]Jänecke et al. [114] find a value of approximately 23 MeV for ^{117}Sn and ^{120}Sn by performing fits to their data.

[c]Values were taken from Jänecke et al. [114].

bution to be correct. As described in section 3.7, the two-step contribution is expected to peak at 2/3 of the incoming triton energy (here: at an apparent $E_x \approx 63$ MeV) with a width of 1/3 of the beam energy (65 MeV). Indeed, above an excitation energy of 40 MeV, a slight rise of the cross section with respect to the quasifree curve can be seen, which could correspond to two-step contributions. Jänecke et al. estimated that approximately 5% of the total continuum cross section is caused by the two-step processes, in the same reaction at the same incoming energy [114]. Again, it must be noted that it is dangerous to draw strong conclusions, since all other contributions at these high energies are neglected. Moreover, the quasifree continuum curve is phenomenological, and the subtraction of instrumental background may introduce systematic errors.

The GTR is fragmented into several components which have already been determined experimentally [114, 117]. The authors found that the main component of the GTR lies at an excitation energy of 13.24±0.25 MeV, approximately 1 MeV higher than the IAS. The other fragments (the so-called *pygmy* resonances) which are due to core polarisation and back spin-flip [166], lie at excitation energies below that of the IAS. The reported width (Γ, assuming a Gaussian line shape) of the main component is 5.2±0.3 MeV [117]. Here, we find an excitation energy of 13.5±0.5 MeV and a width of 6±1 MeV, by fitting the peak height, position and width simultaneously for the GTR, the dipole resonances (see below) and the IAS in the excitation-energy spectrum. The contribution from the quasifree continuum processes was kept fixed as described above.

At even higher excitation energies one finds the isovector giant dipole resonance ($J^\pi=1^-$, $\Delta S=0$) and the three components of the spin-flip dipole resonance ($J^\pi=0^-$, 1^-, 2^-, $\Delta S=1$). The expected excitation energy of the IVGDR in the ^{124}Sn(^{3}He,t) reaction is approximately 22 MeV, where equation 2.5 is used and it is assumed that all strength can be attributed to the $T-1$ component (V_1=55 MeV is used).

Table 6.6: Strength parameters and ranges used for the various components of the effective potential [168].

Interaction	V [MeV]	Range [fm]
V_τ	3.46[a]	1.414
$V_{\sigma\tau}$	-3.5	1.414
$V_{T\tau}$	-3.0	0.878
$V_{LS\tau}$	0	-

[a]Determined from the present data, using the IAS (see text).

The SDR strength is split into three components with different J^π of 0^-, 1^- and 2^-. The 0^- state is highest and the 2^- state lowest in excitation energy due to the fact that the configurations that contribute most to the 0^- strength undergo a large repulsive spin-orbit interaction and are thus shifted up in energy [167]. Strength distributions for the three components in ^{124}Sn have been performed by Kuzmin and Soloviev [164]. They calculated the positions, with respect to the target ground state to be 23.8 MeV, 22.9 MeV and 20.1 MeV for the 0^-, 1^- and 2^- states, respectively. Their rather large widths make them overlap. It is expected that the 2^- state carries most of the strength, followed by respectively the 1^- and 0^- states. This is caused by the weighting of the operators by a factor $(2J+1)$. Kuzmin and Soloviev give a value for the combined centroid of 21.5 MeV. Other calculations give 23 MeV [167] and 27 MeV [36]. Pham et al. [117] reported the centroid of the various components to lie at an excitation energy of 21.1±0.6 MeV, with a width of 9 MeV. For the data presented here, the maximum of the combined bump lies at an excitation energy of 20.9±0.9 MeV and has a width of 8.8±1.5 MeV.

In the spectrum shown in figure 6.1, also an estimate for the combined SIVM/IVGMR cross section is drawn, based on the DWBA calculations and full exhaustion of the normal-mode strength. A Lorentzian centred around 36 MeV with a width (Γ) of 10 MeV is assumed. Clearly, uncertainties in the contribution from the quasifree continuum, the subtraction of instrumental background and, possibly, other resonances make it impossible to identify it in the singles spectrum.

6.2.2 Angular distributions and the difference spectrum

Resonances with different multipolarities usually have different angular distributions. Thus, by comparing spectra at different scattering angles, one may be able to distinguish the various multipoles. For this purpose, distorted wave calculations have been performed, using the code DW81 [61]. The wave functions of appendix A (table A.1 to A.3) were used as input. The parameters (table 6.6) that were used for the effective potentials (equations (3.35)) are taken from an analysis of the ^{12,13,14}C(^{3}He,t)^{12,13,14}N reactions at 200 MeV [168], except the value of V_τ which was deduced from the present data (see below).

The optical-model parameters for the incoming channel were taken from the literature (217 MeV ^{3}He on ^{120}Sn [56]). For the outgoing channel, the optical-potential well

Table 6.7: Optical-model parameters used in DWBA calculations for the ^{124}Sn(^{3}He,t)^{124}Sb reaction [56].

Particle	V_0 [MeV]	r_v [fm]	a_v [fm]	W_0 [MeV]	r_w [fm]	a_w [fm]	r_C [fm]
^{3}He	-70.9	1.27	0.86	-28.9	1.40	0.69	1.3
triton	-60.2	1.27	0.86	-24.6	1.40	0.69	1.3

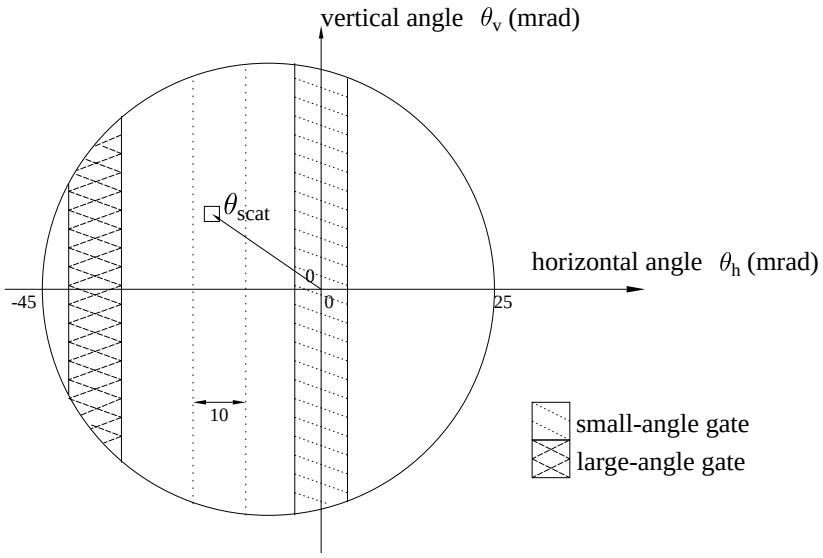

Figure 6.2: Entrance slit for the K600 spectrometer and the division into 10 mrad bins. The small-and large-angle gates that were used for generating difference spectra are also displayed

depths were taken 85% of the ones for the ^{3}He particles in the ingoing channel (see section 3.2.2). The values are listed in table 6.7.

The V_τ parameter was determined by fitting the calculated differential cross section to the measured differential cross section of the IAS. In the fitting procedure V_τ was the only free parameter. To this end, the opening angle of the spectrometer was divided into bins of 10 mrad in the horizontal direction, as displayed in figure 6.2.

The calculations were folded with the binsize, by dividing every bin into small squares of 0.5×0.5 mrad^2. The results for the IAS are shown in figure 6.3. The calculations, which are performed in the centre-of-mass frame, were transformed to the laboratory frame. A value for V_τ of 3.46±0.10 MeV was found.

Next, the distorted-wave calculations for the other resonances were performed. The results for giant resonance monopole transitions (IAS, GTR, IVGMR and SIVM),

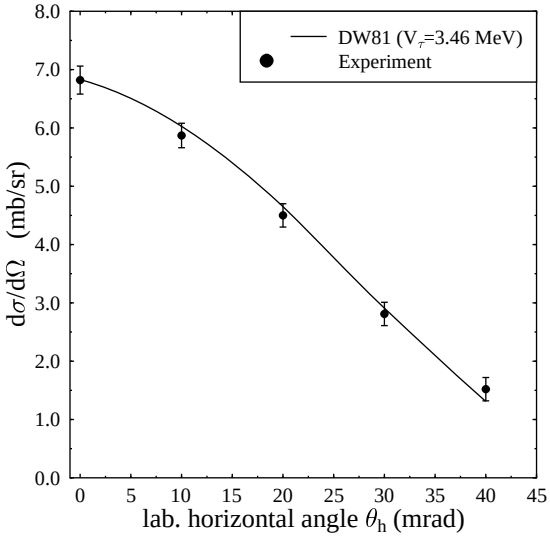

Figure 6.3: Differential cross section of the IAS obtained via the ^{124}Sn(^{3}He,t) reaction at E(^{3}He)=199 MeV. The solid curve is the result of a DWBA calculation in which the V_τ parameter is determined by fitting to the experimental data.

dipole transitions (IVGDR and SDR(0^-,1^-,2^-)) and IVGQR are displayed in figure 6.4(a), (b) and (c), respectively. In table 6.8 the excitation energies for the various resonances that were chosen are shown, as well as their cross sections at 0°. Furthermore, the momentum transfer at 0° is given.

Clearly, the monopole transitions (figure 6.4(a)) peak at 0° and have a minimum at around 3°. The minimum is more pronounced for the non-spin-flip transitions compared to the transitions in which spin-flip is involved. The cross sections at 0° scale almost linearly with the sum-rule strength since $V_{\sigma\tau}$ and V_τ are almost equal. The spin-flip cross sections are more than 3 times larger than the non-spin-flip cross sections. The growing importance of the $V_{T\tau}$ part in the effective potential with growing momentum transfer enhances the relative difference between SIVM and IVGMR with respect to that the GTR and IAS.

The dipole transitions (figure 6.4(b)) peak around 2.2° and have a local minimum at 0°. The SDR component with total angular momentum transfer of 2 is clearly dominant.

The angular distribution of the IVGQR (figure 6.4(c)) is more or less flat below a scattering angle of 4°. Since its cross section and excitation energy are comparable to those of the IVGMR and SIVM, the only possibility to distinguish between them is by comparing excitation-energy spectra at different scattering angles.

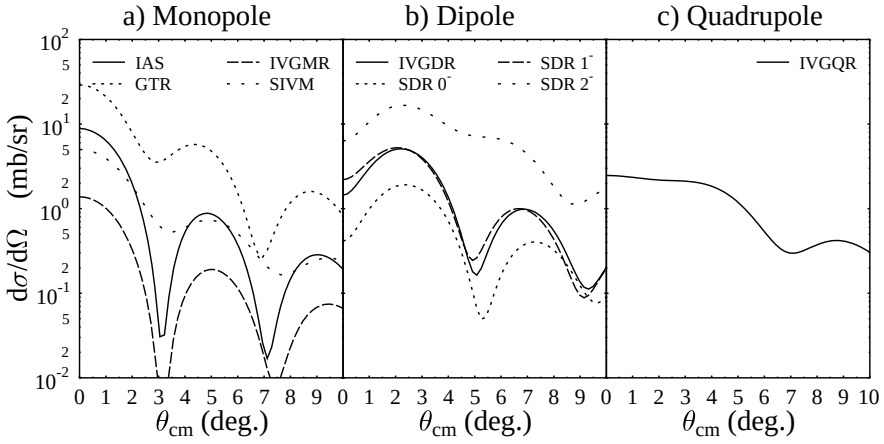

Figure 6.4: DWBA calculations for a) monopole, b) dipole and c) quadrupole transitions to the respective giant resonances at E(^{3}He)=199 MeV. The assumed excitation energies are given in table 6.8.

Table 6.8: Excitation energies and momentum transfers at 0° for the various resonances excited via the ^{124}Sn(^{3}He,t)^{124}Sb reaction at E(^{3}He)=199 MeV, as well as the resulting cross sections at 0°.

Resonance	J^π	E_x [MeV]	q(0°) [1/fm]	$d\sigma/d\Omega(0°)$ [mb/sr]
IAS	0^+	12.19	0.1749	8.85
GTR	1^+	13.25	0.1916	28.9
IVGDR	1^-	22.0	0.3159	1.44
SDR	0^-	23.8	0.3259	0.41
SDR	1^-	22.9	0.3417	2.20
SDR	2^-	20.1	0.2859	6.30
IVGMR	0^+	36.0	0.5084	1.38
SIVM	1^+	36.0	0.5084	5.01
IVGQR	2^+	33.0^a	0.4655	2.47

[a]Calculated using E_x=130*$A^{-1/3}$ [10], adding the excitation energy of the IAS and correcting for the fact that predominantly the $T-1$ component will be excited.

In order to investigate the contributions from the various resonances to the spectrum in figure 6.1, two 10 mrad wide bins were chosen, as indicated in figure 6.2; one around a horizontal scattering angle of 0° (small-angle gate) and one around 2° (large-angle gate). In principle, one could cut the whole aperture into two halves, which would result in better absolute statistics, but on the other hand this will result in a strongly overlapping range of scattering angles. It can be shown that, if only monopole contributions to the spectrum are considered, the relative error in the difference-spectra between the small-and large-angle gates is approximately the same for the two methods. However, since for the runs with a low magnetic-dipole-field setting a small part of the opening angle on the far right ($\theta_h > 22$ mrad) of the aperture was cut because of blocking by the beam stop, it was decided to use the gates as indicated in figure 6.2.

In figures 6.5(a) and 6.5(b) the spectra for, respectively, the small-angle and large-angle gates are shown. Spectrum 6.5(c) is the difference between the two. The peak at Q=0 MeV (apparent E_x=-0.636 MeV), due to $^3He^{++}$ particles that picked up an electron in the target, stems completely from the small-angle gate, as expected. The IAS at E_x=12.2 MeV also peaks strongly at forward angles. For the GTR the same holds and the excess in cross section between E_x=2 MeV and E_x=17 MeV is for a great part due to main component of the GTR at higher excitation energies and the pygmy resonances at lower excitation energies. The combination of the IVGDR and the three components of the SDR make up for the trough in the difference spectrum around E_x=20 MeV. Part of the excess in cross section due to the GTR is cancelled by the negative contributions to the difference spectrum from the dipole resonances. At even higher excitation energies there is basically no structure, indicating that indeed the SIVM and IVGMR can not be distinguished in this manner (the expected contribution in the difference spectrum due to the IVGMR and SIVM is drawn). Moreover, the difference spectrum indicates that the angular distribution of the quasifree continuum is more or less flat. The fact that instrumental background had to be subtracted, makes the interpretation of the difference spectrum even more questionable, since it increases the absolute statistical errors and may introduce systematic errors.

6.3 Coincidence data

In an attempt to separate the resonances at high excitation energies from the quasifree continuum, coincidence measurements were performed between tritons in the focal plane and neutrons emitted at backward angles. The quasifree processes yield tritons in coincidence with protons around the direction of the momentum transfer and the target nucleus is left behind in low-lying neutron-hole states. Emission of neutrons is thus unlikely, because of the relatively high neutron-separation energy of approximately 7 MeV.

As discussed in section 3.3, various modes of decay of an excited nucleus compete with each other (direct, statistical or semi-direct decay). On first thought, one would expect that at high excitation energies decay would largely occur in a statistical manner. This is due to the fact that direct decay requires a strong overlap between the excited state and the final state in the residual nucleus, and this is less likely at

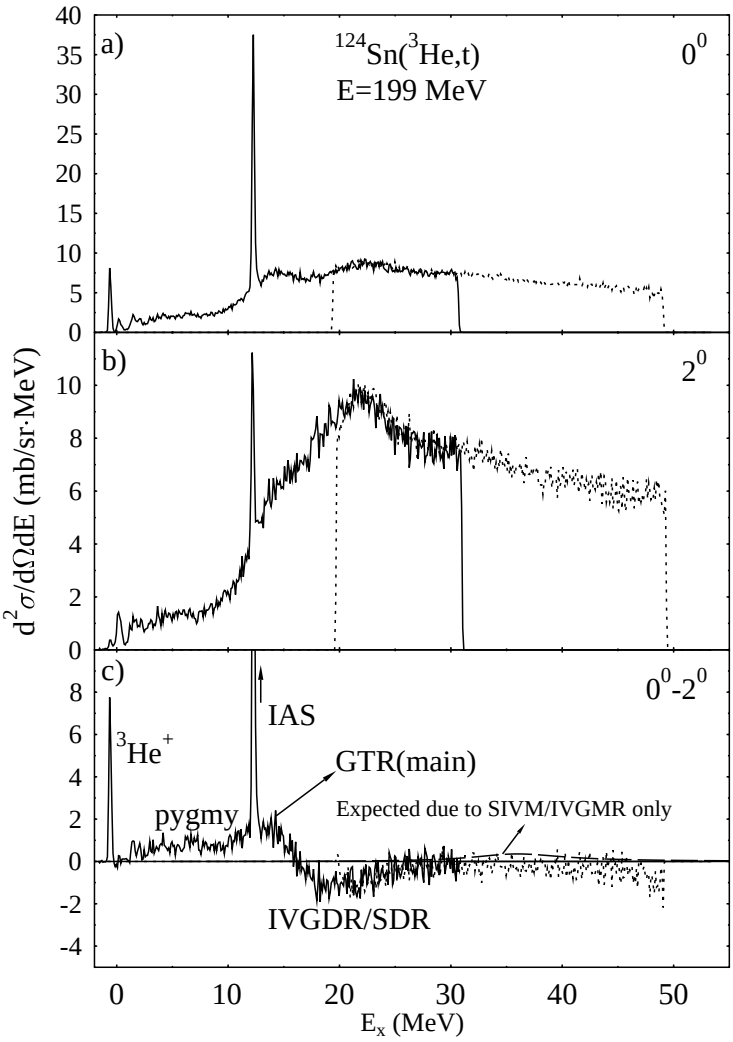

Figure 6.5: Excitation-energy spectra for (a) the small-angle triton gate and (b) the large-angle triton gate; (c) is the difference spectrum between (a) and (b). An estimate of the combined contribution from IVGMR and SIVM is drawn in this spectrum.

higher excitation energies. On the other hand, for giant resonances, this is not so obvious. The simple, collective 1p-1h structure of these charge-exchange resonances at high excitation energies could result in a significant overlap with the ground state and low-lying excited neutron-hole states of the residual nucleus and thus a non-negligible direct-decay rate. Such effects have for example been reported by Akimune et al. [38, 39] who found a branching ratio for direct proton emission of the SDR in ^{208}Bi of 13.4±3.9%[1]. This rather large branching ratio for decay by proton emission forms the basis for the experiment described in chapter 7.

The direct-decay channel will be dominated by decay by proton emission due to the 1 proton-particle, 1 neutron-hole (1πp-1νh) structure of the states excited in the (^{3}He,t) reaction. For direct decay from states at higher excitation energies, the Coulomb barrier is easier to overcome, which is another reason that direct decay by proton emission can not be completely neglected.

Statistical decay will occur for more than 99% through emission of neutrons and γ-rays, since low-energy protons are blocked by the Coulomb barrier (its height is approximately 12 MeV for ^{124}Sb). Small contributions to the decay due to semi-direct neutron emission are neglected in the analysis. The neutron-emission multiplicity can then be calculated using the Hauser-Feshbach formalism incorporated in the code CASCADE, as described in section 3.3.2.

Investigating the decay by γ-ray emission is difficult, since it is hard to determine in which stage of the decay cascade a γ-ray is produced. The gross structures can be described well, as for example shown by Roberts et al. [153], but the determination of the multiplicity is difficult and is not attempted here. In the experiment described here, thin lead sheets of 2 mm thickness were put in front of the liquid scintillators to reduce the count rate due to γ-rays (γ-rays with an energy below 0.3 MeV are stopped by the sheets. Since the energy of the γ-rays produced in the decay cascade have a peak energy ranging from $\sim$ 0.5 MeV (for the lowest excitation energies in ^{124}Sb) to $\sim$ 3 MeV (for an excitation energy in ^{124}Sb of 50 MeV), they are still seen by the neutron detectors, resulting in figure 6.6(b)of the next section).

6.3.1 Non-corrected coincidence spectra

By separating neutron-coincident and γ-ray-coincident events, as discussed in section 5.3, one can construct the coincident excitation-energy spectra shown in figures 6.6(a) (for the coincidence with neutrons) and 6.6(b) (for the coincidence with γ-rays). In figure 6.6, also the thresholds for decay by neutron emission are drawn. The exact values of the decay thresholds are given in table 6.9. At lower excitation energies it can clearly be seen that when the thresholds for one and two neutron emission are reached, the number of neutron-coincidences rises strongly, whereas the number of γ-coincidences drops. This is logical, since the two channels are in competition. At higher excitation energies, the structure becomes less pronounced due to the convolution over the phase spaces for multiple consecutive neutron emission [153]. In any case, it is now

[1] In reference [38] a value of 14.1±4.2% is reported. After reanalysis the percentage has changed slightly to the quoted value.

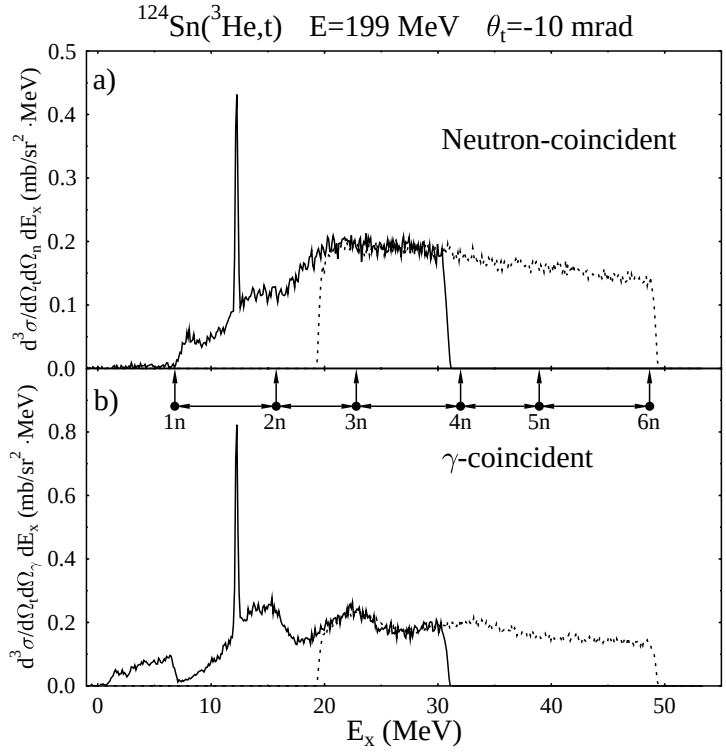

Figure 6.6: Neutron (a) and γ-ray (b) coincidence excitation-energy spectra for the ^{124}Sn(^{3}He,t)^{124}Sb* at E(^{3}He)=199 MeV, uncorrected for multiplicity and efficiency. The thresholds for decay by neutron emission are also indicated.

Table 6.9: Thresholds for decay by multiple neutron emission. The values are given with respect to the groundstate of ^{124}Sb.

decay by n neutrons	E_x [MeV]
1	6.47
2	15.43
3	22.24
4	31.48
5	38.50
6	48.05

clear why one has to correct for multiplicity; the structures observed in the spectra are partly due to this effect.

The decay by particle emission of the IAS is somewhat special. If isospin would be a good quantum number, decay through emission by neutrons is isospin-forbidden; decay by particle emission could then only occur by protons. However, because of the charge-dependent Coulomb force, mixing between the IAS ($\mid T, T-1\rangle$) with states of lower isospin ($\mid T-1, T-1\rangle$) is possible, and, for heavy nuclei, this is believed to be mediated via the IVGMR (see also section 4.4). The mixing makes decay by neutron emission possible. Since the Coulomb barrier is, for ^{124}Sb, almost as high as the excitation energy of the IAS, and the neutron channel is wide open because of the relative large excess of neutrons, this decay channel will be dominant. Jänecke et al. discussed the systematics for a large number of Sn (and Te) isotopes [169]. After the correction for detection efficiencies the branching ratio for decay by neutron emission from the IAS in ^{124}Sb can be compared to the value found by Jänecke et al. (see next section).

6.3.2 Corrections for emission multiplicity and detection efficiency

Multiplicity calculations were performed using the computer code CASCADE. The formalism is described in section 3.2.2. The level density for each of the nuclei that appears in the cascade serves as input. For this purpose, the excitation energy range is divided into four regions. In the first region, the density is calculated from experimentally known levels (n_1) up to an excitation energy E_1 (see table 6.10). In the second region, up to $E_2 = 60A^{-1/3} \approx 12$ MeV, the back-shifted Fermi-gas model is used. For the highest region, starting at $E_3 = 120A^{-1/3} \approx 24$ MeV, the level density was calculated using a liquid-drop model. In the range between regions 2 and 4 a smooth interpolation of level densities is used. In table 6.10 the relevant parameters are displayed. For region 1 the number of levels (n_1) up to an excitation energy E_1 are given. For region 2, the level-density parameter, a_2 (level-density parameter in equation (3.48) a=A/a_2) and the fictive ground state Δ_2 are displayed [96]. The same parameters are shown for region 4, but now the level-density parameter, a_4 has been kept at 8 MeV^{-1} and the fictive ground state is calculated from the liquid-drop model [97].

The result of these calculations at a given excitation energy is a Maxwellian distribution as a function of neutron energy (except at low excitation energies where the target nucleus decays to specific levels which are relatively far apart from each other). The integral of this distribution, relative to the singles cross sections, gives the multiplicity.

The Maxwellian distributions have to be folded with the detection efficiency. The results, at an excitation energy of 30 MeV and for different detection thresholds, is shown in figure 6.7(a). The full curve is the result without the detection efficiency taken into account. Even with a relatively low threshold of 25 keVee, a large part of the neutrons is not seen by the detector. In figure 6.7(b), the multiplicity curves for the excitation-energy range up to 50 MeV is shown. Calculations were performed in steps of excitation energy of 0.1 MeV, every bin being the integral of a curve like the

Table 6.10: Level-density and pairing parameters used for CASCADE calculations.

Nucleus	Region 1		Region 2			Region 4		
	E_1 [MeV]	n_1	E_2 [MeV]	a_2 [MeV^{-1}]	Δ_2 [MeV]	E_3 [MeV]	a_4 [MeV^{-1}]	Δ_4 [MeV]
^{124}Sb	0.40	17	12.0	8.83	-1.39	24.0	8	-3.91
^{123}Sb^a	1.10	5	12.0	8.40	-1.30	24.0	8	-3.13
^{122}Sb	0.48	26	12.0	8.18	-1.21	24.0	8	-4.30
^{121}Sb^a	1.33	10	12.0	8.06	-1.12	24.0	8	-3.44
^{120}Sb^a	0.45	17	12.0	8.00	-1.03	24.0	8	-4.56
^{119}Sb^a	1.68	22	12.0	7.93	0.	24.0	8	-3.72
^{123}Sn	1.12	15	12.0	8.82	0.970	24.0	8	-2.43
^{122}Sn^a	2.80	20	12.0	8.72	1.210	24.0	8	-1.59

^{a}a_2 and Δ_2 are interpolated values

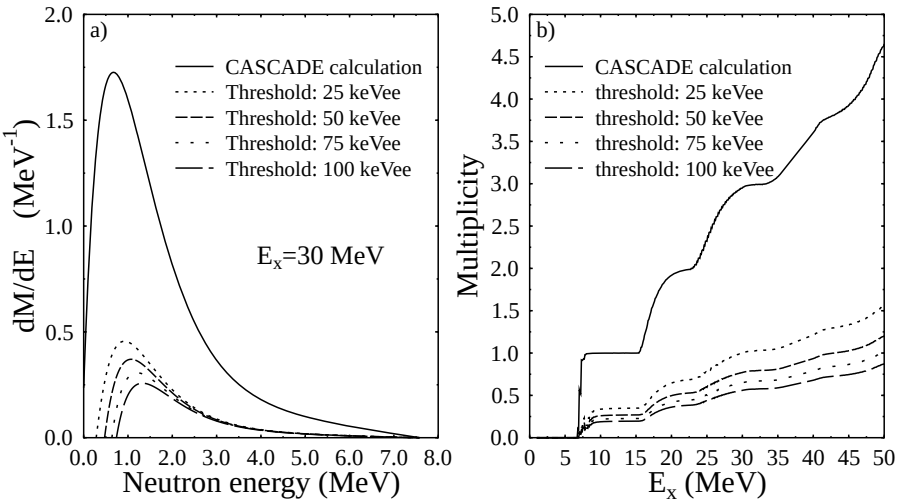

Figure 6.7: Neutron spectra for decay from an excitation energy of 30 MeV as a function of detection threshold (a). The multiplicity curve is shown in (b). Again the effect of a change in detection threshold is shown.

ones in figure 6.7(a).

For the multiplicity curve without the detection efficiency taken into account (full line), one can see that at higher excitation energies, the steps due to the thresholds for multi-neutron emission get less distinct. This is even more so after the folding with the detection efficiency. At higher excitation energies, the corrected curves get 'flatter' with increasing detection threshold. Only at lower excitation energies, steps can be distinguished. This effect is also visible in the experimentally found neutron-coincident excitation-energy spectrum, displayed in figure 6.6(a).

It is estimated that the error made in the determination of the thresholds of each detector is approximately 10 keVee. At a threshold of 50 keVee, the average threshold of the detectors in this experiment, such an error results in a 10% deviation of the efficiency-corrected multiplicity. For example, at an excitation energy of 30 MeV, where the multiplicity as calculated using the code CASCADE is approximately 3, a threshold of 50 keVee results in a corrected multiplicity of 0.53, whereas a threshold of 40 keVee results in a corrected multiplicity of 0.59. This error is systematic in nature (for example due to a wrong choice in the procedure for determining the exact location of the Compton edge) and in that case a shift of the corrected multiplicities in the same direction for each detector is to be expected.

An efficiency-corrected multiplicity curve was determined for every detector and also separately for the high and low magnetic-field runs, since the thresholds had shifted in between. The experimentally found coincidence spectrum for each detector was divided by the efficiency-corrected multiplicity curve. Finally, the spectra from all detectors were added. The result is shown in figure 6.8. Also, an estimate for the combined IVGMR/SIVM cross section is drawn, assuming an equal branching ratio for statistical neutron decay for the IAS and the IVGMR /SIVM. It was found that the branching ratio for decay by emission of neutrons of the IAS was (89±2)%, where the error is statistical only. This is in agreement with the value of (91.1±5.1)% calculated by Jänecke et al. [169]. For the whole excitation-energy range between 10 and 16 MeV a branching ratio of 90% is found, indicating that also the GTR decays mainly by neutron emission. Decay by neutron emission from the dipole resonances can also be seen clearly.

It is surprising to see that still a large background is present in the coincidence spectrum. Even at excitation energies above 30 MeV, the coincidence cross section (if a uniform distribution over 4π is assumed) makes up for approximately 50% of the singles cross section. Therefore, the expected contribution from the monopole resonances, as indicated by the Lorentzian in figure 6.8, is still small compared to the total cross section. It was mentioned before that a small fraction of the continuum is not due to quasifree processes, and thus may decay by neutron emission at backward angles. The coincidence data indicates that this fraction of the continuum is much larger than anticipated.

In order to identify monopole strength, excitation-energy spectra from the small- and large-angle gates were compared. In figure 6.9 the coincidence excitation-energy spectra belonging to the two gates are displayed. The procedure followed is the same as for the singles spectra, except that a binning of 1 MeV has been chosen. The difference spectrum between spectra shown in figures 6.9(a) and 6.9(b) is displayed in figure

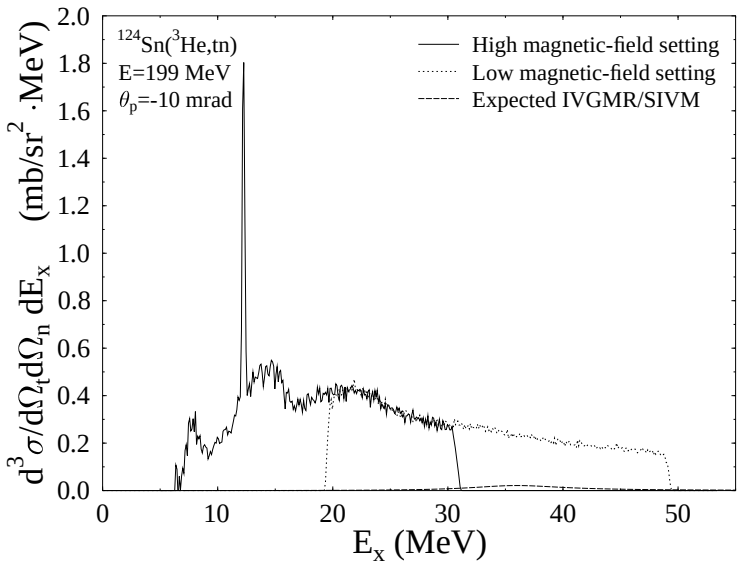

Figure 6.8: Detection-efficiency and multiplicity corrected excitation-energy spectrum for the neutron-coincident ^{124}Sn(^{3}He,t) spectrum. A Lorentzian estimate for the IVGMR/SIVM is also drawn (see text).

6.10(a). The error bars (statistical only) are also drawn. The results are similar to the singles difference spectrum (figure 6.5(c)). There is no indication for any monopole strength at higher excitation energies. Again, an estimate for the cross section of the IVGMR/SIVM has been made, based on the assumptions that the branching ratio for decay by neutron emission for these resonances is equal to this branching ratio for the IAS and full exhaustion of the normal-mode sum-rule strength. This is shown as the Lorentzian curve around $E_x = 36$ MeV. The structures due to the IAS and GTR (positive) and the IVGDR/SDR (negative) are clearly visible.

An excess in cross section at high excitation energies, indicating monopole strength, can not be identified. To investigate whether a strong fragmentation of the strength is the cause, the relevant energy range has been rebinned into 4 MeV bins as displayed in 6.10(b). Again, an estimate for the IVGMR/SIVM is displayed as a Lorentzian at $E_x = 36$ MeV, under the same assumptions as in figure 6.10(a). The data, however, are clearly consistent with zero, indicating that no significant monopole strength is observed in the present data (the reduced χ^2 for a fit to zero of the difference spectra in figure 6.10(a) between 25 and 50 MeV is 1.2). Disregarding any presence of contributions with a multipolarity larger than zero in this difference spectrum at high excitation energies and assuming the Lorentzian line shape as shown in figure 6.10 for

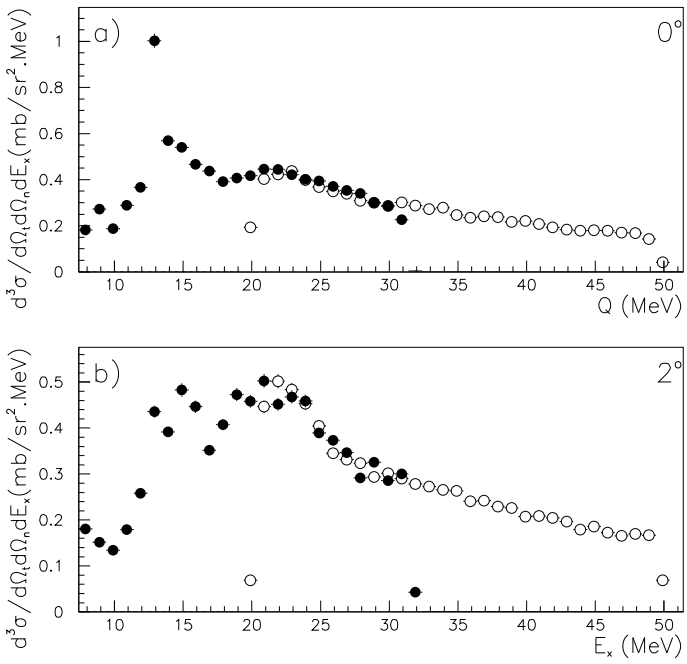

Figure 6.9: Coincidence excitation-energy spectra for small- (a) and large- (b) angle gates. The filled points are the results from the high-magnetic-field runs, the open points for the low-magnetic-field runs.

the distribution of isovector monopole strength, it can be deduced that, with a certainty of 95%, the cross section for the isovector monopole resonances is below 20% of the expected cross section.

6.3.3 Conclusions

The principal idea of the experiment was that the continuum background could be removed by requiring coincidences with neutrons at backward angles. It is clear that this is not the case. It is, therefore, impossible to find a broad resonance at high excitation energies in this manner.

It has already been mentioned that the phenomenological description commonly used for the quasifree continuum tends to give an overestimation. At least a fraction of the cross section at high excitation energies is due to nuclear excitations, including the monopole resonances. Since these excitations mainly decay by neutron emission (also at backward angles), a realistic interpretation of the data could be that multipole resonances and/or distributed strength make up for a considerable part of the continuum.

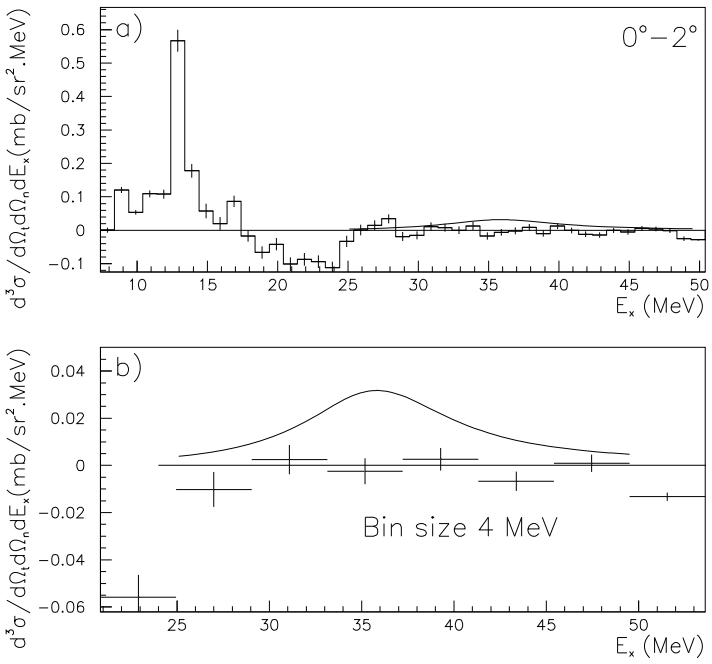

Figure 6.10: Difference spectra for the coincidence data. In a) with a binning of 1 MeV and in b) with a binning of 4 MeV. In both cases an estimate for the SIVM/IVGMR is drawn (see text).

This has not been investigated any further in the present work.

Secondly, it could be argued that the quasifree processes which are thought to be responsible for the bulk of the cross section at high excitation energies do not only involve neutrons in the outer-most shells (the excess neutrons) of the target nucleus, but for a large fraction also deeper-lying neutrons. Therefore, the remaining nucleus could be in a rather highly-excited neutron-hole state and thus decay statistically by neutron emission. However, a strong excitation of these deep-hole states relative to valence-shell excitations is not expected [117]. Also, more complicated, two or more-step, processes that result in the emission of neutrons at backward angles, could be more important than expected.

Of course, a combination of the above explanations could be true and together contribute to the coincidence cross section at high-excitation energies. Thus the problem still remains the insufficient understanding of the processes that contribute to the continuum. It also has to be realised that if indeed a large fraction of the continuum stems from processes involving neutrons that are part of the core of the target nucleus, or from two-step processes, the subsequent decay by neutron-emission is hard to predict

since the excitation energy is unknown. Therefore, blindly correcting for multiplicity and efficiency effects under the assumption that the emission cascade starts at an excitation energy equal to that determined from the triton energy spectrum is wrong. The only way to solve this problem is by measuring the energy of the neutrons by means of time of flight and covering a large solid angle in a kinematically complete experiment.

On the other hand, a possible error in the correction procedure for multiplicity and detection efficiency cannot make up for the fact that no monopole strength whatsoever is found at high excitation energies. A cross section which is consistent with zero in the difference spectrum between excitation-energy spectra at 0° and 2° will remain zero, even if the correction changes. It is therefore interesting to realise which other factors could possibly explain why no monopole strength was found.

The Lorentzian curves, that serve as estimates for the resonances we try to find, are drawn under the assumption that their width (Γ) is 10 MeV. If the width is much larger, as suggested by Auerbach and Klein [33] and results from the π-exchange data [21] (see table 6.2), finding the strength would be much more difficult. It must also be realised that if the monopole resonances are located at higher excitation energies, their cross sections will drop. This is due to the fact that the momentum transfer grows with excitation energy and thus that monopole transitions are less likely to occur.

The assumption that the branching ratio for statistical decay of the SIVM and IVGMR is similar to that of the IAS might also be wrong. If the decay by direct proton emission accounts for a large part of the branching ratio, the estimates which are used, are too high. Furthermore, as was shown in the beginning of this chapter, the estimates for the transition strengths of the SIVM and IVGMR in the normal-mode formalism are approximately 40% higher than the HF-RPA estimates, indicating that the Lorentzian estimates which were used in this chapter are too high.

Finally, the problems in the ray-tracing procedure for the vertical direction has made the difference-of-spectra method less sensitive than it could have been and thus making it harder to identify monopole strength.

7. The Pb(^{3}He,tp) experiment at KVI

After the negative result of the experiment performed at IUCF, presented in the previous chapter, it was decided to do an experiment at KVI. The experiment is based on the same ideas, but instead of requiring coincidences between tritons and neutrons, coincidences between tritons and protons were investigated.

Statistical decay from the SIVM and IVGMR in heavy nuclei (Z>40) by emission of protons is expected to be very small because of hindrance by the Coulomb barrier. However, since the resonances under study are situated far above the Coulomb barrier for reactions in the $T_z = -1$ direction, emission of protons through (semi-)direct decay is expected to be of measurable magnitude. Evidence for a strong direct-decay component is given by experimental work performed at RCNP, Osaka, where a branching ratio of (13.4±3.9)% was found for the direct decay by proton emission from the SDR in ^{208}Bi, excited via the ^{208}Pb(^{3}He,t) reaction at 450 MeV [38, 39]. For the direct decay by proton emission from the GTR a branching ratio of (4.9±1.3)% was measured. The Coulomb barrier is relatively less important for the SDR than for the GTR. This will also be true for the higher-lying SIVM and IVGMR. Calculations in the framework of the continuum random-phase approximation (continuum RPA) for the partial escape widths of giant resonances have been carried out [76, 77] (see also section 3.3.1) and results are comparable to the experimental results published in reference [38]. Similar calculations have been performed for the escape width ($\Gamma^{\uparrow}$) of the IVGMR in ^{208}Bi [79], with a result of 11±2 MeV. This would mean that the branching ratio for decay by direct proton emission is quite high ($P^{\uparrow} \approx 50\%$ if the total width of the IVGMR in ^{208}Bi is 20 MeV).

For the experiment performed at KVI, it was intended to use ^{208}Pb as target, but due to an unfortunate administrative error, a ^{nat}Pb target (52.3% ^{208}Pb, 22.6% ^{207}Pb, 23.6% ^{206}Pb, 1.48% ^{204}Pb) was used instead. For the excitation strength and the mean excitation energy of the giant resonances this does not matter much, but because of limited energy resolution, it will be impossible to distinguish direct decay by proton emission to separate low-lying neutron-hole states in the final nuclei. For the SIVM and IVGMR this would have been very difficult in any case, because of the fact that at these high energies the protons emitted in the direct-decay process will punch through the 5 mm thick Si(Li)-detectors and resolution will be degraded (see section 5.4). The Q-values for the excitation of the IAS in the (^{3}He,t) reaction for the four components in ^{nat}Pb are very similar (-18.061±0.004 MeV for ^{208}Pb, −18.115±0.004 MeV for ^{207}Pb, −18.163±0.004 MeV for ^{206}Pb and −18.273±0.006 MeV for ^{204}Pb [170]). Also, the proton-emission thresholds for the various Bi isotopes populated in (^{3}He,t) reaction are very similar; the Q-values for decay by proton emission from ^{208}Bi, ^{207}Bi, ^{206}Bi and ^{204}Bi are -3.71 MeV, -3.55 MeV, -3.54 MeV and -3.21 MeV, respectively. In figure 7.1, the relevant level scheme for the (^{3}He,t) reaction on ^{208}Pb is shown. For the IAS, the

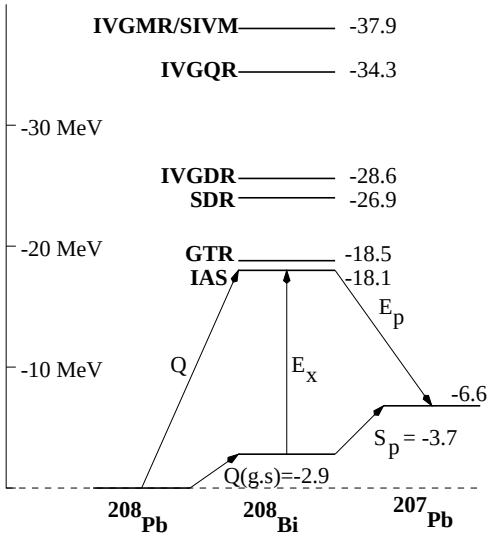

Figure 7.1: Level scheme in which the (expected) peak position for the various resonances excited through the (^{3}He,t) on ^{208}Pb are shown (see also section 7.2.1). For the IAS, the Q-value (Q), excitation energy (E_x) and proton energy (E_p) corresponding to decay to the groundstate of ^{207}Pb are indicated by arrows. The Q-value for the ^{208}Pb(^{3}He,t) reaction to the groundstate of ^{208}Bi ($Q(g.s)$), the proton separation energy (S_p) in ^{208}Bi and the positions of the various resonances are nearly equal to those for the same reaction on other Pb-isotopes (see text).

Q-value, excitation energy (E_x) and proton energy (E_p) corresponding to direct decay to the groundstate of ^{207}Pb are indicated. The Q-values for the various resonances (the widths are not indicated) are discussed later in this chapter.

The data-acquisition system for the focal-plane detector is developed at *IPN Orsay* [171, 148]. The OASIS package [172], especially developed for nuclear physics experiments, is used for the online analysis. Offline analysis was done using the PAW package [173] developed at CERN. A code, written originally for transforming data from singles experiments with the Orsay focal-plane detection system into Ntuples [174], was extended to handle coincidence data.

The first part of this chapter will deal with predictions. After that the singles and coincidences data will be discussed.

7.1 Predictions

Predictions similar to the ones in the previous chapter can be made for the monopole resonances excited via the Pb(^{3}He,t) reaction. The calculations were performed only for ^{208}Pb and not for the other isotopes present in the target. Differences will be small, however. By calculating the isospin-coupling (Clebsch-Gordan) coefficients for the

Table 7.1: Predicted widths of the IVGMR in ^{208}Bi.

Method	Γ [MeV]	Ref.
Dissipative term in Euler eq. (eq. 2.7)	4.4	[45]
Width of the IAS, β =0 (section 4.4)	6.2	[134]
Width of the IAS, $\beta \neq$0 (section 4.4)	7.8	[134]
HF-RPA approach	15	[33]
(π^+, π^0) data on ^{208}Pb	15±6[a]	[21]

[a]Cross section is consistent with zero [21]

^{208}Pb(^{3}He,t) reaction, one finds that the component with isospin $(T-1)$ is, compared to the T and $(T+1)$ components, even more strongly excited than was the case for the ^{124}Sn(^{3}He,t) reaction. This is due to the larger asymmetry between the number of neutrons and protons. A ratio of 1:45:989 is found for $B^{T+1,T-1} : B^{T,T-1} : B^{T-1,T-1}$. Applying the simple estimates for the reduced transition probabilities, (equation (3.50) [98]) the ratio becomes 1:58:1533.

Using equation (3.53) and the values for the parameters V_0 and V_1 given in the previous chapter one can calculate that an excitation energy of 35±3 MeV for the IVGMR in ^{208}Pb is to be expected.

Estimates for the width of the IVGMR excited through the ^{208}Pb(^{3}He,t) reaction are given in table 7.1. As was the case in the previous chapter, the various estimates differ strongly. The only available data, from the (π^+, π^0) experiment [21], are unreliable since the cross section itself is consistent with zero. The authors give for the excitation energy a value of 37.2±3.5 MeV. It can be remarked that the various estimates for the width are lower than the corresponding values calculated for the IVGMR in ^{124}Sb.

The total transition strengths of the various resonances were calculated. Calculations in the normal-mode framework and via a microscopic approach are compared in table 7.2. Since ^{208}Pb is a doubly-closed-shell nucleus, the occupation numbers of all neutron and proton shells were assumed to be 1 for the calculations performed in the normal-mode framework.

The RPA calculations for the SIVM and IVGMR are strongly reduced with respect to the normal-mode values, due to the fact that groundstate correlations are not taken into account in the case of the normal-mode calculations. The effect is slightly stronger than was the case in the excitation of the IVGMR and SIVM in ^{124}Sb. For the IVGMR the reduction is ∼50% and for the SIVM the reduction is ∼65%.

7.2 Singles data

The experiment was performed with the BBS spectrometer at KVI, which was set at -1° (the beam entered the spectrometer along its shorter curvature). The angle-defining slit shown in figure 5.5(b) was put in front of the spectrometer opening. The Pb target had a thickness of 7.8 mg/cm^2. The focal-plane detection efficiency was 98% (determined by comparing the accepted events with the number of triggers from

Table 7.2: Transition-strength calculations for various resonances excited through the ^{208}Pb(^{3}He,t)^{208}Bi reaction, using a normal-mode procedure (column 2) and the comparison with HF-RPA calculations by Auerbach and Klein [33, 36], Auerbach, Klein and Zamick [165] (column 3) and Kuzmin and Soloviev [164] (column 4).

Resonance	Normal modes	HF-RPA	
		[165, 33, 36][a]	[164]
IAS	3.5		
GTR	10.5	9.2	
IVGMR	2229 fm^4	1000 fm^4	
SIVM	6146 fm^4	1776 fm^4	
IVGDR	432.8 fm^2	305.7 fm^2	
SDR 0^-	178.2 fm^2	133.1 fm^2	134.2 fm^2
SDR 1^-	438.8 fm^2	350.0 fm^2	392.0 fm^2
SDR 2^-	744.5 fm^2	540.5 fm^2	609.0 fm^2
IVGQR	28440 fm^4	24070 fm^4	

[a]The values taken from the literature have been recalculated to match the operator definition of equation (3.37).

the scintillator detectors) and the electronics live-time was 99%. Singles data were down scaled by a factor of 16. Ray-trace measurements were performed as discussed in sections 5.2.1 and 5.2.3. Because of a failing strip on the low-momentum side of the focal plane, it was decided to measure the $|Q|$-value spectrum between 17 MeV and 48 MeV (in fact, data were available from $|Q|\approx$14 MeV to $|Q|\approx$60 MeV, but below $|Q|$=17 MeV and above $|Q|$=48 MeV part of the acceptance was cut).

A large amount of instrumental background (15% of the total measured events) was present in the singles spectra, most probably due to scattering from the beam stop. Surprisingly, hardly any instrumental background could be detected with an empty frame, indicating that it was not related to the target frame. A large fraction of the instrumental background (80%) could be removed in the offline analysis, by setting gates on the ΔE-E spectra from the scintillators, and on the spectra for the scattering angles in the horizontal and vertical directions. Still, some instrumental background was present in the data, mainly above $|Q|$-values above 35 MeV. It could therefore not be removed in the analysis. In the coincidence spectra hardly any instrumental background was present (<0.5%) and mostly random in character. In figure 7.2 the singles $|Q|$-value spectrum is displayed; the ground-state Q-value of the (^{3}He,t) reaction on ^{208}Pb is -2.897 MeV, on ^{207}Pb it is -2.41 MeV and on ^{206}Pb it is -3.77 MeV. The IAS at $|Q|$=18.1 MeV and a large bump with a centroid at $|Q|$=26 MeV due to the IVGDR and the three components of the SDR can be seen. The spectrum is very similar to the singles spectrum measured via the ^{124}Sn(^{3}He,t) reaction (figure 6.1).

An estimate for the quasifree continuum is drawn in the spectrum, based on the procedure described by Erell et al. [21]. The curve is drawn under the assumption that the cross section at high $|Q|$ values is essentially due to quasifree processes. The parameters used in the description (see equation (3.58)) are listed in table 7.3.

The parameters T and W_L were taken from the ^{120}Sn(^{3}He,t)^{120}Sb data by Jänecke

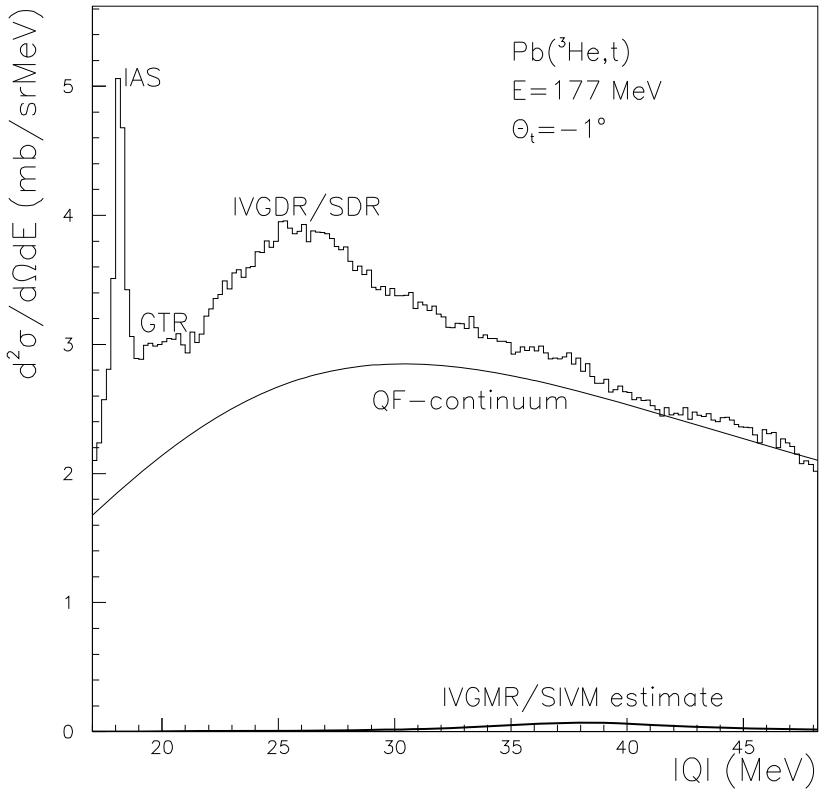

Figure 7.2: Singles spectrum from the Pb(^{3}He,t) experiment. Estimates of the quasifree continuum and the IVGMR/SIVM are also displayed (see text for more details). Note that, especially above $|Q|$=35 MeV, there is still some instrumental background present in the spectrum, which could not be removed by applying software gates.

Table 7.3: Parameters used in equation 3.58 to describe the quasifree-continuum curve displayed in figure 7.2.

Parameter	Value
$E_{projectile}$	177.0 MeV
$E_t(g.s.)$	174.11 MeV
$E_t(free)$	177.76 MeV
S_p	3.707 MeV
B_{Coul}	14 MeV
E_{xn}	2 MeV[a]
S_p+B_{Coul}+E_{xn}	19.707 MeV
W_L	22 MeV[b]
T	100 MeV[b]
N	17

[a]This value was calculated under the assumption that only the excess neutrons participate. On average they are approximately 2 MeV below the Fermi surface (using a harmonic-oscillator model).
[b]Values were taken from Jänecke et al. [114].

et al. [114]. Akimune et al. [38] also used these values in the analysis of the ^{208}Pb(^{3}He,t) reaction at E(^{3}He)=450 MeV.

It was difficult to perform a fitting procedure for the GTR and the dipole resonances. The GTR, which is expected to peak at $|Q|$=18.5±0.2 MeV with a width Γ=3.72±0.25 MeV (for ^{208}Pb [38]), is partly lying outside the range covered by the focal-plane detector. The fitting procedure for the dipole strength at $|Q|\approx$26 MeV is therefore also difficult, since it overlaps the GTR. At E(^{3}He)=450 MeV, where the total dipole cross section is dominated by spin-flip transitions, the dipole bump peaks at $|Q|$=24.0±0.8 MeV [38], with a width Γ=8.4±1.7 MeV. Kuzmin and Soloviev [164] predict that the combined SDR peaks at $|Q|$=24.8 MeV (for the three components they calculate the following peak positions: 0^- at 27.80 MeV, 1^- at 25.58 MeV and 2^- at 22.01 MeV). The IVGDR is expected to peak at $|Q|\approx$25.7 MeV, using equation (2.5), and assuming that only the component with lowest isospin $(T-1)$ is excited.

In figure 7.2 also an estimate for the combined contribution from the IVGMR and SIVM is shown. A Lorentzian shape, centred around $|Q|$=38 MeV and having a width Γ=10 MeV, is assumed. It is clear that it would be extremely difficult to distinguish it from the continuum, even if no instrumental background was present in the spectrum.

7.2.1 Angular distributions

Since there is some remaining instrumental background in the singles spectra, interpretation of the spectra in terms of a multipole decomposition is difficult. Furthermore, since below $|Q|$=27 MeV no information about the vertical scattering angle is available, difference spectra in the lower excitation-energy range can only be made by gating on angles in the horizontal direction. Because of the special slit used (figure 5.5(b)), and the relatively large angular range in the vertical direction (i.e. from -60 mrad to +60 mrad), interpretation of such difference spectra is not straightforward. Therefore, only

Table 7.4: Optical-model parameters used in the DWBA calculation for the ^{208}Pb(^{3}He,t)^{208}Bi reaction at 177 MeV [56].

Particle	V_0 [MeV]	r_v [fm]	a_v [fm]	W_0 [MeV]	r_w [fm]	a_w [fm]	r_C [fm]
^{3}He	-78.0	1.25	0.86	-24.9	1.43	0.81	1.3
triton	-66.3	1.25	0.86	-20.5	1.43	0.81	1.3

the angular distribution of the IAS was thoroughly investigated. Because it is such a well-defined, strong peak and has a very distinct angular distribution, instrumental background will hardly influence the analysis.

To investigate the angular distribution of the IAS, the horizontal opening angle was divided into six, 11 mrad wide bins (the full horizontal opening angle is 66 mrad). Distorted-wave calculations were performed using the code DW81 [61]. The wave function for the IAS is given in appendix A (table A.4) and is the result of a calculation in the normal-mode framework (see also table 7.2). It is assumed that the cross sections for the excitation of the IAS through the (^{3}He,t) reaction for all Pb isotopes present in the ^{nat}Pb target are equal, even though the transition strength is expected to be slightly lower for the isotopes with lower neutron excess (by approximately 2% per excess neutron) since the strength is proportional to the excess (equation (3.52)). It is worth mentioning that cross sections for the IAS excited via the (^{3}He,t) reaction on various Pb-isotopes were measured at E(^{3}He)=60 MeV [170], but with high uncertainties.

Parameters that describe the effective force (see equation (3.35)) are taken from the analysis of the ^{12,13,14}C(^{3}He,t)^{12,13,14}N reactions at 200 MeV [168] (see table 6.6). Only the value for V_τ was deduced by fitting to the measured angular distribution of the IAS. The other parameters are assumed not to change dramatically at the lower beam energy of 177 MeV as compared to 200 MeV [18].

The optical-model parameters that were used in the distorted-wave calculations are listed in table 7.4. They were taken from the literature (217 MeV ^{3}He on ^{208}Pb [56]). For the tritons the well depths were taken 85% of the values for the ^{3}He particles (see section 3.3.2).

The distorted-wave calculations were transformed to the laboratory frame and folded with the angles covered by each of the 11 mrad wide bins. Note that each bin in fact consists of three separate parts, because of the angle-defining slit that was used. The result for fitting the calculated to the measured differential cross sections is shown in figure 7.3. A value of 3.50±0.11 MeV for V_τ was found to results in the best fit. This value is, within the uncertainty, equal to the value found (see previous chapter) at a beam energy of 198.8 MeV (see also chapter 8.1).

DWBA calculations were performed also for other giant resonances. The wavefunctions, constructed in the normal-mode formalism, are given in appendix A, tables A.4 to A.6. The results are similar to those for the ^{124}Sn target. The angular distributions are shown in figure 7.5

In table 7.5, some details of the calculations are given. The cross sections for the monopole transitions will decrease strongly with increasing momentum-transfer and

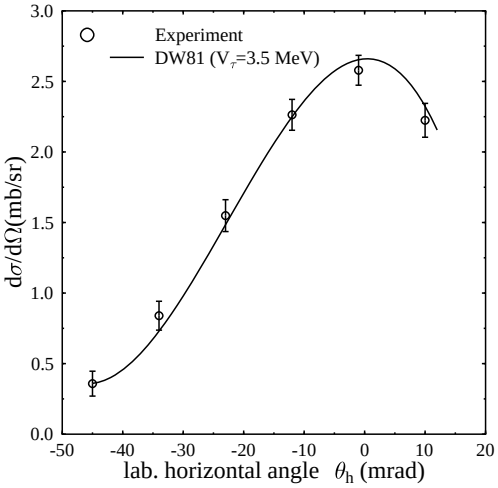

Figure 7.3: Differential cross section of the IAS and fitted calculation.

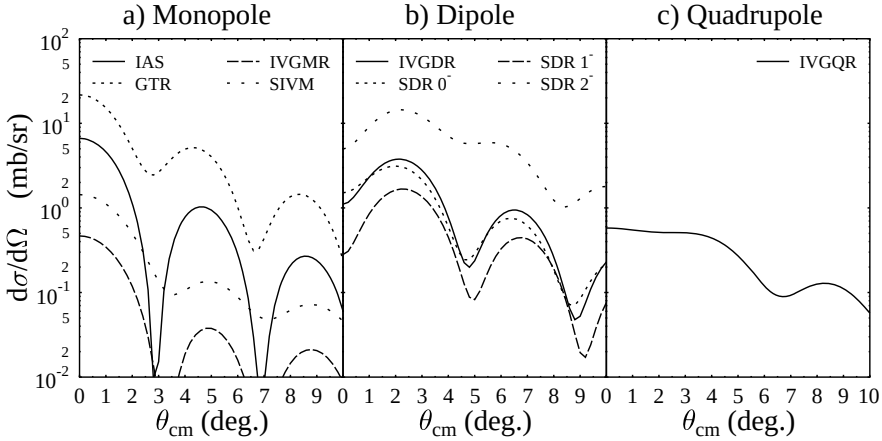

Figure 7.4: DWBA calculations for a) monopole, b) dipole and c) quadrupole resonances excited through ^{208}Pb(^{3}He,t) at E(^{3}He)=177 MeV. The excitation energies used in the calculations for the various resonances are given in table 7.5.

Table 7.5: Excitation energies, momentum transfers at 0° and DWBA cross sections at 0° for the various resonances excited through the ^{208}Pb(^{3}He,t)^{208}Bi reaction at 177 MeV.

Resonance	J^π	E_x [MeV]	q(0°) [1/fm]	$d\sigma/d\Omega(0°)$ [mb/sr]
IAS	0^+	15.171	0.2643	6.65
GTR	1^+	15.6	0.2708	21.7
IVGDR	1^-	22.8	0.3820	1.105
SDR	0^-	24.9	0.4130	0.272
SDR	1^-	22.7	0.3790	1.507
SDR	2^-	19.5	0.3299	4.96
IVGMR	0^+	35.0	0.5742	0.47
SIVM	1^+	35.0	0.5742	1.44
IVGQR	2^+	31.4[a]	0.5151	0.88

[a]Calculated using E_x=130*$A^{-1/3}$ [10] and correction for the fact that predominantly the $(T-1)$ component will be excited.

Table 7.6: Definitions for combinations of cuts and the average scattering angle ($\bar{\theta}_t$) of each gate. See also figure 7.5.

	Definition				$\bar{\theta}_t$ [deg.]
gate I	cut 2	cut 5			1.4
gate II	cut 1	cut 3	cut 4	cut 6	3.2
gate III	cut 1	cut 2	cut 3		1.8
gate IV	cut 4	cut 5	cut 6		1.2
gate V	cut 2				2.0
gate VI	cut 5				0.8

since the excitation energies for the SIVM and IVGMR are not well known, this gives rise to large uncertainties in the cross section. Calculations for the cross sections of the SIVM and IVGMR as a function of $|Q|$-value will be presented in the following section.

In order to investigate angular distributions in the remainder of this chapter,angular gates (cuts) in the solid angle of the BBS were applied (limited by the special angle-defining aperture of figure 5.5(b)). The cuts are explained in figure 7.5. For simplicity, combinations of cuts are made. They will be called 'gates' and are defined in table 7.6. Note that gate I and gate II simply correspond to the divisions made in the solid angle by the special angle-defining aperture and thus can not result in systematic errors due to imperfections in the ray-tracing procedure. Since the angular aperture of the cuts is large compared to the angular resolution (see section 5.2.3), the errors introduced by the software cuts are small. Gates I and II are complementary in the sense that if added together the whole available solid angle is covered. The same holds for gates III and IV. Furthermore, note that the various gates probe different angular ranges. Using gate V, for example, for which the average triton scattering angle is 2°,

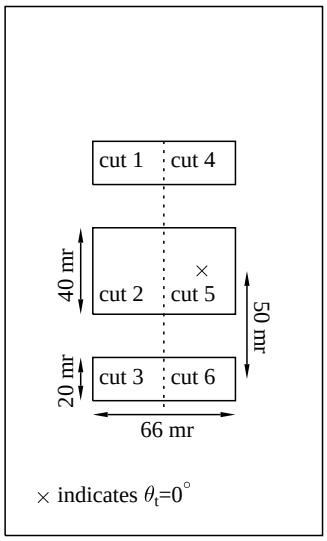

Figure 7.5: The various cuts in the solid angle of the BBS, limited by the special angle-defining aperture.

high sensitivity to contributions from dipole transitions is obtained (see figure 7.4). A comparison between spectra obtained with gate I and II is most useful to study monopole transitions. This is not only because of the absence of systematic errors and the large expected difference in contributions from monopole transitions in spectra obtained with these two gates, but also because contributions to the number of events in both gates due to dipole transitions are almost equal.

It should be realised that the scattering angles present in different gates are sometimes strongly overlapping. This is especially the case for gates III and IV, resulting in a loss of sensitivity for components with different angular distributions.

7.3 Coincidence data

As discussed in the beginning of this chapter, results from investigating the decay of the GTR and SDR resonances in ^{208}Bi by direct proton emission excited through the ^{208}Pb(^{3}He,t) reaction at 450 MeV [37, 38], partly triggered the experiment described here. One has to be careful in comparing results though, since reaction kinematics, and thus available phase space for quasifree and breakup-pickup processes, is dependent on bombarding energy. Because of momentum conservation, protons stemming from quasifree and breakup-pickup mechanisms are more strongly forward peaked if the bombarding energy is higher. Part of this chapter will therefore deal with the

investigation of possible contributions from protons stemming from quasifree processes to the coincidence cross section. The plane-wave impulse approximation (PWIA) will be used. The formalism was treated in section 3.7.

Investigating the decay by proton emission has two main experimental advantages as compared to the study of decay by neutron emission. Firstly, using solid-state detectors, it can be assumed that the detection efficiency for protons is 100%. Whereas for neutrons spectra have to be corrected for energy-dependent efficiencies, for the protons the analysis is more straightforward. Secondly, since statistical decay by proton emission is small, due to the Coulomb barrier, multiplicity corrections are not needed.

Decay by α-particle emission ais, as a consequence of the Coulomb barrier, strongly inhibited and was neglected. ^{3}He-particles due to elastic scattering from the target and deuterons from breakup processes are strongly forward peaked and, moreover, only contribute to random coincidences. Therefore, it is unnecessary to perform particle identification by putting ΔE-detectors in front of the thick Si(Li)-detectors.

Proton detectors were put at polar angles between 96° and 160° with respect to the beam direction and at out-of-plane angles between -20° to 40°. The solid angle covered was 6% of 4π. A 5 mm thick aluminium disc was placed in front of one of the detectors. This was done to slow down the emitted protons and to stop even high-energy (up to 50 MeV) protons inside the detector. As a result low-energy protons (below 30 MeV) could not reach that particular detector. Due to low statistics and possibly interference from reaction products due to scattering of the protons in the aluminium disc itself, coincidences with this detector were impossible to interpret. It was also attempted to measure coincidences at forward angles, with the main purpose to study quasifree and breakup-pickup processes in that part of the phase space, but due to very high count rates the detectors had to be switched off during the experiment.

For the analysis of the coincidence data, the proton detectors were divided into five groups. Each group contains detectors with nearly equal (within 2°) polar scattering angle. These angles were: 96° (3 detectors), 125° (2 detectors), 135° (3 detectors), 140° (3 detectors) and 160° (2 detectors).

In figure 7.6 a three-dimensional coincidence spectrum of proton energy (E_p) versus $|Q|$ is displayed. Random events have already been subtracted following the procedure described in section 5.9. The most distinct peak in the plot corresponds to decay by proton emission from the IAS. For the IAS, protons emitted in a direct way to the ground state of the final nucleus will thus have an energy of approximately 11.5 MeV (see Q-values for proton-emission quoted at the beginning of this chapter). Because of the different Pb isotopes present in the target and the limited energy resolution of 360 keV, decay to different final neutron-hole states cannot be distinguished. Decay to neutron-hole states in ^{207}Pb from the IAS and GTR has been studied extensively in the past [37, 38]. Bordewijk [170] investigated the direct decay from the IAS for the stable Pb isotopes.

In figure 7.7(a), the two-dimensional spectrum is shown, in which the events have been projected on the '$|Q| - E_p$' plane. The darkest diagonal band in figure 7.7(a) corresponds to a combination of decay from the excited nucleus to low-lying hole states, and quasifree and breakup-pickup processes. In this plot the data of these two different processes overlap, since, from a kinematical point of view, the processes are similar. At

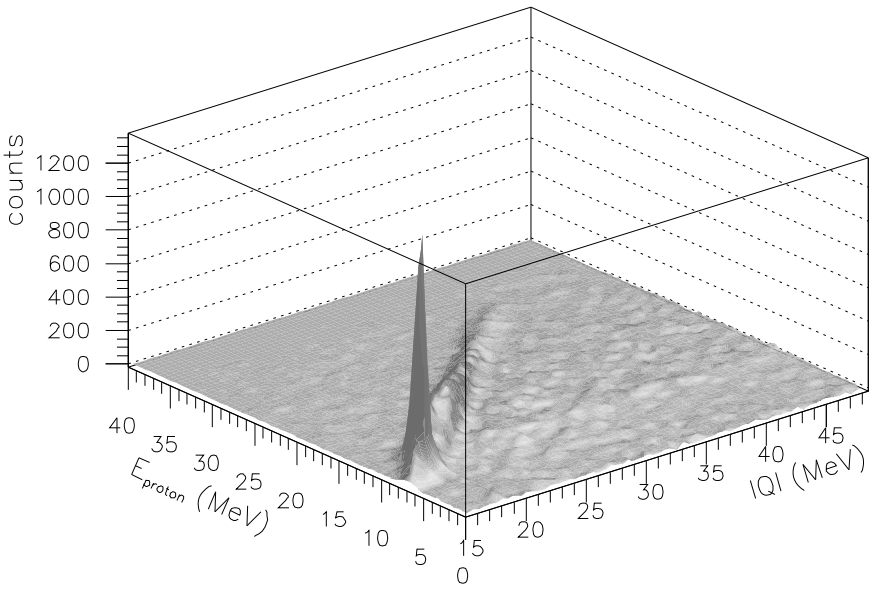

Figure 7.6: Proton energy E_p versus $|Q|$, summed for all proton detectors (see text).

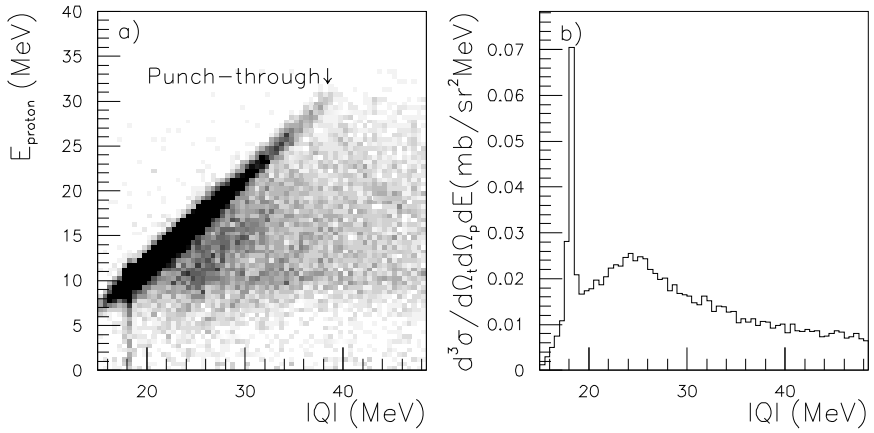

Figure 7.7: Coincidence spectra summed for all proton detectors. Proton-energy versus $|Q|$ (a) and projection on the $|Q|$-axis (b).

$E_p \approx 30$ MeV, protons will punch through the detector (as indicated in figure 7.7(a)), and deposit less energy (see also figure 5.19(a)). Indeed, a weak band can be seen for $|Q|>38$ MeV, corresponding to protons at the kinematical limit of the decay process. It can be shown that this weak band stems for 90% from coincidences with protons in the most forward detectors (θ_p=96°).

Protons emitted in a statistical way are expected to have an energy of approximately 10 MeV (calculated using the code CASCADE [87]). As explained earlier, statistical decay will largely occur through decay by neutron emission. The CASCADE calculations show that statistical decay by proton emission is of the order of 0.1% of the total statistical-decay branch (calculated at E_x=40 MeV). Although coincidences are measured for which the proton has an energy of approximately 10 MeV, it is impossible to determine to what extent these stem from statistical-decay processes.

Figure 7.7(b) is the projection of the two-dimensional plot (figure 7.7(a)) on the $|Q|$-axis and can be compared to the singles spectrum (figure 7.2). It was found that the branching ratio for direct decay by proton emission ($P^{\uparrow}$, associated with the escape width $\Gamma^{\uparrow}$) from the IAS is 69±3%. To obtain this number, the three most forward proton detectors ($\theta_p = 96°$) were excluded from the analysis, since they were partially blocked by the target holder (see also next section). Decay from the IAS in ^{124}Sb, discussed in chapter 6, occurs mainly through statistical emission of neutrons even though decay by neutrons is isospin forbidden and is only possible as a result of isospin mixing. This is due to the relatively high Coulomb barrier in combination with a high angular momentum barrier. In the Pb-isotopes, the combination of barriers is less high and decay by proton emission is dominant. The escape width and corresponding branching ratio have been measured for the IAS in Bi isotopes with A=204, 206 and 207 by Bordewijk [170] who found branching ratios of (73.3±14.0)%, (60.5±4.2)% and (67.7±4.5)% respectively. For the IAS in ^{208}Bi, results have been presented by Gaarde et al. [175] (they find a branching ratio of (63.5±3.0)%) and Akimune et al. [38] (who find (63.4±3.0)%). If these values are combined, with the proper isotopic weighting, a value of (64±4)% for the branching ratio for decay of the IAS, populated by the Pb(^{3}He,t) reaction, by direct proton emission should be expected, which agrees with the present analysis.

7.4 Quasifree processes

It is important to investigate to what extent quasifree processes contribute to the coincidence data. An indication that such processes indeed do play a considerable role can be seen in figure 7.8. The summed coincidence $|Q|$-value spectra for groups of proton detectors with almost identical polar scattering angles are displayed. The number of counts in each spectrum has been divided by the number of detectors contributing to that particular spectrum. All detectors cover the same solid angle except for the most forward proton detectors ($\theta_p = 96°$). They were partially shielded by the target holder, and thus effectively had a smaller opening angle. This was corrected for by scaling the total number of counts for the IAS in these detectors to the mean of the number of counts found for the IAS in the other detectors, since decay products from the IAS are

isotropically distributed (ΔL=0). A factor of approximately 2 was needed to correct for the shielding. It can be seen from the figure that a large fraction of the total coincidences peaks at forward proton angles. A large structure peaking around $|Q|$=25 MeV drops steadily with increasing proton polar angle. In first instance, one would assign this structure to decay by proton emission from the IVGDR/SDR. This can, however, not be the case since the branching ratio for this decay from the IVGMR/SDR should then be much higher than the value reported ((13.4$\pm$3.9)%) for the decay by direct proton emission from the SDR in ^{208}Bi excited through the same reaction at 450 MeV [38, 39]. In fact, if one subtracts the estimate for the quasifree continuum from the complete singles spectrum (figure 7.2) and assumes that the remaining cross section between $|Q|$=22 MeV and 32 MeV stems completely from the the SDR/IVGDR, one finds that the total branching ratio for decay by proton emission in that $|Q|$-value range (assuming an isotropic distribution) is 29%.

Because the behaviour of the structure at $|Q|$=25 MeV is typical for coincidences due to quasifree processes, a model in plane-wave impulse approximation (PWIA) (see section 3.7), which was previously used in the description of the (α,α'n) knock-out process [80, 118], has been used to test the hypothesis.

The procedure was the following. Equations (3.61) to (3.64) were used and most parameters can be put in straightforwardly, especially after realising that relativistic corrections are very small and do not have to be taken into account. The quasifree scattering process can be regarded as the scattering of ^{3}He on a neutron. Since ^{3}He and ^{4}He particles are both strongly absorbed at the surface of the target nucleus the (^{3}He,^{3}He'n) and (α,α'n) reactions are rather similar and we use the formalism used in the latter case [118, 80] also in the present work. The process which is responsible for the charge-exchange of a proton, which is part of the ^{3}He projectile, with a target neutron is neglected. In other words, it assumed that the (^{3}He,tp) process is similar to the (α,α'n) process. The reaction is purely studied from a kinematical point of view.

The momentum distribution of the knocked-out particle, the neutron, is described by the square of a harmonic-oscillator wave function in momentum space. Since it is not known which neutron of the target nucleus is knocked out, in principle one should perform PWIA calculations for processes involving different target-neutrons, normalise these to the spectroscopic factors, and subsequently fit the measured spectrum to a sum of all contributions. The situation is simplified, however, by the fact that the procedure is done in a reverse order; first one calculates the momentum of the neutron in the target nucleus as it should have been by looking at the kinematics of the reaction, and then one calculates the probability of finding a neutron with such momentum. Following the procedure described in section 3.7, one finds that coincidences between protons at backward angles ($\theta_p > 90°$) and tritons at forward angles ($\theta_t < 4°$), in the apparent excitation-energy range between 20 MeV and 50 MeV, are only possible if the momentum of the neutron in the target is in between 250 MeV/c (for $\theta_p = 90°$) and 350 MeV/c (for $\theta_p = 180°$). In figure 7.9(a) the neutron-momentum distributions for three of the highest neutron shells in ^{208}Pb ($2p_{1/2}$, $1f_{5/2}$ and $0i_{13/2}$ shells) are shown. In the figure, the distributions have been scaled with respect to each other in order to make the tails overlap. In the relevant momentum range the dependence of the probability distribution on momentum is similar for the neutrons in the different shells;

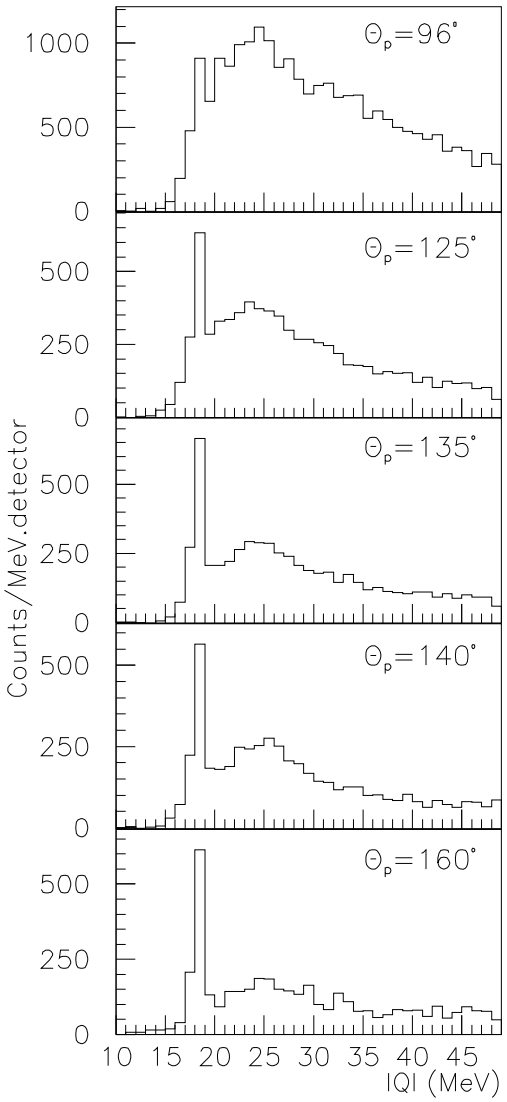

Figure 7.8: Coincidence spectra for groups of proton detectors corresponding to polar angles as indicated in each panel.

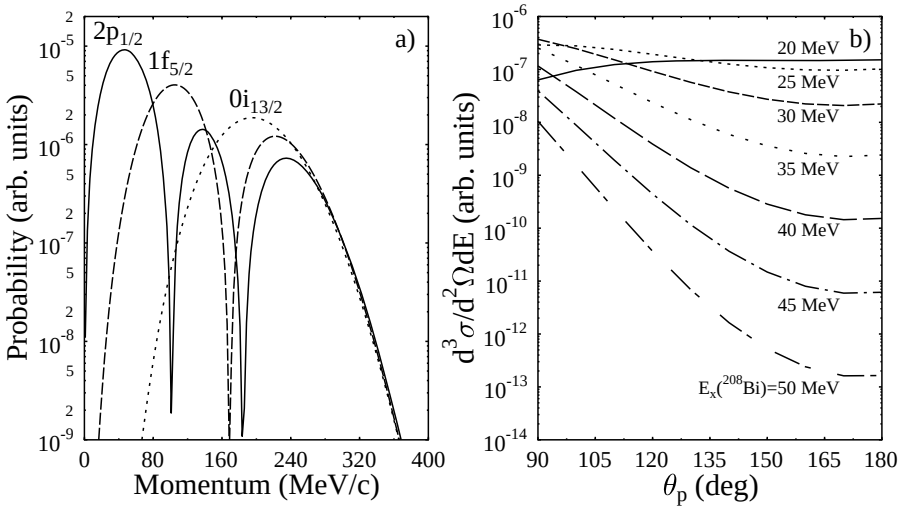

Figure 7.9: Momentum distributions of the $2p_{1/2}$, $1f_{5/2}$ and $0i_{13/2}$ neutrons in ^{208}Pb approximated by the square of a harmonic-oscillator wave function in momentum space (a). The curves are scaled with respect to each other in such a way that the tails overlap. Coincidence cross-section curves (b) as a function of θ_p for $\theta_t = -1^\circ$ and for different apparent excitation energies of the target nucleus.

they fall off more or less exponentially. Since we are not interested in the absolute cross sections, we can just use any of the curves. If one would like to perform calculations for quasifree contributions at more forward proton angles, the situation would be more complex since the missing momentum of the neutron involved in the process could be much smaller in that case, and the probability would be strongly dependent on the quantum numbers of the corresponding neutron shell.

By using equation (3.61), coincidence cross sections for the quasifree processes are calculated as a function of the triton scattering angle (θ_t), the proton polar angle (θ_p) and the apparent excitation energy of the target nucleus. It is assumed that the triton angular distribution is flat near 0°. In figure 7.9(b) results are shown for quasifree processes in ^{208}Pb for the case where the triton passes through the centre of the solid angle of the BBS during the experiment described here ($\theta_t = -1^\circ$). For the most backward proton angles and for high excitation energies, the cross section drops by several orders of magnitude with respect to the cross section at $\theta_p = 90^\circ$.

It must be noted that the rate for protons emitted in the quasifree process is axially symmetric around the recoil axis of the excited nucleus. The effect of a change in recoil angle with changing triton-scattering angle is a shift of the curves that are displayed in figure 7.9(b). The magnitude of the shift is also dependent on the apparent excitation energy. This effect was taken into account by subdividing the opening angle into smaller angular bins and by calculating the cross-section curves per bin, using the central triton scattering angle of each bin. Finally, all contributions were added and by combining

values at different apparent excitation energies for a particular proton polar angle, $|Q|$-value spectra corresponding to quasifree processes were constructed. The main effect of the shifting recoil axis is that for a specific proton polar angle the cross section will not drop as strongly as a function of $|Q|$ as was the case in figure 7.9(b).

No distinction between detectors at equal polar scattering angle but different azimuthal angle has been made. In principle this is not correct, but due to the folding over triton scattering angles present in the solid angle of the BBS, differences in the azimuthal coordinate are averaged out. It was indeed found that, $|Q|$-value spectra from proton detectors at different azimuthal angles, but similar polar angles were are very similar. Therefore, to increase statistics, data from such detectors were added.

In order to compare with the data, the measured spectra for each group of proton detectors, corresponding to approximately the same proton polar angle, were gated on coincidences that correspond to direct decay by proton emission to states in the final nucleus below 5 MeV.
Assuming ^{208}Pb to be the target nucleus, this corresponds to:

$$E_x(^{207}\mathrm{Pb}) = (E_x(^{208}\mathrm{Bi}) - S_p - E_p) < 5 \text{ MeV} \tag{7.1}$$

in which S_p is the proton-separation energy and E_p is the measured proton energy. Because of the 'punch-through' effect only data up to $|Q|$=38 MeV were taken into account.

The contribution from quasifree processes to coincidences for which θ_p=160° is very small. To remove contributions that are certainly not due to quasifree processes, the coincidence Q-value spectrum for θ_p=160° was subtracted from the coincidence spectra at the other proton angles. The same subtraction was performed for the calculated spectra. By doing so, contributions from, for example, the IAS in the experimental spectra are excluded in the comparison. It must be realized, however, that this method does not fully exclude contributions from the IVGDR and SDR, since decay from these resonances is not isotropic.

The results are shown in figure 7.10. One common scaling factor is introduced for all calculated curves. Taking the assumptions of the model into account, the calculated curves correspond well with the data.

Together with the fact that the expected contribution to the coincidence $|Q|$-value spectrum due to the IVGDR and SDR is much smaller, because of the smaller branching ratios [38, 39], than for the structures found in the present data around $|Q|\approx$25 MeV, it is quite plausible that a fraction of the coincidence spectrum stems from quasifree processes. This is especially true for the most forward detectors and for $|Q|<$30 MeV. Even for very backward proton angles the results suggest interference from these processes below $|Q|$=30 MeV. It would, however, only be possible to draw strong conclusions if data is also taken for $\theta_p < 90°$, where the quasifree contributions are believed to be dominant.

It must also be noted that even for higher $|Q|$-values the spectrum at $\theta_p = 96°$ (top panel of figure 7.8) contains considerably more (a factor of ~ 3) events than at other angles. It was already noted that the punch-through band in figure 7.7(a) almost completely stems from coincidences with these forward-positioned detectors. Also, more complex processes that contribute to the continuum background and that result

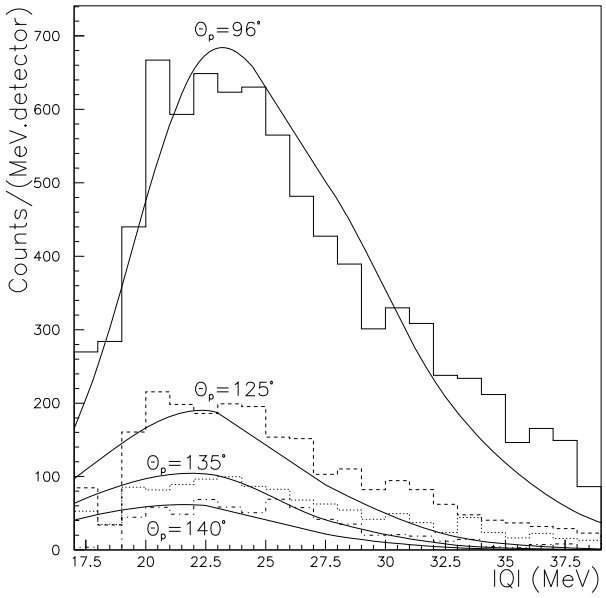

Figure 7.10: Comparison of cross-section calculations for quasifree processes (solid lines) and data (histograms). The calculational procedure is explained in the text.

in coincidences between tritons at forward angles and protons at backward angles (e.g. breakup-pickup) could be the cause. In the further analysis, coincidences with the most forward-positioned proton detectors, i.e. at $\theta_p = 96°$, have therefore been excluded. For events that correspond to coincidences with protons at backward proton angles and $|Q|$>30 MeV, the contribution from quasifree and possibly other processes that are part of the continuum background is not completely absent, but reduced strongly and this Q-value range is exactly the region of interest for the SIVM and IVGMR.

7.5 Monopole strength

In order to investigate whether monopole strength is present at high $|Q|$-values, spectra at different triton scattering angles, generated by using the gates as defined in table 7.6 have been compared.

It was explained in section 5.2.3 that reliable difference spectra from events corresponding to separate holes in the aperture-defining slit (gates I and II) can only be made for $|Q|$>27 MeV due to the cross over of the bow-tie. Cuts in the phase space using only the horizontal component of the triton scattering angle (gates III and IV) can be made, however, to investigate the presence of various multipolarities at lower

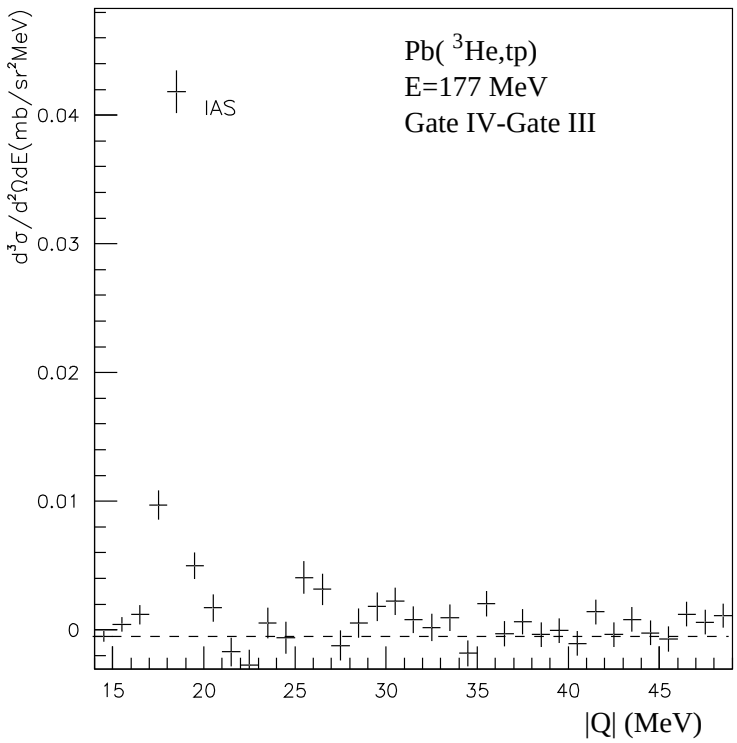

Figure 7.11: Difference between coincidence $|Q|$-value spectra at $\theta_t = 1.2°$ (gate IV) and $\theta_t = 1.8°$ (gate III). Coincidences between tritons and protons detected in the Si(Li) detectors at $\theta_p = 96°$ are excluded.

$|Q|$. A difference spectrum generated by subtracting events in gate III from those in gate IV is shown in figure 7.11.

The IAS, at $|Q|$=18 MeV is the most prevailing feature of this difference spectrum. For the remainder of the spectrum, error bars do not allow strong conclusions on the presence of other resonances. The main reason is that the scattering angles present in gates III and IV overlap to a great extent. It is, therefore, impossible to draw any conclusions on the branching ratio for decay by direct proton emission of the IVGDR and SDR; this is further complicated, because in the relevant range ($|Q|$=22 MeV to 30 MeV), contributions to the coincidence cross section from quasifree processes interfere. The decay from these resonances, and also the GTR, should, therefore, be studied at higher bombarding energies, as was done at E(^{3}He)=450 MeV by Akimune et al. [38] and Harakeh et al. [37], where, because of kinematical considerations, coincidences between tritons at forward angles and protons at backward angles due to quasifree processes are not possible.

The total excess in cross section in the difference spectrum, in the range relevant for the SIVM and IVGMR (30 $<|Q|<$ 48 MeV), was summed for comparison with results

Table 7.7: Difference in coincidence cross section between gates I and II (second column), corresponding to the central hole and a combination of the upper and lower holes in the angle-defining aperture, respectively. Assuming the proton distribution to be isotropic (see text), one finds for a proton-detection solid angle of 4π, the values in the third column for the coincidence cross section.

Q [MeV]	Experiment $\frac{d^2\sigma}{d\Omega_p d\Omega_t}$ [μb/sr^2]	Isotropic p-distribution $\frac{d\sigma}{d\Omega_t}[= 4\pi\frac{d^2\sigma}{d\Omega_p d\Omega_t}]$ [μb/sr]
27-30	-2.31±1.30	-29.0±16.3
30-33	5.45±1.23	68.5±15.5
33-36	6.10±1.08	76.6±13.6
36-39	3.78±0.88	47.6±11.1
39-42	5.75±0.89	72.3±11.2
42-45	0.62±0.85	7.9±10.7
45-48	2.30±1.65	29.0±20.9
>30	24.0±2.8	301±35

from difference spectra created using other gates. For 30 <$|Q|$< 48 MeV, an excess of (6.4±4.0) μb/sr^2 was found. It must be noted that a fit to a zero content for the difference spectrum in figure 7.11 between $|Q|$=30 MeV and $|Q|$=48 MeV results in a reduced χ^2 of 1.4 and is thus within a 95% confidence interval consistent with zero data.

Next, the $|Q|$-value spectra obtained from gates I (central hole of the angle-defining aperture) and II (upper and lower holes of the angle-defining aperture) were compared. The result is displayed in figure 7.12. In figure 7.12(a), the spectra from both gates are shown, and figure 7.12(b) is the difference between the two. A binning of 3 MeV has been chosen. The data in the highest $|Q|$-value bin (45-48 MeV) have slightly larger error bars than the other values. This is due to the fact that only events, which had a vertical triton scattering angle that was larger than zero (i.e. above the median plane), were included in the analysis, because a small fraction of the solid angle below the median was cut due to a missing strip in the detector (see section 5.2.3). It is clear that there is an excess in cross section using gate I with respect to that for gate II between $|Q|$=30 MeV and $|Q|$=48 MeV. Contributions to the cross section in the two gates due to quadrupole resonances are more or less equal, as a consequence of the flat angular distribution (see figure 7.4(c)). The same holds for the contributions due to quasifree contributions. Also, dipole transitions will hardly contribute to the difference spectrum, since calculated cross sections due to these are nearly equal for gate I and gate II. Therefore, in first instance, the excess in cross section can be assigned completely to monopole transitions and interference from other multipolarities can be neglected. In the next section, the influence of the possible presence of other resonances will be estimated.

The data shown in figure 7.12(b) are tabulated in the first column of table 7.7. The total excess in cross section above $|Q|$=30 MeV is 24.0±2.8 μb/sr^2. The second column

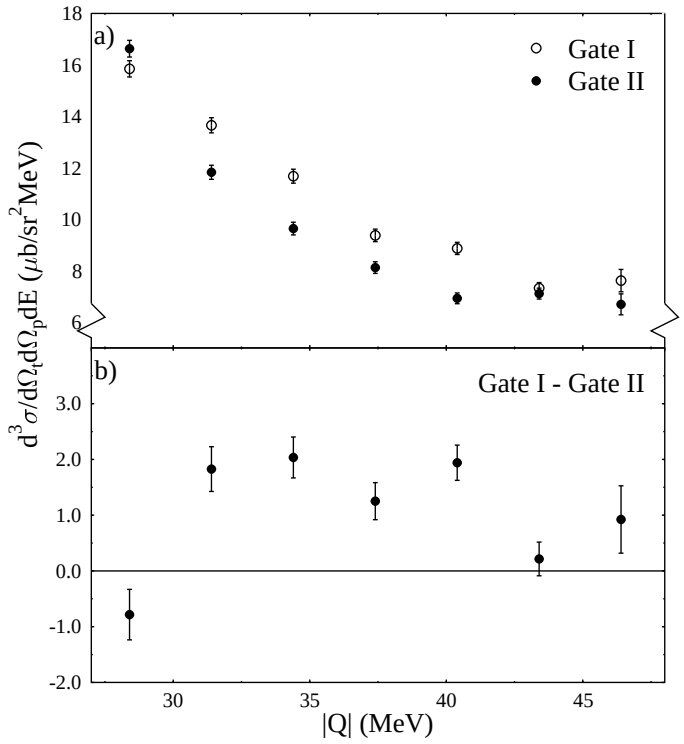

Figure 7.12: (a) Comparison between $|Q|$-value spectra for tritons passing through the top and bottom openings in the angle-defining aperture (gate II, $\bar{\theta}_t = 3.2°$) and tritons passing through the central opening (gate I, $\bar{\theta}_t = 1.4°$); (b) the difference spectrum between the two spectra gated on gate I and II. Coincidences with the most forward proton detectors (at $\theta_p = 96°$) were excluded and a binning of 3 MeV was applied.

in table 7.7 contains the same data, but it is assumed that the coincidence cross section is isotropically distributed (as it should be for monopole transitions) over all proton angles. To check whether this is justified, contributions to the excess in the difference spectrum given in figure 7.12(b) from different proton detectors were compared. The results are shown in figure 7.13.

In figure 7.13(a), data from detectors set at nearly equal proton polar angle (θ_p, see section 7.3) are grouped together. In figure 7.13(b), the same has been done for detectors with equal out-of-plane (azimuthal) angle (ϕ_p). The dotted line is the average excess in counts per detector. A fit of the excess number of counts in each detector to this mean results in a reduced χ^2 of 1.15. Although the error bars are not small, the assumption that the distribution is isotropic, and thus that the excess in cross section in gate I with respect to gate II is of monopole character, is justified.

Next, the experimentally-deduced monopole cross section is compared to the expectations for the SIVM and IVGMR, as discussed in section 7.2. To do so, it is

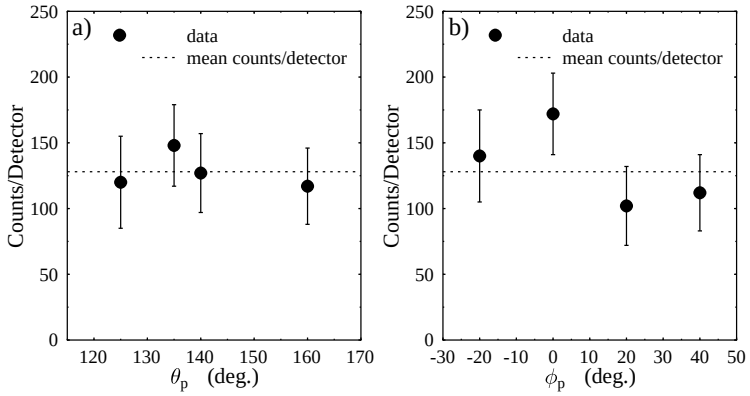

Figure 7.13: Contributions to the excess in counts in gate I (central hole of angle-defining aperture) with respect to gate II (upper and lower holes of angle-defining aperture) from proton detectors at different angles. In (a) the proton detectors are grouped according to polar angle (θ_p) and in (b) according to out-of-plane angle (ϕ_p). The dotted line is the average number of excess of counts per detector.

important to realise that the cross sections of these resonances are strongly dependent on the momentum transfer and thus on the reaction Q-value. The dependence is shown in figure 7.14. The cross sections for the SIVM and IVGMR (at $\theta_t = 0°$) are displayed as a function of $|Q|$. Calculations have been performed with the code DW81, using the wave functions constructed in the normal-mode framework (100% of the NEWSR). The ratio between the cross sections of the SIVM and IVGMR at θ_t=0° is approximately 3.3 over the whole $|Q|$-value range.

Secondly, one has to take into account that the ratio between the expected cross sections at 0° and 3° (the maximum and the minimum, respectively, in the angular distributions of the IVGMR and SIVM) is higher for the IVGMR than for the SIVM (see figure 7.4(a)). This results in a relative enhancement of the contribution from the IVGMR with respect to the contribution from the SIVM to the difference spectrum between gates I and II. The effect is somewhat suppressed due to the fact that the gates cover a range of scattering angles. By folding the calculated angular distributions of the IVGMR and the SIVM over the angles covered by gates I and II, one finds that in the difference spectrum between these two gates, the ratio of the expected cross sections from contributions of the SIVM and IVGMR is approximately 3.

The measured excess in cross section in gate I with respect to gate II can now be compared directly to the excess obtained by folding the angular distributions calculated in DW81 over the scattering angles covered by gates I and II, taking into account the effects discussed above. The ratio of the measured and calculated cross sections gives the percentage of exhaustion of the NEWSR, calculated in the normal-modes framework. Results of the calculations per $|Q|$-value interval of 3 MeV are given in table 7.8. Note that, in the data, no distinction can be made between contributions

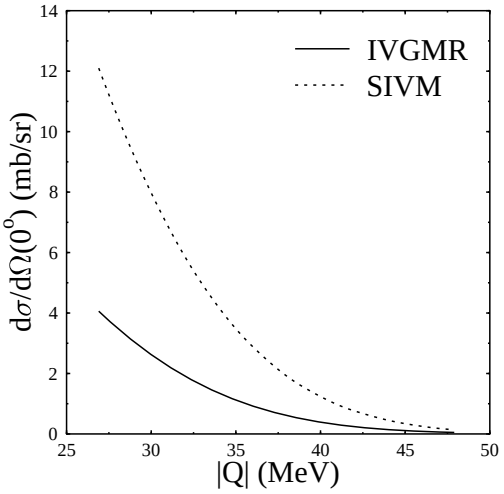

Figure 7.14: Dependence of cross section for the SIVM and IVGMR at θ_t=0° on $|Q|$.

to the excess in cross section from the IVGMR and SIVM. Therefore, the degree of exhaustion of the NEWSR is equal for the SIVM and IVGMR.

Approximately 20% of the NEWSR for the SIVM and IVGMR is found between $|Q|$=30 and $|Q|$=45 MeV in the proton channel. The percentage found in the range between 45 MeV and 48 MeV carries a large error margin, because of the small calculated cross sections and the relatively large experimental uncertainty. It is therefore excluded from figure 7.15, in which the exhaustion of the NEWSR per $|Q|$-value bin of 3 MeV is displayed. The curve drawn in figure 7.15 is the result of a fit with a Lorentzian to the data; the reduced χ^2 of the fit is 3. The width (Γ) is approximately 11 MeV.

It can, therefore, be concluded that if the branching ratio for decay by proton emission from the SIVM and IVGMR is 20%, all normal-mode strength can be accounted for. If a quenching of the strength is taken into account, as predicted by the HF-RPA calculations (see table 7.2), the branching ratio should approximately be a factor of two higher to account for all the strength. The latter statement is, of course, only true if a linear correlation between strength and cross section is assumed.

It was very difficult to attribute the excess in cross section at forward scattering angles to a specific proton decay channel; the experimentally deduced monopole cross section contains contributions from direct, semi-direct and statistical decay (although, as explained earlier, the latter is expected to be extremely small). It was attempted to construct a two-dimensional difference spectrum between events belonging to gate I and gate II, in which proton energy was plotted versus $|Q|$ (similar to figure 7.6(a)), but due to low statistics, conclusions could not be drawn. However, it was possible to determine an upper limit for the branching ratio for direct decay by proton emission

Table 7.8: Comparison of measured and calculated excess in cross section in gate I (central hole of angle-defining aperture) and gate II (upper and lower holes of angle-defining slit), expressed in terms of exhaustion of NEWSR. No distinction between IVGMR and SIVM can be made in the data and the degree of exhaustion of the NEWSR is equal for both resonances.

	experiment	theory		comparison
Q (MeV)	$\frac{d\sigma}{d\Omega_t}$ [μb/sr]	$\frac{d\sigma}{d\Omega_t}$ [μb/sr]		%NEWSR
	monopole	IVGMR	SIVM	
30-33	68.5±15.5	1050	3200	1.6±0.4
33-36	76.6±13.6	650	1950	3.0±0.5
36-39	47.6±11.1	340	1060	3.5±0.8
39-42	72.3±11.2	175	550	10.0±1.5
42-45	7.9±10.7	84	271	2.2±3.1
45-48	29.0±20.9	35	111	20±15
Total	301±35			40±15
< 45	272±28			20±4

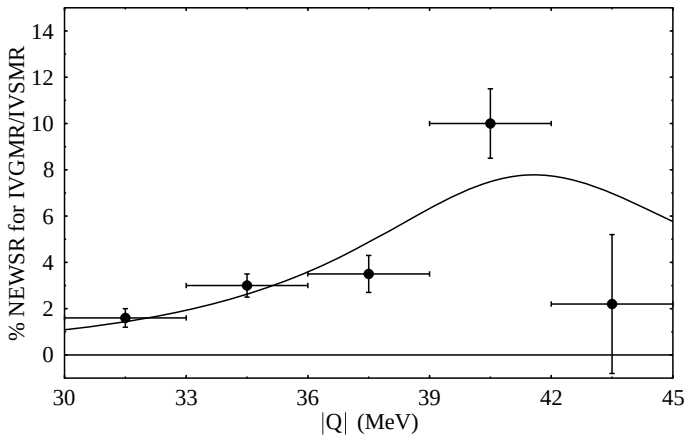

Figure 7.15: Exhaustion of the NEWSR for the IVGMR and SIVM in the proton decay channel. The curve is the result of a fit with a Lorentzian (width $\Gamma = 11$ MeV) to the data points.

of the SIVM and IVGMR. The excess in cross section in gate I with respect to gate II, above $|Q|$=30 MeV, for events that could correspond to direct decay to a state in the final nucleus with an excitation energy below 5 MeV was determined. The events found in this manner cannot be attributed unambiguously to the direct decay processes, because the high-energy protons punch through the detector and deposit the same amount of energy as some protons of lower energy that are stopped in the detector (see figure 5.19(a)). Therefore, only an upper limit can be determined. It was found that at most (41±19)% of the total excess in cross section in gate I with respect to gate II (which corresponds to (8±4)% of the NEWSR for the IVGMR and SIVM) can be attributed to the direct decay process to states in the final nucleus below 5 MeV excitation energy. For the remaining fraction of the experimentally found excess in cross section at forward triton angles, the decay mechanism cannot be deduced from the present data. However, since statistical decay by proton emission is expected to be very small, the remaining events can hardly be attributed to that channel. The results thus suggest that a large fraction of the coincidences attributed to monopole strength, stems from semi-direct decay mechanisms. This outcome can only be studied in full when better statistics are available and high-energy protons, that in the present setup punched through the detectors and deposited less energy, are well separated from lower-energy protons. It must be remarked that the percentage of exhaustion ((8±4)%) is much lower than the only available theoretical calculation of the escape width [79] (see introduction of this chapter).

7.6 Contributions from other resonances

In the above analysis, possible contributions from other resonances has been neglected. In this section, it will be discussed how large the systematic errors due to this may be. In the first part, the possibility of interference from dipole strength at high $|Q|$-values will be discussed. In the second part, it is estimated to what extent the monopole cross section that has been found, could be due to Gamow-Teller strength that has shifted to high $|Q|$ (see section 3.6).

7.6.1 Contributions from dipole transitions

To check whether the monopole cross section, that was found in the difference spectrum between gate I and gate II, is partly reduced due to a dipole contribution (high-energy tails of IVGDR and SDR), difference spectra between $|Q|$-values of 30 MeV and 48 MeV, constructed using the various gates defined in table 7.6, were compared. Three difference spectra were generated: the first one by subtracting spectra belonging to gates I and II (figure 7.12(b)), the second one by subtracting spectra belonging to gates IV and III (figure 7.11), and the third one by using gates V and VI (not displayed). Poor statistics and the limited angular range did not allow a multipole decomposition as a function of Q-value and therefore only the total excesses of the difference spectra between $|Q|$=30 MeV and $|Q|$=48 MeV were fitted. The excess in cross section found by using gates I and II and gates IV and III was (24.0±2.8)μb/sr^2 and (6.4±4.0)μb/sr^2,

respectively (see above). The excess in cross section in gate VI with respect to gate V was (10.0±3.0)μb/sr^2.

Two hypotheses were tested; one in which only a contribution from monopole excitations was assumed between $|Q|$=30 MeV and $|Q|$=48 MeV, and a second in which a combination of monopole and dipole contributions was assumed. Calculations were performed in a similar way as described in the previous section (i.e. by using a folding procedure of the calculated angular distributions in DW81 over the relevant scattering angles covered by the gates and taking into account the dependence of cross section on $|Q|$). The result for the first hypothesis was a χ^2 of 5.83 (with two degrees of freedom). For the second hypothesis the χ^2 reached a minimum of 1.25 (one degree of freedom) if the cross section due to dipole transitions between $|Q|$=30 MeV and $|Q|$=48 MeV is 5 μb/sr^2.

The possibility of contributions to the cross section from dipole excitations above $|Q|$=30 MeV can not be excluded. Such a contribution, with a magnitude of 5 μb/sr^2, would result in a quenching of approximately 20% of the cross section (24.0±2.8)μb/sr^2) found for monopole transitions in the difference spectrum between gates I and II, i.e. the cross section of the SIVM and IVGMR should be increased by 20% if dipole strength is assumed to be present.

7.6.2 Gamow-Teller contributions

To investigate to what extent the monopole cross section that was unravelled could be due to Gamow-Teller strength that has shifted up to high $|Q|$, it was assumed that all the 'missing' GTR strength at low Q-values (40% of 3(N-Z), see section 3.6) was shifted towards the Q-value range between 30 MeV and 48 MeV. In practice, distorted wave calculations for the GTR were performed assuming 100% exhaustion of the NEWSR in the normal-mode formalism and the calculated cross section was then multiplied by 0.4. The calculated angular distributions were folded over the scattering angles covered by gates I and II and subtracted from each other (note that the angular distributions of GTR, SIVM and IVGMR are rather similar and thus comparing difference spectra obtained through subtracting data from other gates than I and II does not make sense). Of course, Q-value dependence was taken into account. The calculated difference in cross section between gates I and II due to the GTR was compared to the experimental results obtained for the SIVM and IVGMR. The result of the comparison was that maximally 15% of the excess in cross section in gate I with respect to gate II could be due to high-lying GTR strength.

The possible interference of spin-dipole and GTR contributions has been disregarded in the calculations presented in section 7.5.

7.7 Conclusions

It can be concluded that evidence for monopole strength has been found in the Pb(^{3}He,tp) reaction at $|Q|$-values between 30 and 48 MeV in the coincidence spectrum between tritons at forward scattering angle and protons at backward angles. This strength can be assigned to the SIVM and IVGMR. It has been shown that in this part of the

phase space contributions from quasifree processes are strongly suppressed. The total double-differential coincidence cross section found was 24.0±2.8 μb/sr^2 (301±35 μb/sr if integrated over the full proton detection solid angle). Approximately 20% of the NEWSR for the IVGMR and SIVM, calculated in a normal-modes framework, was found in the proton decay channel.

Possible underestimation of the cross section of the IVGMR and SIVM due to interference from dipole contributions by 20% and a possible overestimation of the cross section by 15% due to the presence of Gamow-Teller strength can not be excluded.

Low statistics make determination of branching ratios for the various decay channels impossible. However, an upper limit of (8±4)% for the exhaustion of the NEWSR for the IVGMR and SIVM by the direct proton-decay channel could be extracted.

8. Conclusions and outlook

The goal of the experiments performed as part of this thesis was to find isovector monopole strength at high excitation energies associated with the IVGMR and SIVM. This was done by studying coincidences between ejectiles at forward angles and decay particles (protons or neutrons) emitted from the excited nucleus at backward angles.

It has been shown by performing distorted-wave calculations using wave functions constructed in a normal-modes formalism that the largest contribution to the cross section associated with the isovector monopole transitions, excited through the (^{3}He,t) reaction at approximately 190 MeV, is expected to stem from the transition where spin-flip is involved. Since the $V_{\sigma\tau}$ and V_{τ} components of the effective nucleon-nucleon interaction are of approximately equal magnitude at this beam energy, the dominance of the SIVM over the IVGMR in terms of strength is almost linearly translated in the expected cross sections. A further, although smaller, effect is due to the influence of the $V_{T\tau}$ component of the effective nucleon-nucleon interaction, since it only contributes in the excitation of the SIVM and not of the IVGMR.

Calculations performed in a HF-RPA framework by Auerbach and Klein show a strong reduction (∼50%) of the transition strength for the resonances under study with respect to calculations performed in the normal-mode framework. The reason for this difference is the fact that in the HF-RPA calculations, ground-state correlations are taken into account, in contrast to the calculations performed in the normal-mode formalism.

In the first experiment, the ^{124}Sn(^{3}He,t)^{124}Sb* reaction at 200 MeV and the subsequent decay by neutron emission were measured. No cross section was found at high excitation energies that could be associated with monopole transitions. With a certainty of 95%, the cross section for the isovector giant monopole resonances is below 20% of the expected cross section, assuming full exhaustion of the NEWSR calculated in the normal-modes formalism and a Lorentzian line shape with a width of 10 MeV).

The main reason was that a large fraction (∼50%) of the non-resonant continuum background also consists of processes that lead to neutron emission at backward angles. This indicates that either deep-lying neutrons are involved in those processes and the thus-excited nucleus can decay statistically by neutron-emission in spite of the rather high separation energy, or that more complex mechanisms play a more important role than expected.

It must also be mentioned that if indeed the quenching of the SIVM and IVGMR is as strong as predicted in the HF-RPA calculations and moreover their widths are extremely large (>20 MeV) the presence of monopole strength cannot be excluded completely given the statistical uncertainties obtained in the present experiment.

Corrections that have to be performed for neutron-emission multiplicity and neutron-detection efficiency could give rise to sizeable systematic errors. On the other hand, this

can not explain the failure in revealing monopole strength since the correction procedure will not bias data at various scattering angles differently. Furthermore, results for the statistical decay by neutron emission from the IAS agree well with predictions and previous experimental data, indicating that systematic errors are not extremely large. Unfortunately, due to problems in the ray-tracing procedure in the vertical direction, part of the sensitivity to the monopole angular distribution was lost.

A second experiment focusing on coincidences between tritons and decay protons was performed. The ^{3}He-beam energy was 177 MeV and the target was Pb. In this case strength corresponding to monopole excitations at high excitation energies was unravelled in the exclusive spectra. Although coincidences due to quasifree processes still contribute at $|Q|$-values below 30 MeV, it has been shown by studying the kinematics of such processes that for $|Q|$>30 MeV and at proton polar angles larger than 120° the contributions from these processes are strongly reduced. It was therefore possible to identify the monopole contribution at high excitation energies. Determination of ray-trace parameters for the reconstruction of events was successful, also in the vertical direction. Still it was decided to place a special angle-defining aperture in front of the entrance of the spectrometer in order to remove uncertainties due to limited angular resolution.

The monopole cross section found in the proton-decay channel corresponds to 20±4% of the NEWSR for the SIVM and IVGMR, calculated in the normal-mode formalism. Assuming a (more realistic) branching ratio of 20% would, therefore, mean that all strength can be accounted for. On the other hand, if one considers the reduction in transition strength as calculated in HF-RPA, compared to the calculations in the normal-mode framework, a higher total branching ratio for proton decay can be expected. Also additional strength could be present at $Q > 45$ MeV. Due to low statistics and the fact that the highest-energy protons (which stem from the direct decay process) punch through the Si(Li) detectors and deposit less energy, it was not possible to determine branching ratios for the direct, semi-direct and statistical decay channels. An upper limit for the cross section in the direct-decay channel (to states in the final nucleus below an excitation energy of 5 MeV) could however be estimated. The result corresponds to 8±4% of the NEWSR. Since statistical decay by proton emission is negligible, the results suggest a considerable semi-direct decay channel.

8.1 The V_τ component of the effective potential.

In both experiments that were performed, the V_τ component of the effective nucleon-nucleon (NN) potential was determined by fitting the distorted-wave calculations for the IAS to the experimentally found differential cross sections. The V_τ parameter was the only free parameter. The values found can be compared to values determined at other beam energies and systematics as predicted by theory. This is done in figure 8.1. All data stem from (^{3}He,t) experiments, performed on various targets. It is clear that the isospin-flip component of the effective potential drops strongly as a function of beam energy. The theoretical curve is a smooth interpolation of curves calculated by Bertsch et al. [176] (up to 300 MeV) and by Love and Franey [18] (higher energies).

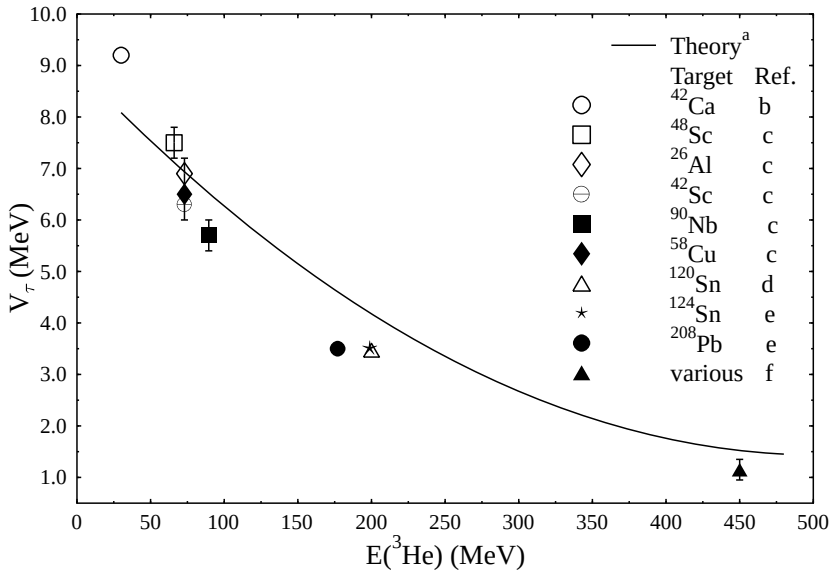

Figure 8.1: Dependence of V_τ on ^{3}He beam energy. The curve (a) is taken from Bertsch et al. [176] and Love and Franey [18]. The data are from: (b) Schaeffer [59], (c) Van der Werf et al. [57], (d) Jänecke et al. [114], (e) this work and (f) Fujiwara et al. [177].

Bertsch et al. [176] derived the effective NN interaction from the basic NN force via the intermediary of a representative set of G-matrix elements. Love and Franey [18] derived the curve above a bombarding energy of 300 MeV (100 MeV for protons) from the free NN t matrix.

These predictions were originally developed for (p,p) and (p,n) reactions. Therefore, to compare the calculations with the results obtained from (^{3}He,t) reactions, one should perform a folding of the interaction over the ^{3}He particle. This has not been done here. Based on the idea that, since the ^{3}He particle consists out of three nucleons, the derived values of the parameter V_τ from the (^{3}He,t) experiments can be expected to be an addition of those deduced from the (p,n) reaction. Due to the isospin-flip part of the effective potential, however, contributions due to the neutron and one of the protons of the ^{3}He particle cancel. Therefore, the value for V_τ in the (^{3}He,t) reaction is expected to be approximately equal to that from a (p,n) reaction. Of course, one should compare data from the (p,n) reaction at a certain bombarding energy with (^{3}He,t) data at the same bombarding energy per nucleon.

As can be seen from figure 8.1, the values of V_τ obtained from the (^{3}He,t) data agree reasonably well with the predictions by Bertsch et al. [176] and Love and Franey [18], in spite of the fact that the folding of the interaction over the ^{3}He particle was omitted. It must be mentioned that error bars of the experimentally deduced values for V_τ are statistical only; other, systematic errors could arise from inaccuracies due

to the optical potentials used and deviations due to the limited accuracy of measuring the integrated beam current in the Faraday cup.

8.2 Outlook

The results, especially from the (^{3}He,tp) experiment, justify further investigation using the same method. There are three main issues that need to be addressed.

First of all, one should strive to establish a more complete picture of isovector monopole resonances by studying various nuclei. This is troublesome, because in order to have good statistics one would need a considerable amount of beam time.

Secondly, one should try to distinguish between the IVGMR and SIVM. For the (^{3}He,t) reaction this can only be done by going to a higher beam energy. As shown in the above picture, at 450 MeV the expected contribution from the non-spin-flip component is very low. Therefore, at beam energies around this value, one would observe almost solely the contribution from the SIVM. At these energies one has the further advantage that momentum transfer will be lower and thus cross sections higher. Also, protons stemming from the quasifree processes will be more strongly forward peaked than at lower beam energies. Going to very low beam energies in order to be especially sensitive to the IVGMR is difficult since the momentum transfer will become large and thus the cross section very low. Therefore, for the direct study of the IVGMR, spinless light particles, such as pions, are the best probes.

Finally, one should try to study the various decay channels in order to determine branching ratios and decay widths. For this one should accurately measure the energy of the decay particles. For neutrons, one should measure time-of-flight. This has the disadvantage that the solid angle that is covered will become smaller because the detectors have to be put at some distance from the target. In the case of protons it should be considered to use detectors in a telescope setup (ΔE-E measurement) in order to remove the ambiguity caused by the punch-through effect of the high-energy protons. If such an extensive study of the decay properties were to be undertaken, considerable theoretical effort is needed, since accurate calculations of decay widths and branching ratios for the IVGMR and SIVM are scarce.

There are many different probes that one can use to excite the IVGMR and SIVM. They have been mentioned in chapter 4 of this thesis. Each of the probes has its advantages and disadvantages. Study of the SIVM or IVGMR by using the (p,n) or (n,p) reactions (especially at lower bombarding energies) has the disadvantage that the entire nuclear volume is probed, leading to a cancellation of transition strength. Moreover, from an experimental point of view these reactions are difficult to study. Especially for the (p,n) reaction the momentum mismatch is very large, leading to reduced expected cross sections for the monopole resonances relative to the underlying continuum and other resonances.

Further investigation using the π-charge-exchange reactions is difficult, since the resolution is low which makes study of the decay mechanisms difficult.

Heavy-ion reactions have been used in the past for the study of the IVGMR and SIVM. The general disadvantage of using such probes is the contribution from more

complex channels as compared to the relatively simple ^{3}He probe. Also, the analysis is more involved, since one has to be sure that one carefully identifies particles with nearly equal mass-to-charge ratio detected in the spectrometer.

The recently published results from the ^{60}Ni(^{7}Li,^{7}Be+γ) experiment [23] in which isovector monopole strength associated with the IVGMR was identified, show that this method is a valuable tool for further studies of the $T_z = (T + 1)$ channel. Although the presence of the continuum background makes the analysis difficult, experiments at different beam energies and using different targets could contribute to a systematic understanding of the IVGMR and possibly the SIVM.

It should be mentioned that in principle the study of SIVM and IVGMR in the $T_z = +1$ direction ((n,p)-like reactions) is easier than the study in the reverse direction. This is due to the fact that the excitation energy is lower and thus also the spreading width, since the density of states increases with excitation energy. The (t,^{3}He) reaction would be a good candidate, not only to study the SIVM and IVGMR, but (spin-)isospin modes in general. Experiments using this reaction (E(triton)=381 MeV) with promising results have been performed already at the National Superconducting Cyclotron Laboratory (NSCL) using a secondary triton beam [178]. Also at KVI, plans exist to perform (t,^{3}He) experiments, using a primary triton beam of approximately 180 MeV. Of course, working with a radioactive triton beam requires special safety measures and the beam intensities are low. Still, it is certainly worthwhile to attempt to study the SIVM and IVGMR (and possibly the decay by particle emission) via this reaction.

It can therefore be concluded that for the further study of the SIVM and its decay properties, the (^{3}He,t) reaction is an appropriate tool. The IVGMR can only be investigated indirectly by comparing results at high and low ^{3}He bombarding energies. The study of the IVGMR and SIVM through the (^{3}He,t) reaction can thus not be the sole way of investigation. For a complete picture, other probes have to be used also.

Appendix A. Wave functions

This appendix gives the wave functions, projected on a 1p-1h basis, for the various giant resonances in ^{124}Sb and ^{208}Bi. They were calculated using the program NORMOD [63] and served as input for the distorted-wave calculations in this work. In tables A.1 to A.3, the wave functions for the ^{124}Sn(^{3}He,t)^{124}Sb reaction are given. In A.4 to A.6 those for the ^{208}Pb(^{3}He,t)^{208}Bi reaction are given. Tables A.1 and A.4 refer to monopole transitions, tables A.2 and A.5 to dipole transitions and A.3 and A.6 to quadrupole transitions. The parameter X_{ph}^{JM} is defined through equations (3.38) and (3.39). In the tables the labels of X are omitted and the subscript gives the specific giant resonance for which the values are given in that column.

Table A.1: Wave functions for isovector giant monopole transitions in ^{124}Sn(^{3}He,t)^{124}Sb.

1πp	1νh	X_{SIVM}	X_{IVGMR}	X_{IAS}	X_{GTR}
$3s_{1/2}$	$2s_{1/2}$	0.1966	0.1966	-	-
$1h_{11/2}$	$0h_{11/2}$	0.2111	0.3363	-	-
$1h_{9/2}$	$0h_{11/2}$	0.2618	-	-	-
$2d_{3/2}$	$1d_{3/2}$	-0.1069	0.2391	-	-
$2d_{3/2}$	$1d_{5/2}$	0.2496	-	-	-
$2d_{5/2}$	$1d_{3/2}$	-0.2138	-	-	-
$2d_{5/2}$	$1d_{5/2}$	0.2335	0.3418	-	-
$1g_{7/2}$	$0g_{7/2}$	-0.1449	0.2846	-	-
$1g_{7/2}$	$0g_{9/2}$	0.2739	-	-	-
$1g_{9/2}$	$0g_{7/2}$	-0.2449	-	-	-
$1g_{9/2}$	$0g_{9/2}$	0.2271	0.3557	-	-
$2p_{1/2}$	$1p_{1/2}$	-0.0598	0.1795	-	-
$2p_{1/2}$	$1p_{3/2}$	0.1692	-	-	-
$2p_{3/2}$	$1p_{1/2}$	-0.1692	-	-	-
$2p_{3/2}$	$1p_{3/2}$	0.1892	0.2538	-	-
$1f_{5/2}$	$0f_{5/2}$	-0.1216	0.2493	-	-
$1f_{5/2}$	$0f_{7/2}$	0.2176	-	-	-
$1f_{7/2}$	$0f_{5/2}$	-0.2176	-	-	-
$1f_{7/2}$	$0f_{7/2}$	0.1884	0.2878	-	-
$1d_{3/2}$	$0d_{3/2}$	-0.0803	0.1795	-	-
$1d_{3/2}$	$0d_{5/2}$	0.1605	-	-	-
$2s_{1/2}$	$1s_{1/2}$	0.1517	0.1517	-	-
$1d_{5/2}$	$0d_{3/2}$	-0.1605	-	-	-
$1d_{5/2}$	$0d_{5/2}$	0.1502	0.2198	-	-
$1d_{3/2}$	$1d_{3/2}$	-	-	0.2945	-0.1320
$1d_{5/2}$	$1d_{3/2}$	-	-	-	-0.2639
$1d_{3/2}$	$1d_{5/2}$	-	-	-	0.3080
$2s_{1/2}$	$2s_{1/2}$	-	-	0.2243	0.2247
$0h_{11/2}$	$0h_{11/2}$	-	-	0.4875	0.3065
$0h_{9/2}$	$0h_{11/2}$	-	-	-	0.3802
$1d_{5/2}$	$1d_{5/2}$	-	-	0.4211	0.2881
$0g_{7/2}$	$0g_{7/2}$	-	-	0.4485	-0.2288
$0g_{7/2}$	$0g_{9/2}$	-	-	0.4485	0.4323

Table A.2: Wave functions for isovector giant dipole transitions in ^{124}Sn(^{3}He,t)^{124}Sb.

1πp	1νh	$X_{SDR,2^-}$	$X_{SDR,1^-}$	$X_{SDR,0^-}$	X_{IVGDR}
$1g_{7/2}$	$0h_{11/2}$	-0.1360	-	-	-
$1g_{9/2}$	$0h_{11/2}$	-0.0867	-0.0892	-	-0.1340
$0i_{11/2}$	$0h_{11/2}$	0.1558	-0.3385	0.4520	-0.0424
$2p_{1/2}$	$1d_{3/2}$	0.0236	0.0653	-	-0.0981
$2p_{1/2}$	$1d_{5/2}$	-0.1349	-	-	-
$2p_{1/2}$	$2s_{1/2}$	-	-0.1315	0.1526	-0.0988
$2p_{3/2}$	$2s_{1/2}$	0.1681	-0.0930	-	0.1397
$2p_{3/2}$	$1d_{3/2}$	0.0472	0.1168	0.1515	-0.0439
$2p_{3/2}$	$1d_{5/2}$	-0.1262	-0.1022	-	-0.1536
$1f_{5/2}$	$1d_{3/2}$	-0.0695	0.1314	-	0.1974
$1f_{5/2}$	$1d_{5/2}$	0.1082	-0.2459	0.3248	-0.0616
$1f_{5/2}$	$0g_{7/2}$	0.0480	0.0797	-	-0.1197
$1f_{5/2}$	$0g_{9/2}$	-0.1519	-	-	-
$1f_{7/2}$	$1d_{3/2}$	-0.2271	-	-	-
$1f_{7/2}$	$1d_{5/2}$	0.1988	-0.1833	-	0.2753
$1f_{7/2}$	$0g_{7/2}$	0.0555	0.1227	0.1631	-0.0230
$1f_{7/2}$	$0g_{9/2}$	-0.1028	-0.1015	-	-0.1524
$1d_{3/2}$	$1p_{1/2}$	-0.0376	0.1040	-	0.1562
$1d_{3/2}$	$1p_{3/2}$	0.0752	-0.1860	0.2413	-0.0698
$1d_{3/2}$	$0f_{5/2}$	0.0395	0.0746	-	0.1120
$1d_{3/2}$	$0f_{7/2}$	-0.01289	-	-	-
$0i_{13/2}$	$0h_{11/2}$	0.2337	-0.2475	-	0.3719
$0h_{9/2}$	$0g_{7/2}$	-0.1372	0.2128	-	0.3197
$0h_{9/2}$	$0g_{9/2}$	0.1640	-0.3587	0.4782	-0.0539
$2s_{1/2}$	$1p_{3/2}$	-0.1421	-0.0786	-	-0.1181
$2s_{1/2}$	$1p_{1/2}$	-	0.1111	0.1290	-0.0835
$0h_{11/2}$	$0g_{7/2}$	-0.3594	-	-	-
$0h_{11/2}$	$0g_{9/2}$	0.2561	-0.2636	-	0.3960
$1d_{5/2}$	$1p_{1/2}$	-0.1841	-	-	-
$1d_{5/2}$	$1p_{3/2}$	0.1722	-0.1395	-	0.2095
$1d_{5/2}$	$0f_{5/2}$	0.0526	0.1195	0.1579	-0.0299
$1d_{5/2}$	$0f_{7/2}$	-0.0966	-0.0891	-	-0.1339
$0g_{7/2}$	$0h_{11/2}$	-0.3189	-	-	-
$0g_{7/2}$	$0f_{5/2}$	-0.1139	0.1890	-	0.2840
$0g_{7/2}$	$0f_{7/2}$	-0.1315	-0.2910	0.3869	-0.0547

Table A.3: Wave functions for IVGQR in ^{124}Sn(^{3}He,t)^{124}Sb.

1πp	1νh	X_{IVGQR}	1πp	1νh	X_{IVGQR}
$3s_{1/2}$	$1d_{3/2}$	0.0541	$0i_{13/2}$	$0g_{9/2}$	0.3734
$3s_{1/2}$	$1d_{5/2}$	0.0774	$0h_{9/2}$	$0f_{5/2}$	0.2502
$1h_{11/2}$	$0h_{11/2}$	-0.1032	$0h_{9/2}$	$0f_{7/2}$	-0.0616
$2d_{3/2}$	$2s_{1/2}$	-0.0945	$2s_{1/2}$	$0d_{3/2}$	0.0376
$2d_{3/2}$	$1d_{3/2}$	-0.0663	$2s_{1/2}$	$0d_{5/2}$	0.0461
$2d_{3/2}$	$1d_{5/2}$	0.0597	$0h_{11/2}$	$0f_{7/2}$	0.2822
$2d_{3/2}$	$0g_{7/2}$	0.0540	$1d_{5/2}$	$0d_{3/2}$	-0.0326
$2d_{5/2}$	$2s_{1/2}$	0.1157	$1d_{5/2}$	$0d_{5/2}$	-0.0625
$2d_{5/2}$	$1d_{3/2}$	-0.0434	$1d_{5/2}$	$1s_{1/2}$	0.0964
$2d_{5/2}$	$1d_{5/2}$	-0.1013	$0g_{7/2}$	$0d_{3/2}$	0.1693
$2d_{5/2}$	$1g_{7/2}$	0.0180	$0g_{7/2}$	$0d_{5/2}$	-0.0564
$2d_{5/2}$	$1g_{9/2}$	0.0711	$0j_{15/2}$	$0h_{11/2}$	0.3749
$1g_{7/2}$	$0g_{7/2}$	-0.0861	$0j_{13/2}$	$0h_{11/2}$	-0.0565
$1g_{7/2}$	$0g_{9/2}$	0.0290	$2f_{7/2}$	$0h_{11/2}$	0.0637
$1g_{7/2}$	$1d_{3/2}$	0.1763	$1h_{9/2}$	$0h_{11/2}$	0.0225
$1g_{7/2}$	$1d_{5/2}$	-0.0686			
$1g_{9/2}$	$0g_{7/2}$	-0.0260			
$1g_{9/2}$	$0g_{9/2}$	-0.1086			
$1g_{9/2}$	$1d_{5/2}$	0.2426			
$0i_{11/2}$	$0g_{7/2}$	0.3034			
$0i_{11/2}$	$0g_{9/2}$	-0.0665			
$2p_{1/2}$	$0f_{5/2}$	0.0461			
$2p_{1/2}$	$1p_{1/3}$	0.0704			
$2p_{3/2}$	$1p_{3/2}$	-0.0704			
$2p_{3/2}$	$1p_{1/2}$	-0.0704			
$2p_{3/2}$	$0f_{5/2}$	0.0246			
$2p_{3/2}$	$0f_{7/2}$	0.0603			
$1f_{5/2}$	$0f_{5/2}$	-0.0739			
$1f_{5/2}$	$0f_{7/2}$	0.0302			
$1f_{5/2}$	$1p_{3/2}$	-0.0691			
$1f_{5/2}$	$1p_{1/2}$	0.1293			
$1f_{7/2}$	$0f_{5/2}$	-0.0302			
$1f_{7/2}$	$0f_{7/2}$	-0.0871			
$1f_{7/2}$	$1p_{3/2}$	0.1693			
$1d_{3/2}$	$0d_{3/2}$	-0.0498			
$1d_{3/2}$	$0d_{5/2}$	0.0326			
$1d_{3/2}$	$1s_{1/2}$	-0.0787			

Table A.4: Wave functions for isovector giant monopole transitions in ^{208}Pb(^{3}He,t)^{208}Bi.

1πp	1νh	X_{SIVM}	X_{IVGMR}	X_{IAS}	X_{GTR}
$1f_{7/2}$	$0f_{7/2}$	0.1450	0.2124	-	-
$1f_{7/2}$	$0f_{5/2}$	-0.1675	-	-	-
$1f_{5/2}$	$0f_{7/2}$	0.1675	-	-	-
$1f_{5/2}$	$0f_{5/2}$	-0.0936	0.1839	-	-
$2p_{3/2}$	$1p_{3/2}$	0.1456	0.1873	-	-
$2p_{3/2}$	$1p_{1/2}$	-0.1303	-	-	-
$2p_{1/2}$	$1p_{3/2}$	0.1303	-	-	-
$2p_{1/2}$	$1p_{1/2}$	-0.0461	0.1325	-	-
$2d_{5/2}$	$1d_{5/2}$	0.1854	0.2601	-	-
$2d_{5/2}$	$1d_{3/2}$	-0.1982	-	-	-
$1g_{7/2}$	$0g_{9/2}$	0.2108	-	-	-
$1g_{7/2}$	$0g_{7/2}$	-0.1247	0.2348	-	-
$3s_{1/2}$	$2s_{1/2}$	0.1692	0.1622	-	-
$2d_{3/2}$	$1d_{5/2}$	0.1982	-	-	-
$2d_{3/2}$	$1d_{3/2}$	-0.0991	0.2124	-	-
$1h_{11/2}$	$0h_{11/2}$	0.2047	0.3126	-	-
$1h_{11/2}$	$0h_{9/2}$	-0.2539	-	-	-
$1g_{9/2}$	$0g_{9/2}$	0.1748	0.2625	-	-
$1g_{9/2}$	$0g_{7/2}$	-0.2108	-	-	-
$1h_{9/2}$	$0h_{11/2}$	0.2539	-	-	-
$1h_{9/2}$	$0h_{9/2}$	-0.1555	0.2854	-	-
$3p_{3/2}$	$2p_{3/2}$	0.2023	0.2601	-	-
$3p_{3/2}$	$2p_{1/2}$	-0.1809	-	-	-
$3p_{1/2}$	$2p_{3/2}$	0.1809	-	-	-
$3p_{1/2}$	$2p_{1/2}$	-0.0640	0.1839	-	-
$2f_{7/2}$	$1f_{7/2}$	0.2268	0.3321	-	-
$2f_{7/2}$	$1f_{5/2}$	-0.2619	-	-	-
$2f_{5/2}$	$1f_{7/2}$	0.2619	-	-	-
$2f_{5/2}$	$1f_{5/2}$	0.1464	0.2876	-	-
$1i_{13/2}$	$0i_{13/2}$	-0.2347	0.3627	-	-
$0h_{9/2}$	$0h_{11/2}$	-	-	-	0.4066
$0h_{9/2}$	$0h_{9/2}$	-	-	0.4767	-0.2490
$0i_{13/2}$	$0i_{13/2}$	-	-	0.5641	0.3498
$1f_{7/2}$	$1f_{7/2}$	-	-	0.4264	0.2791
$1f_{7/2}$	$1f_{5/2}$	-	-	-	-0.3223
$1f_{5/2}$	$1f_{5/2}$	-	-	0.3693	-0.1802
$1f_{5/2}$	$1f_{7/2}$	-	-	-	0.3223
$2p_{3/2}$	$2p_{3/2}$	-	-	0.3015	0.2247
$2p_{3/2}$	$2p_{1/2}$	-	-	-	-0.2010
$2p_{1/2}$	$2p_{1/2}$	-	-	0.2132	-0.0711
$2p_{1/2}$	$2p_{3/2}$	-	-	-	0.2010
$0h_{11/2}$	$0h_{13/2}$	-	-	-	0.4425

Table A.5: Wave functions for isovector giant dipole transitions in ^{208}Pb(^{3}He,t)^{208}Bi.

1πp	1νh	$X_{SDR,2^-}$	$X_{SDR,1^-}$	$X_{SDR,0^-}$	X_{IVGDR}
$0h_{9/2}$	$0g_{9/2}$	0.1300	-0.2850	0.3841	-0.4260
$0h_{9/2}$	$0g_{7/2}$	-0.1216	0.1890	-	0.2826
$0h_{9/2}$	$0i_{13/2}$	-0.3809	-	-	-
$0i_{13/2}$	$0h_{11/2}$	0.2332	-0.2478	-	0.3705
$0i_{13/2}$	$0h_{9/2}$	-0.3809	-	-	-
$1f_{7/2}$	$0g_{9/2}$	-0.0815	-0.0806	-	-0.1205
$1f_{7/2}$	$0g_{7/2}$	0.0491	0.1090	0.1455	-0.0204
$1f_{7/2}$	$1d_{5/2}$	0.1624	-0.1502	0.2637	0.2245
$1f_{7/2}$	$1d_{3/2}$	-0.2166	-	-	-
$1f_{5/2}$	$0g_{9/2}$	-0.1203	-	-	-
$1f_{5/2}$	$0g_{7/2}$	0.0425	0.0708	-	-0.1059
$1f_{5/2}$	$1d_{5/2}$	0.0884	-0.2015	-	-0.0502
$1f_{5/2}$	$1d_{3/2}$	-0.0663	-0.1257	-	0.1879
$2p_{3/2}$	$1d_{5/2}$	-0.1031	-0.0838	-	-0.1252
$2p_{3/2}$	$1d_{3/2}$	0.0450	0.1117	0.1455	-0.0417
$2p_{3/2}$	$2s_{1/2}$	0.1489	-0.0826	-	0.1235
$2p_{1/2}$	$1d_{5/2}$	-0.1103	-	-	-
$2p_{1/2}$	$1d_{3/2}$	0.0225	0.0624	-	-0.0934
$2p_{1/2}$	$2s_{1/2}$	-	-0.1168	0.1361	0.0873
$0j_{15/2}$	$0i_{13/2}$	-	-0.2861	-	0.4278
$0i_{11/2}$	$0h_{11/2}$	0.1555	-0.3389	0.4543	-0.0422
$0i_{11/2}$	$0h_{9/2}$	-0.1527	0.2277	-	0.3404
$2d_{5/2}$	$1f_{7/2}$	-0.1083	-0.1001	-	-0.1497
$2d_{5/2}$	$2p_{3/2}$	0.1547	-0.1257	-	0.1879
$2d_{5/2}$	$1f_{5/2}$	0.0589	0.1343	0.1782	-0.0335
$2d_{5/2}$	$2p_{1/2}$	-0.1654	-	-	-
$1g_{7/2}$	$0h_{11/2}$	-0.1357	-	-	-
$1g_{7/2}$	$1f_{7/2}$	0.1152	-0.2556	0.3412	-0.0478
$1g_{7/2}$	$0h_{9/2}$	0.0518	0.0806	-	-0.1205
$1g_{7/2}$	$1f_{5/2}$	-0.0998	0.1660	-	0.2482
$3s_{1/2}$	$2p_{3/2}$	-0.1378	-0.0765	-	-0.1143
$3s_{1/2}$	$2p_{1/2}$	-	0.1081	0.1260	-0.0808
$2d_{3/2}$	$1f_{7/2}$	-0.1444	-	-	-
$2d_{3/2}$	$2p_{3/2}$	0.0675	-0.1675	0.2182	-0.0626
$2d_{3/2}$	$1f_{5/2}$	0.0442	0.0838	-	-0.1252
$2d_{3/2}$	$2p_{1/2}$	-0.0388	0.0937	-	0.1400
$1h_{11/2}$	$0i_{13/2}$	-0.0915	-0.0972	-	-0.1453
$1g_{9/2}$	$0h_{11/2}$	-0.0865	-0.0893	-	-0.1335
$1g_{9/2}$	$1f_{7/2}$	0.1910	-0.1890	-	0.2826
$1g_{9/2}$	$0h_{9/2}$	0.0554	0.1215	0.1627	-0.0182
$1g_{9/2}$	$1f_{5/2}$	-0.2882	-	-	-
$1h_{9/2}$	$0i_{13/2}$	-0.1494	-	-	-
$0j_{13/2}$	$0i_{13/2}$	0.1809	-0.3928	0.5270	-0.0419
$0j_{15/2}$	$0i_{13/2}$	0.2637	-	-	-

Table A.6: Wave functions for IVGQR in ^{208}Pb(^{3}He,t)^{208}Bi.

1πp	1νh	X_{IVGQR}	1πp	1νh	X_{IVGQR}
$0h_{9/2}$	$0f_{7/2}$	-0.0459	$1g_{9/2}$	$0g_{7/2}$	-0.0216
$0h_{1/2}$	$0f_{5/2}$	0.1864	$1g_{9/2}$	$1d_{5/2}$	0.1864
$0i_{11/2}$	$0g_{9/2}$	0.2781	$1h_{9/2}$	$0h_{11/2}$	0.0211
$1f_{7/2}$	$0f_{7/2}$	-0.0649	$1h_{9/2}$	$1f_{7/2}$	-0.0551
$1f_{7/2}$	$1p_{3/2}$	0.1262	$1h_{9/2}$	$0h_{9/2}$	-0.0880
$1f_{7/2}$	$0f_{5/2}$	-0.0225	$1h_{9/2}$	$1f_{5/2}$	0.2240
$1f_{5/2}$	$0f_{7/2}$	0.0225	$3p_{3/2}$	$1f_{7/2}$	0.0779
$1f_{5/2}$	$1p_{3/2}$	-0.0515	$3p_{3/2}$	$2p_{3/2}$	-0.0728
$1f_{5/2}$	$0f_{5/2}$	-0.0551	$3p_{3/2}$	$1f_{5/2}$	0.0318
$1f_{5/2}$	$1p_{1/2}$	0.0964	$3p_{3/2}$	$2p_{1/2}$	-0.0728
$2p_{3/2}$	$0f_{7/2}$	0.0450	$3p_{1/2}$	$2p_{3/2}$	0.0728
$2p_{3/2}$	$1p_{3/2}$	-0.0524	$3p_{1/2}$	$1f_{5/2}$	0.0595
$2p_{3/2}$	$0f_{5/2}$	0.0184	$2f_{7/2}$	$0h_{11/2}$	0.0598
$2p_{3/2}$	$1p_{1/2}$	-0.0524	$2f_{7/2}$	$1f_{7/2}$	-0.1014
$2p_{1/2}$	$1p_{3/2}$	0.0524	$2f_{7/2}$	$0h_{9/2}$	0.0130
$2p_{1/2}$	$0f_{5/2}$	0.0343	$2f_{7/2}$	$2p_{3/2}$	0.1581
$0i_{11/2}$	$0g_{9/2}$	-0.0469	$2f_{7/2}$	$1f_{5/2}$	-0.0351
$0i_{11/2}$	$0g_{7/2}$	0.2527	$2f_{5/2}$	$1f_{7/2}$	0.0351
$2d_{5/2}$	$0g_{9/2}$	0.0530	$2f_{5/2}$	$0h_{9/2}$	0.0530
$2d_{5/2}$	$0g_{7/2}$	0.0150	$2f_{5/2}$	$2p_{3/2}$	-0.0646
$2d_{5/2}$	$1d_{5/2}$	-0.0779	$2f_{5/2}$	$1f_{5/2}$	-0.0861
$2d_{5/2}$	$1d_{3/2}$	-0.0389	$2f_{5/2}$	$2p_{1/2}$	0.1208
$2d_{5/2}$	$2s_{1/2}$	0.0964	$0j_{13/2}$	$0h_{11/2}$	-0.0530
$1g_{7/2}$	$0g_{9/2}$	0.0216	$0j_{13/2}$	0h9/2	0.3248
$1g_{7/2}$	$0g_{7/2}$	-0.0717	$0j_{15/2}$	$0h_{11/2}$	0.3518
$1g_{7/2}$	$1d_{5/2}$	-0.0527	$2g_{9/2}$	$0i_{13/2}$	0.0658
$1g_{7/2}$	$1d_{3/2}$	0.1581	$0k_{17/2}$	$0i_{13/2}$	0.4309
$3s_{1/2}$	$1d_{5/2}$	0.0595	$0k_{15/2}$	$0i_{13/2}$	-0.0563
$3s_{1/2}$	$1d_{3/2}$	0.0486			
$2d_{3/2}$	$0g_{7/2}$	0.0450			
$2d_{3/2}$	$1d_{5/2}$	0.0389			
$2d_{3/2}$	$1d_{3/2}$	-0.0595			
$2d_{3/2}$	$2s_{1/2}$	-0.0787			
$1h_{11/2}$	$0h_{11/2}$	-0.0968			
$1h_{11/2}$	$1f_{7/2}$	0.2527			
$1h_{11/2}$	$0h_{9/2}$	-0.0211			
$1g_{9/2}$	$0g_{9/2}$	-0.0809			

Bibliography

[1] W. Bothe and W. Gentner, Z. Phys. **106**, 236 (1937).

[2] A.B. Migdal, J. Phys. USSR **8**, 331 (1944).

[3] G.C. Baldwin and G.S. Klaiber, Phys. Rev. **71**, 3 (1947).

[4] M. Goldhaber and E. Teller, Phys. Rev. **74**, 1046 (1948).

[5] H. Steinwedel and J.H.D. Jensen, Z. Naturforschung **5a**, 413 (1950).

[6] J.P. Elliot and B.H. Flowers, Proc. Roy. Soc. A **242**, 57 (1957).

[7] G.E. Brown and M. Bolsterli, Phys. Rev. Lett **3**, 472 (1959).

[8] J.S. Levinger, *Nuclear Photo Disintegration* (Oxford University Press, Oxford, 1960).

[9] B.L. Berman and S.C. Fultz, Rev. Mod. Phys. **47**, 713 (1975).

[10] J. Speth, J Wambach, A. van der Woude, K.T. Knöpfle, G.J. Wagner, S. Raman, L.W. Fagg, R.S. Hicks, and F. Osterfeld, in *Electric and magnetic giant resonances in nuclei*, Vol. 7 of *International Reviev of Nuclear Physics*, edited by J. Speth (World Scientific, Singapore, 1991).

[11] M. Buenerd, Jour. Phys. **A45**, C4 (1984).

[12] F.E. Bertrand, Nucl. Phys. **A354**, 129c (1981).

[13] A. van der Woude, Prog. Part. Nucl. Phys. **18**, 217 (1987).

[14] M.N. Harakeh, in *Proceedings of the XVII Masurian International Summer School on Nuclear Physics*, edited by Z. Wilhelmi, G. Szetlinska, and M. Kicinska-Habior (Harwood Academic Publisher, Mikołajki, Poland, 1985), p. 463.

[15] J.P. Blaizot, Phys. Rep. **64**, 171 (1980).

[16] J. Treiner, H. Krivine, O. Bohigas, and J. Martorell, Nucl. Phys. **A371**, 253 (1981).

[17] N.K. Glendenning, Phys. Rev. C **37**, 2733 (1988).

[18] W.G. Love and M.A. Franey, Phys. Rev. C **24**, 1073 (1981).

[19] F. Osterfeld, Rev. Mod. Phys. **64**, 491 (1992).

[20] A. Erell, J. Alster, J. Lichtenstadt, M.A. Moinester, J.D. Bowman, M.D. Cooper, F. Irom, H.S. Matis, E. Piasetzky, U. Sennhauser, and A. Ingram, Phys. Rev. Lett. **52**, 2134 (1984).

[21] A. Erell, J. Alster J. Lichtenstadt, M.A. Moinester, J.D. Bowman, M.D. Cooper, F. Irom, H.S. Matis, E. Piasetzky, and U. Sennhauser, Phys. Rev. C **34**, 1822 (1986).

[22] F. Irom, J.D. Bowman, G.O. Bolme, E. Piasetzky, U. Sennhauser, J. Alster, J. Lichtenstadt, M. Moinester, J.N. Knudson, S.H. Rokni, and E.R Siciliano, Phys. Rev. C **34**, 2231 (1986).

[23] S. Nakayama, H. Akimune, Y. Arimoto, I. Daito, H. Fujimura, Y. Fujita, M. Fujiwara, K. Fushimi, H. Kohri, N. Koori, K. Takahisa, T. Takeuchi, A. Tamii, M. Tanaka, T. Yamagata, Y. Yamamoto, K. Yonehara, and H. Yoshida, Phys. Rev. Lett. **83**, 690 (1999).

[24] S. Nakayama, T. Yamagata, M. Tanaka, M. Inoue, K. Yuasa, T. Itahashi, H. Ogata, N. Koori, and K. Shima, Phys. Rev. Lett. **67**, 1082 (1991).

[25] S. Nakayama, K. Fushimi, H. Kohri, H. Akimune, I. Daito, H. Fujimura, Y. Fujita, M. Fujiwara, T. Inomata, K. Ishibashi, T. Iwasaki, N. Koori, K. Takahisa, A. Tamii, M. Tanaka, H. Toyokawa, and T. Yamagata, Nucl. Instr and Meth. A **404**, 34 (1998).

[26] T.D. Ford, J.L. Romero, F.P. Brady, C.M. Castaneda, J.R. Drummond, B. McEachern, D.S. Sorenson, Zin Aung, N.S.P. King, A. Klein, and W.G. Love, Phys. Lett. **B195**, 311 (1987).

[27] C. Bérat, M. Buénerd, J.Y. Hostachy, P. Martin, J. Barrette, B. Berthier, B. Fernandez, A. Miczaïka, A. Villari, H.G. Bohlen, S. Kubono, E. Stiliaris, and W. von Oertzen, Nucl. Phys. **A555**, 455 (1993).

[28] I. Lhenry, Nucl. Phys. **A599**, 245c (1996).

[29] W. von Oertzen, Nucl. Phys. **A482**, 357c (1988).

[30] C. Ellegaard, C. Gaarde, J.S. Larsen, C. Goodman, I. Bergqvist, L. Carlén, L.P. Ekström, B. Jakobsson, J. Lyttkens, M. Bedjidian, M. Chamcham, J.Y. Grossiord, A. Guichard, M. Gusakow, R. Haroutunian, J.R. Pizzi, D. Bachelier, J.L. Boyard, T. Hennino, J.C. Jourdain, M. Roy-Stephan, M. Boivin, and P. Radvanyi, Phys. Rev. Lett. **50**, 1745 (1983).

[31] N. Auerbach, F. Osterfeld, and T. Udagawa, Phys. Lett. **B219**, 184 (1989).

[32] D.L. Prout *et al.*, in *Proceedings of the Eighth International Symposium on Polarization Phenomena in Nuclear Physics*, Vol. **339** of *AIP Conf. Proc.*, edited by E.J. Stephenson and S.E. Vigdor (AIP Press, New York, 1995), p. 458.

[33] N. Auerbach and A. Klein, Nucl. Phys. **A395**, 77 (1983).

[34] N. Auerbach and A. Klein, Phys. Rev. C **28**, 2075 (1983).

[35] S. Adachi and N. Auerbach, Phys. Lett. **131B**, 11 (1983).

[36] N. Auerbach and A. Klein, Phys. Rev. C **30**, 1032 (1984).

[37] M.N. Harakeh, H. Akimune, I. Daito, Y. Fujita, M.B. Greenfield, T. Inomata, J. Jänecke, K. Katori, S. Nakayama, H. Sakai, Y. Sakemi, M. Tanaka, and M. Yosoi, Nucl. Phys. **A577**, 57c (1994).

[38] H. Akimune, I. Daito, Y. Fujita, M. Fujiwara, M.B. Greenfield, M.N. Harakeh, T. Inomata, J. Jänecke, K. Katori, S. Nakayama, H. Sakai, Y. Sakemi, M. Tanaka, and M. Yosoi, Phys. Rev. C **52**, 604 (1995).

[39] Akimune et al., to be published.

[40] A. Bohr and B.R. Mottelson, *Nuclear Structure, Vol 2* (W.A. Benjamin, inc., New York, 1975).

[41] D. Vautherin and D.M. Brink, Phys. Rev. C **5**, 626 (1972).

[42] A. Bohr and B.R. Mottelson, *Nuclear Structure, Vol 1* (W.A. Benjamin, inc., New York, 1969).

[43] J.D. Bowman, E. Lipparini, and S. Stringari, Phys. Lett. **197**, 497 (1987).

[44] M.N. Harakeh, Internal Report **KVI-77**, (1981), KVI (unpublished).

[45] N. Auerbach and A. Yeverechyahu, Ann. Phys. (N.Y.) **95**, 35 (1975).

[46] M.N. Harakeh, Private Communication.

[47] K. Goeke and J. Speth, Ann. Rev. Nucl. Part. Sci. **32**, 65 (1982).

[48] P.J. Siemens and A.S. Jensen, *Elements of Nuclei* (Addison-Wesley Publishing Company, Inc., Reading, Massachusetts, 1987).

[49] S. Krewald, S.J. Birkhold, A. Faessler, and J. Speth, Phys. Rev. Lett. **33**, 1386 (1974).

[50] J. Sawicki, Phys. Rev. **126**, 2231 (1962).

[51] D. F. Jackson, *Nuclear Reactions* (Methuen and Co LTD., London, 1970).

[52] G.R. Satchler, *Direct Nuclear Reactions* (Clarendon Press, Oxford, 1983).

[53] V.A. Madsen, Nucl. Phys. **80**, 177 (1966).

[54] J. Raynal, Nucl. Phys. **A97**, 572 (1967).

[55] P. Grasdijk, Ph.D. thesis, Rijksuniversiteit Groningen, (1986), unpublished.

[56] N. Willis, I. Brissaud, Y. le Bornec, B. Tatischeff, and G. Duhamel, Nucl. Phys. **A204**, 454 (1973).

[57] S.Y. van der Werf, S. Brandenburg, P. Grasdijk, W.A. Sterrenburg, M.N. Harakeh, M.B. Greenfield, B.A. Brown, and M. Fujiwara, Nucl. Phys. **A496**, 305 (1989).

[58] W.T. Pinkston and G.R. Satchler, Nucl. Phys. **A388**, 61 (1982).

[59] R. Schaeffer, Nucl. Phys **A164**, 145 (1971).

[60] R. Schaeffer, Nucl. Phys. **A158**, 321 (1970).

[61] R. Schaeffer and J. Raynal, computer code DWBA70, (1971), unpublished, extended version DW81 by J.R. Comfort (1981).

[62] M.A. Hofstee, S.Y. van der Werf, A.M. van den Berg, N. Blasi, J.A. Bordewijk, W.T.A. Borghols, R. De Leo, G.T. Emery, S. Fortier, S. Galès, M.N. Harakeh, P. den Heijer, C.W. de Jager, H. Langevin-Joliot, S. Micheletti, M. Morlet, M. Pignanelli, J.M. Schippers, H. de Vries, A. Willis, and A. van der Woude, Nucl. Phys. **A588**, 729 (1995).

[63] S.Y. van der Werf, Program NORMOD, unpublished.

[64] A. Bracco, Nucl. Phys. **A482**, 421c (1988).

[65] M.N. Harakeh, Lecture Notes in Physics **158**, 236 (1982).

[66] S. Shlomo and G. Bertsch, Nucl. Phys. **A243**, 507 (1975).

[67] K.F. Liu and N. Van Giai, Nucl. Phys. **A265**, 23 (1976).

[68] N. Van Giai and H. Sagawa, Nucl. Phys. **A371**, 1 (1981).

[69] G. Co and S. Krewald, Nucl. Phys. **A433**, 392 (1985).

[70] A. Faessler, D.J. Millener, P. Paul, and D. Strottman, Nucl. Phys. **A330**, 333 (1979).

[71] G.F. Bertsch, P.F. Bortignon, and R.A. Broglia, Rev. Mod. Phys. **55**, 287 (1983).

[72] J. Wambach, Rep. Prog. Phys. **51**, 989 (1988).

[73] G. Coló, P.F. Bortignon, N. Van Giai, A. Bracco, and R.A. Broglia, Phys. Lett. **276B**, 279 (1992).

[74] G. Coló, P.F. Bortignon, N. Van Giai, and R.A. Broglia, Phys. Rev. C **50**, 1496 (1994).

[75] G. Còlo and N. Van Giai, Phys. Rev. C **53**, 2201 (1996).

[76] S.E. Muraviev and M.H. Urin, Nucl. Phys. **A572**, 267 (1994).

[77] O.A. Rumyantsev and M.H. Urin, Phys. Rev. C **49**, 537 (1994).

[78] E.A. Moukhai, V.A. Rodin, and M.H. Urin, Phys. Lett. **447B**, 8 (1999).

[79] E. Moukhai and M.H. Urin, (1998), private communication.

[80] W.T.A. Borghols, Ph.D. thesis, Rijksuniversiteit Groningen, (1988), unpublished.

[81] S. Brandenburg, W.T.A. Borghols, A. Drentje, A. van der Woude, M.N. Harakeh, L.P. Ekström, L. Nilsson A. Håkanson, N. Olsson, and R. De Leo, Phys. Rev. C **39**, 2448 (1989).

[82] S. Brandenburg, Ph.D. thesis, Rijksuniversiteit Groningen, (1985), unpublished.

[83] F. Zwarts, A.G. Drentje, M.N. Harakeh, and A. van der Woude, Nucl. Phys. **A439**, 117 (1985).

[84] K.T. Knöpfle, H. Riedesel, K. Schindler, G.J. Wagner, C. Mayer-Böricke, W. Oelert, M. Rogge, and P. Turek, Lecture Notes in Physics **92**, 444 (1979).

[85] K.T. Knöpfle, Lecture Notes in Physics **108**, 311 (1979).

[86] F. Pühlhofer, Nucl. Phys. **A280**, 267 (1977).

[87] F. Pühlhofer, computer code CASCADE, (1979), unpublished.

[88] W. Hauser and H. Feshbach, Phys. Rev. **87**, 366 (1952).

[89] J. Grover and J. Gilat, Phys. Rev. **157**, 802 (1967).

[90] T.D. Thomas, Nucl. Phys. **53**, 558 (1964).

[91] J.M. Blatt and V.F. Weisskopf, *Theoretical Nuclear Physics* (Wiley, New York, 1952).

[92] R.R. Kinsey, Nudat Program for Nuclear Data Sheets, version 2.5, http://www.nndc.bnl.gov/nndc/nudat, 1996, national nuclear data center, Brookhaven National Laboratory.

[93] E. Gadioli and R. Zetta, Phys. Rev. **167**, 1016 (1968).

[94] E. Erba, U. Facchini, and E. Saetta-Menichella, Nuovo Cim. **22**, 1237 (1961).

[95] H. Vonach and M. Hille, Nucl. Phys. **A127**, 289 (1969).

[96] W. Dilg, W. Schantl, H. Vonach, and M. Uhl, Nucl. Phys. **A217**, 269 (1973).

[97] W.D. Myers, *Droplet model of atomic nuclei* (IFI/PLENUM, New York, 1977).

[98] N. Auerbach, Nucl. Phys. **A182**, 247 (1972).

[99] M.A. Preston and R.K. Bhaduri, *Structure of the Nucleus* (Addison-Wesley Publishing Company, Inc., Reading, Massachusetts, 1975).

[100] W.D. Myers and W.J. Swiatecki, Nucl. Phys. **81**, 1 (1966).

[101] K. Ikeda, S. Fujii, and J.I. Fujita, Phys. Lett. **3**, 271 (1963).

[102] C.D. Goodman, C.A. Goulding, M.B. Greenfield, J. Rapaport, D.E. Bainum, C.C. Foster, W.G. Love, and F. Petrovich, Phys. Rev. Lett. **44**, 1755 (1980).

[103] C. Gaarde, J. Rapaport, T.N. Taddeucci, C.D. Goodman, C.C. Foster, D.E. Bainum, C.A. Goulding, M.B. Greenfield, D.J. Horen, and E. Sugarbaker, Nucl. Phys. **A369**, 258 (1981).

[104] M. Ericson, A. Figureau, and C. Thévenet, Phys. Lett. **B45**, 19 (1973).

[105] K. Shimizu, M. Ichimura, and A. Arima, Nucl. Phys. **A226**, 282 (1974).

[106] H. Hyuga, A. Arima, and K. Shimizu, Nucl. Phys. **A336**, 363 (1980).

[107] A. Arima, Nucl. Phys. **A649**, 260c (1999).

[108] F. Osterfeld, D. Cha, and J. Speth, Phys. Rev. C **31**, 372 (1985).

[109] T. Wakasa, H. Sakai, H. Okamura, H. Otsu, S. Fujita, S. Ishida, N. Sakamoto, T. Uesaka, Y. Satou, M.B. Greenfield, and K. Hatanaka, Phys. Rev. C **55**, 2209 (1997).

[110] E.H.L. Aarts, Ph.D. thesis, Rijksuniversiteit Groningen, (1983), unpublished.

[111] E.H.L. Aarts, R.K. Bhowmik, R.J. de Meijer, and S.Y. van der Werf, Phys. Lett. **102B**, 307 (1981).

[112] O. Bousshid, H. Machner, C. Alderliesten, U. Bechstedt, A. Djaloeis, P. Jahn, and C. Mayer-Böricke, Phys. Rev. Lett. **45**, 980 (1980).

[113] S. Gopal, A. Djaloeis, J. Bojowald, O. Bousshid, W. Oelert, N.G. Puttaswamy, P. Turek, and C. Mayer-Böricke, Phys. Rev. C **23**, 2459 (1981).

[114] J. Jänecke, K. Pham, D.A. Roberts, D. Stewart, M.N. Harakeh, G.P.A. Berg, C.C. Foster, J.E. Lisantti, R. Sawafta, E.J. Stephenson, A.M. van den Berg, S.Y. van der Werf, S.E. Muraviev, and M.H. Urin, Phys. Rev. C **48**, 2828 (1993).

[115] I. Bergqvist, A. Brockstedt, L. Carén, L.P. Ekström, B. Jakobsson, C. Ellegaard, C. Gaarde, J.S. Larsen, C. Goodman, M. Bedjidian, D. Contardo, J.Y. Grossiord, A. Guichard, R. Haroutunian, J.R. Pizzi, D. Bachelier, J.L. Boyard, T. Hennino, J.C. Jourdain, M. Roy-Stephan, M. Boivin, and P. Radvanyi, Nucl. Phys. **A469**, 648 (1987).

[116] D.L. Prout, C. Zafiratos, T.N. Taddeucci, J. Ullmann, R.C. Byrd, T.A. Carey, P. Lisowski, J.P. McClelland, L.J. Rybarcyl, W. Sailor, W. Amian, M. Braunstein, D. Lind, D.J. Mercer, D. Cooper, S. DeLucia, B. Luther, D.G. Marchlenski, E. Sugarbaker, J. Rapaport, B.K. Park, E. Gülmez, C.A. Whitten Jr., C.D. Goodman, W. Huang, D. Ciskowski, and W.P. Alford, Phys. Rev. C **52**, 228 (1995).

[117] K. Pham, J. Jänecke, D.A. Roberts, M.N. Harakeh, G.P.A. Berg, S. Chang, J. Liu, E.J. Stephenson, B.F. Davis, H. Akimune, and M. Fujiwara, Phys. Rev. C **51**, 526 (1995).

[118] C. Sükösd, C. Mayer-Böricke, M. Rogge, P. Turek, K.T. Knöpfle, H. Riedesel, K. Schindler, and G.J. Wagner, Nucl. Phys. **A467**, 365 (1987).

[119] A. Celler, S. Yen, W.P. Alford, R. Abegg, B.A. Brown, S. Burzynski, D. Frekers, O Häuser, R. Helmer, R.S. Henderson, K. Hicks, K.P. Jackson, R. Jeppesen, C.A. Miller, M.A. Moinester, B.W. Pointon, A. Trudel, and M.C. Vetterli, Phys. Rev. C. **47**, 1563 (1993).

[120] M. Danos, Nucl. Phys. **5**, 23 (1958).

[121] B. Fukuda and Y. Torizuka, Phys. Rev. Lett. **29**, 1109 (1972).

[122] H. Emling, Nucl. Phys. **A553**, 493c (1993).

[123] R. Schmidt, Th. Blaich, Th.W. Elze, H. Emling, H. Freiesleben, K. Grimm, W. Henning, R. Holzmann, J.G. Keller, H. Klinger, R. Kulessa, J.V. Kratz, D. Lambrecht, J.S. Lange, Y. Leifels, E. Lubkiewicz, E.F. Moore, E. Wajda, W. Prokopowicz, Ch. Shütter, H. Spies, K. Stelzer, J. Stroth, W. Walus, H.J. Wollersheim, M. Zinser, and E. Zude, Phys. Rev. Lett. **70**, 1767 (1993).

[124] F.E. Bertrand, J.R. Beene, and D.J. Horen, Nucl. Phys. **A482**, 287c (1988).

[125] S. Mordechai and C. F. Moore, Nature **352**, 393 (1991).

[126] J.D. Bowman, H.W. Baer, R. Bolton, M.D. Cooper, F.H. Cverna, N.S.P. King, M. Leitch, H.S. Matis, A. Erell, J. Alster, A. Doron, M.A. Moinester, E. Blackmore, and E.R. Siciliano, Phys. Rev. Lett. **50**, 1195 (1983).

[127] N. Auerbach, Comm. Nucl. Part. Phys. **22**, 223 (1998).

[128] M.N. Harakeh and A.E.L. Dieperink, Phys. Rev. C **23**, 2329 (1981).

[129] T. Udagawa, A. Schulte, and F. Osterfeld, Nucl. Phys. **A474**, 131 (1987).

[130] N. Auerbach, J.D. Bowman, M.A. Franey, and W.G. Love, Phys. Rev. C **28**, 280 (1983).

[131] M.A. Moinester, A. Trudel, K. Raywood, S. Yen, B.M. Spicer, R. Abegg, W.P. Alford, N. Auerbach, A. Celler, D. Frekers, O. Häusser, R.L. Helmer, R. Henderson, K.H. Hicks, K.P. Jackson, R.G. Jeppesen, N.S.P. King, S. Long, C.A. Miller, M. Vetterli, J. Watson, and A.I. Yavin, Phys. Lett. **B230**, 41 (1989).

[132] A.Z. Mekjian, Phys. Rev. Lett. **25**, 888 (1970).

[133] N. Auerbach, J. Hüfner, A.K. Kerman, and C.M. Shakin, Rev. Mod. Phys. **44**, 48 (1972).

[134] J. Jänecke, M.N. Harakeh, and S.Y. van der Werf, Nucl. Phys. **A463**, 571 (1987).

[135] W.M. MacDonald and M.C. Birse, Phys. Rev. C **29**, 425 (1984).

[136] M.N. Harakeh, in *Proc. 4th Int. Conf. on Nuclear Reaction Mechanisms*, edited by E. Gadioli (Ricera Scientifica Ed Educazione Permanente, Università di Milano, Varenna, Italy, 1985), p. 353.

[137] Floor plan of IUCF experimental areas, World Wide Web http://www.iucf.indiana.edu/, 1997.

[138] H.W. Schreuder, S. Brandenburg, H. Post, L.P. Roobol, and S. van der Veen, KVI Annual Report, 1997, p. 52.

[139] R.G.T. Zegers and B. Kharraja, Internal Report **206i** (1998), KVI (unpublished).

[140] G.P.A. Berg, L.C. Bland, D. DuPlantis, C.C. Foster, D.W. Miller, P. Schwandt, R. Sawafta, K. Solberg, and E. Stephenson, IUCF Annual Report, (1988), p. 223.

[141] G.P.A. Berg, S. Wells, Y. Wang, T. Hall, A. Bacher, D. Bilodeau, J. Doskow, G. East, C.C. Foster, J.E. Lisantti, T. Rinckel, P. Schwandt, and E.J. Stephenson, IUCF Annual Report, (1991), p. 221.

[142] G.P.A. Berg, C.C. Foster, E.J. Stephenson, and B.F. Davis, IUCF Annual Report, (1994), p. 106.

[143] D.L. Hendrie, in *Nuclear Spectroscopy and Reactions*, edited by J. Cerny (Academic Press, New York, 1974), Vol. part A, Chap. Magnetic detection of charged particles, p. 365.

[144] P. Schwandt, K600 lecture 1, Lecture notes, (1986).

[145] P. Schwandt, K600 lecture 2, Lecture notes, (1986).

[146] L. Bland, Detectors and Electronics of the K600 spectrometer, Lecture notes, (1987).

[147] A.M. van der Berg, Nucl. Instr. Meth. **B99**, 637 (1995).

[148] Z. Zojceski, Ph.D. thesis, l'Université Paris XI Orsay, (1997), unpublished.

[149] F.J. Lynch, IEEE Trans. Nucl. Sci. **NS-22**, 58 (1975).

[150] G. Dietze and H. Klein, Nucl. Inst. Meth. **193**, 549 (1982).

[151] N. Olsson, P.-O. Söderman, L. Nilsson, and H. Laurent, Nucl. Inst. Meth. Phys. Res. A **349**, 231 (1994).

[152] D.L. Smith, R.G. Polk, and T.G. Miller, Nucl. Inst. Meth. **64**, 157 (1968).

[153] D.A. Roberts, K. Ashktorab, F.D. Becchetti, J. Jänecke, M.N. Harakeh, S.Y. van der Werf, G.P.A. Berg, C.C. Foster, J.E. Lisantti, T. Rinckel, E.J. Stephenson, S.P. Wells, A. Nadasen, and S. Shaheen, Phys. Rev. C **52**, 1361 (1995).

[154] G. Dietze and H. Klein, computer codes NRESP4 and NEFF4, Physikalisch-Technische-Bundesanstalt Report **ND22**, (1982), updated versions NRESP7 and NEFF7(1991), unpublished.

[155] E.N.E. van Dalen, Internal Report 205I (1998), KVI (unpublished).

[156] J.F. Ziegler and J.P. Biersach, computer code TRIM, (Pergamon Press, New York, 1985).

[157] N.R. Yoder, XSYS, IUCF Data Acquisition Software, IUCF Internal Report, (1988), revised 1990, original Version by Triangle Universities Nuclear Laboratory (TUNL).

[158] E.J. Stephenson, Software routines for the data-acquisition system of the K600 spectrometer at IUCF, Private Communication, (1996).

[159] D.A. Roberts and J. Jänecke, Software routines for processing data from neutron detectors, Private Communication, (1996).

[160] R.Ö. Akyüz and S. Fallieros, Phys. Rev. Lett. **27**, 1016 (1971).

[161] P. Paul, J. Amann, and K.A. Snover, Phys. Rev. Lett. **27**, 1013 (1971).

[162] N. Auerbach and A. Yeverechyahu, Nucl. Phys. **A332**, 173 (1979).

[163] E.J. Schneid, A. Prakash, and B.L. Cohen, Phys. Rev. **156**, 1316 (1967).

[164] V.A. Kuzmin and V.G. Soloviev, J. Phys. G **11**, 603 (1985).

[165] N. Auerbach, L. Zamick, and A. Klein, Phys. Lett. **118B**, 256 (1982).

[166] Yu. V. Gaponov and Yu. S. Lyutostanskiĭ, Sov. J. Nucl. Phys. **19**, 33 (1974).

[167] G. Bertsch, D. Cha, and H. Toki, Phys. Rev. C **24**, 533 (1981).

[168] J. Jänecke *et al.*, analysis of the ^{12,13,14}C(^{3}He,t)^{12,13,14}N reactions at 200 MeV, to be published.

[169] J. Jänecke, J.A. Bordewijk, S.Y. van der Werf, and M.N. Harakeh, Nucl. Phys. **A552**, 323 (1993).

[170] J.A. Bordewijk, Ph.D. thesis, Rijksuniversiteit Groningen, 1993, unpublished.

[171] J.F. Clavelin, R. Douet, V. Hervier, A. Lesage, A. Willis, and Z. Zojceski, Data-acquisition system for the BBS focal-plane detector constructed at IPN, Orsay.

[172] N. Borome, J.F. Clavelin, P. Didelon, R. Douet, H. Harroch, N. Navarre, T. Tran-Khanh, and C. Veron, Open Acquisition System IPN Saturne, World Wide Web: http://ipnweb.in2p3.fr/ douet/.

[173] Physics Analysis Workstation, CERN Program Library, entry **Q121**, 1995.

[174] H.K.T. van der Molen, Data transformation code for experiments with the IPN Orsay focal-plane detection system, private communication.

[175] C. Gaarde, J.S. Larsen, A.G. Drentje, M.N. Harakeh, and S.Y. van der Werf, Phys. Rev. Lett. **46**, 902 (1981).

[176] G.F. Bertsch, J. Borysowicz, H. McManus, and W.G. Love, Nucl. Phys. **A284**, 399 (1977).

[177] M. Fujiwara, H. Akimune, I. Daito, H. Ejiri, Y. Fujita, M.B. Greenfield, M.N. Harakeh, R. Hazama, T. Inomata, J. Jänecke, N. Kudomi, K. Kume, S. Nakayama, K. Shinmyo, A. Tamii, M. Tanaka, H. Toyokawa, and M. Yosoi, Nucl. Phys. **A577**, 43c (1994).

[178] I. Daito, H. Akimune, Sam M. Austin, D. Bazin, G.P.A. Berg, J.A. Brown, B.S. Davids, Y. Fujita, H. Fujimura, M. Fujiwara, R. Hazama, T. Inomata, K. Ishibashi, J. Jänecke, S. Nakayama, K. Pham, D.A. Roberts, B.M. Sherrill, M. Steiner, A. Tamii, M. Tanaka, H. Toyokawa, and M. Yosoi, Phys. Lett. **418B**, 27 (1998).

Samenvatting

Het onderzoek naar reuzenrensonanties startte rond 1940 en sinds die tijd is er veel onderzoek verricht naar deze excitaties van de atoomkern, zowel op experimenteel als theoretisch gebied. In dit proefschrift worden twee experimenten beschreven die als doel hadden meer informatie te verkrijgen over twee van deze reuzenresonanties, waar tot op heden weinig experimentele informatie over beschikbaar is: de zogenaamde isovector monopool reuzenresonantie (IVGMR) en de spin-flip isovector monopool reuzenresonantie (SIVM). De voornaamste redenen om te proberen meer te weten te komen over deze reuzenresonanties ligt in het feit dat ze ons veel kunnen vertellen over de structuur van de atoomkern en eigenschappen van kernmaterie.

Reuzenresonanties zijn collectieve trillingen van de atoomkern die op betrekkelijk eenvoudige manier kunnen worden begrepen door de atoomkern te beschouwen als een vloeistofdruppel. Een reuzenresonantie kan dan worden gezien als een trilling van de vloeistofdruppel. De simpelste wijze van trilling is als het vloeistofoppervlak op één moment langs de straal naar buiten beweegt en vervolgens weer naar binnen, in een adem-achtige manier van beweging. Zo'n trilling wordt gekwalificeerd als een monopool trilling, wat betekent dat de dichtheidsverdeling tijdens de trilling sferisch symmetrisch blijft. De atoomkern bestaat echter niet uit één soort deeltjes, maar uit twee: protonen en neutronen. De 'protonvloeistof' kan in of uit fase bewegen met de 'neutronvloeistof'. In het eerste geval spreken we van een isoscalaire trilling en in het tweede geval van een isovector trilling. Deze trillingsgrondtonen zijn in figuur S.1 schematisch weergegeven.

Een verdere onderverdeling valt te maken als men beseft dat de deeltjes in de atoomkern ook nog spin hebben. Als deeltjes met verschillende spin uit fase bewegen, spreekt men van een 'spin-flip' resonantie. De IVGMR is dus een monopool trillingsgrondtoon waarbij protonen en neutronen uit fase bewegen (figuur S.1, rechts), maar waarbij de spin geen rol speelt. Het verschil met de SIVM is dat voor die reuzenresonantie dat laatste wel het geval is. De energie die nodig is om een atoomkern te laten trillen als een IVGMR of een SIVM is ongeveer hetzelfde. Behalve monopool trillingsgrondtonen zijn er ook oscillaties mogelijk, waarbij de dichtheidsverdeling niet sferisch symmetrisch is. Men spreekt dan over dipool, quadrupool enz. modes.

Isovector resonanties, waarbij de protonen en neutronen in de atoomkern dus uit fase bewegen, kunnen het best bestudeerd worden als men deze asymmetrie expliciet oplegt in de manier waarop de resonantie wordt aangeslagen. Voor de experimenten in dit proefschrift is dat gedaan door de (^{3}He,t) reactie te bestuderen. Een bundel van ^{3}He deeltjes (een ^{3}He kern bestaat uit twee protonen en één neutron) is op een trefplaat

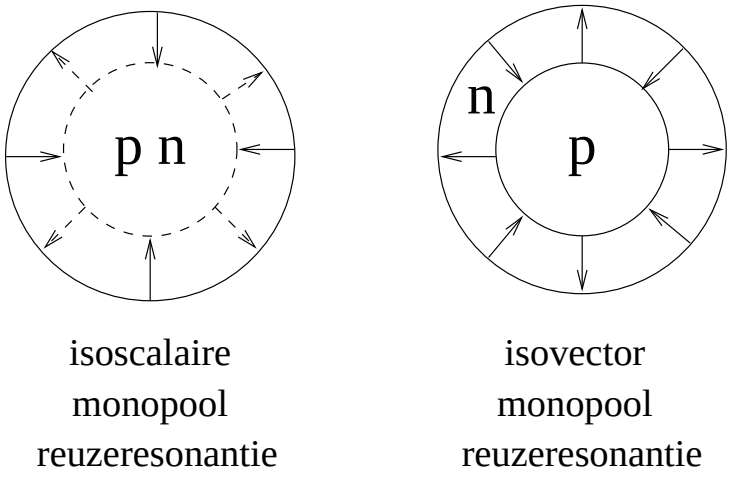

Figuur S.1: Schematische weergave van isoscalaire (links) en isovector (rechts) monopool reuzenresonaties van atoomkernen. In het isoscalaire geval bewegen de protonen (p) en neutronen (n) in fase. In de isovector trilling bewegen zij juist uit fase.

geschoten die bestaat uit de atomen waarin we de reuzenresonaties willen onderzoeken. In de experimenten die hier beschreven zijn bestond de trefplaat uit ^{124}Sn (tin) of Pb (lood). Vervolgens is gekeken naar de reacties waarbij een triton onstaat (een triton bestaat uit één proton en twee neutronen). Het inkomende deeltje heeft dan dus een proton omgewisseld met een neutron van de atoomkern in de trefplaat. Door nu te kijken naar het verschil in kinetische energie (gerelateerd aan snelheid) tussen de inkomende ^{3}He deeltjes en de uitgaande tritonen en door bovendien te meten onder welke hoek de tritonen ten opzichte van de inkomende bundel de trefplaat verlaten, kan men verschillende excitaties van de atoomkern (waaronder de reuzenresonanties) van elkaar proberen te onderscheiden.

Het grote probleem bij de bestudering van de IVGMR en SIVM is dat er ook, en met een veel hogere waarschijnlijkheid, processen plaatsvinden tijdens de reactie waarbij de kern niet als geheel wordt aangeslagen, maar waarbij wel dezelfde reactieproducten ontstaan als bij de excitatie van de atoomkern in de vorm van een reuzenresonantie. Deze fysische achtergrond, die de nucleaire continuüm achtergrond wordt genoemd, bestaat uit quasivrije processen en zogenaamde 'breakup-pickup' (oftewel 'opbreek-opneem') mechanismen. In de (^{3}He,t) reactie is een quasivrij proces voor te stellen als een één-staps interactie tussen één van de protonen in een inkomend ^{3}He deeltje en één van de neutronen uit een atoomkern in de trefplaat, en waarbij de rest van die atoomkern als spectator 'toekijkt' en onaangetast wordt door de reactie. Het 'opbreek-opneem' mechanisme is een twee-staps proces, waarbij het inkomende ^{3}He deeltje opbreekt in een proton en een deuteron (bestaande uit één proton en één neutron) ten gevolge van het veld van een atoomkern in de trefplaat. Vervolgens neemt het deuteron één neutron uit de trefplaat-atoomkern op en vormt een triton. Voor zowel het quasivrije proces als het 'opbreek-opneem' mechanisme geldt dat samen met triton ook een hoog-energetisch

(snel), sterk voorwaarts gericht (d.w.z. in de bundel richting) proton onstaat.

In de experimenten die beschreven staan in dit proefschrift is geprobeerd deze laatste eigenschap van de processen, die bijdragen tot continuüm achtergrond, te gebruiken om een onderscheid te maken met de reacties waarbij een reuzenresonantie ontstaat. Een aangeslagen atoomkern zal proberen de extra energie, ten opzichte van zijn rusttoestand (grondtoestand), die het heeft gekregen tijdens de reactie, kwijt te raken. Dat kan op verschillende manieren gebeuren. De atoomkern kan in één keer vervallen naar de grondtoestand door directe emissie van een deeltje, of de aangeslagen toestand in de atoomkern koppelt met meer complexe toestanden totdat er een statistisch evenwicht onstaat en de atoomkern stukje bij beetje de energie verliest door de emissie van deeltjes of elektromagnetische quanta (fotonen). Welke manier van verval ook plaatsvindt, voor monopool excitaties geldt dat de verdeling van de geëmitteerde deeltjes isotroop is (d.w.z. er is geen voorkeur voor een bepaalde richting). Door nu niet alleen maar de tritonen te meten, die tijdens de reactie tussen het inkomende ^{3}He deeltje en de zware atoomkern ontstaan, maar tegelijkertijd (oftewel 'in coïncidentie') vervaldeeltjes te meten in achterwaartse richting (d.w.z. tegenovergesteld aan de bundel richting) is men juist wel gevoelig voor reacties waarbij de IVGMR en de SIVM zijn aangeslagen, en veel minder voor de processen die bijdragen tot de continuüm achtergrond, omdat die juist in coincïdentie zijn met voorwaarts gerichte protonen.

Er zijn twee experimenten uitgevoerd. De eerste op het 'Indiana University Cyclotron Facility' (IUCF), waarbij coïncidenties werden vereist tussen tritonen en neutronen op achterwaartse hoeken. De trefplaat bestond uit ^{124}Sn. De reden dat besloten werd om in eerste instantie naar neutronen te kijken, was het feit dat verwacht werd dat het verval van de IVGMR en SIVM voornamelijk op statistiche wijze gebeurt. De kans is klein dat dat via emissie van protonen gebeurt, ten gevolge van de Coulomb barrière.

Het resultaat van het experiment was verrassend in de zin dat bleek dat ook processen die bijdragen tot de continuüm achtergrond voor een groot gedeelte coïncident zijn met neutronen geëmitteerd in achterwaartse richting. De verhouding tussen de continuüm achtergrond en de verwachte bijdrage ten gevolge van de SIVM en IVGMR was daarom nog steeds erg hoog en daarom bleek het onmogelijk om de reuzenresonanties te identificeren. Er zijn verschillende verklaringen mogelijk voor het feit dat een groot gedeelte van de processen die bijdragen tot de continuüm achtergrond coïncident zijn met neutronen op achterwaartse hoeken. Daarvoor moet men de atoomkern vanuit een microscopisch oogpunt bekijken, in tegenstelling tot de macroscopische beschrijving in termen van een vloeistofdruppel.

In de microscopische beschrijving van de atoomkern bevinden de protonen en neutronen zich in zogenaamde schillen. Elke schil kan slechts een beperkt aantal neutronen of protonen bevatten (ten gevolge van het zogenaamde Pauli principe). De verschillende schillen worden gekenmerkt door quantumgetallen. Aangezien er in atoomkernen, die we hier bestuderen, meer neutronen dan protonen zijn, zijn er meer schillen nodig om de neutronen te 'plaatsen'. In de (^{3}He,t) reactie, waar één neutron uit de atoomkern wordt gehaald en er één proton bijkomt, ontstaat er een gat in één van de neutronenschillen en het 'nieuwe' proton bevindt zich in een hoge protonschil. Deze deeltje-gat toestand is schematisch weergegeven in figuur S.2. Er zijn veel van dit soort deeltje-gat combinaties mogelijk. Er is in de microscopische beschrijving sprake van een reuzen-

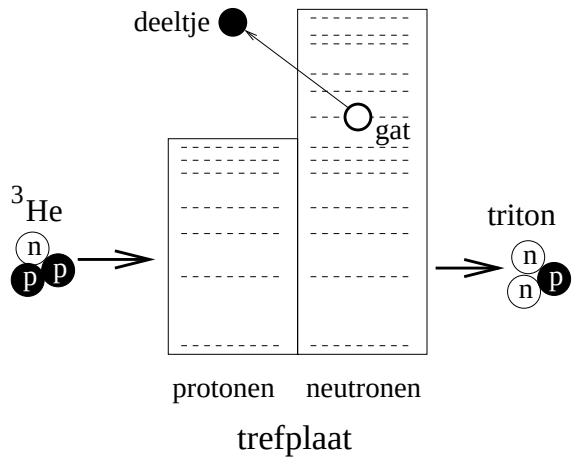

Figuur S.2: Schematische weergave van de (^{3}He,t) reactie. In een atoomkern van de trefplaat ontstaat een 'deeltje-gat' toestand. De schillen in de atoomkern zijn weergegeven door stippellijnen

resonantie als de excitaties die leiden tot deze deeltje-gat toestanden (voor een groot gedeelte) 'in fase' zijn. De combinaties die bijdragen tot een bepaalde reuzenresonantie voldoen aan een aantal eisen met betrekking tot de quantumgetallen van de schillen waarin de deeltjes zich bevinden. Men zegt dat de schil waarin het proton zich bevindt en de schil waaruit het neutron afkomstig is verbonden zijn door een 'operator' die bij de specifieke reuzenresonantie hoort.

Ook de quasivrije en 'opbreek-opneem' processen, die onderdeel zijn van de continuüm achtergrond, kunnen leiden tot bevolking van gat toestanden. Immers, één van de neutronen wordt uit de atoomkern gehaald. Er werd echter aangenomen dat de neutronen die betrokken zijn bij deze processen zich in één van de hoogste schillen bevinden. Omdat na zo'n proces de kern slechts licht geëxciteerd is (het gat zit niet erg diep), is de kans op verval door emissie van deeltjes erg klein. Als de aanname dat voornamelijk neutronen in de hoogste schillen deelnemen aan deze processen onjuist is, en dieperliggende neutronen meedoen, dan zou de excitatie energie wel hoog genoeg kunnen zijn om verval door middel van deeltjes emissie mogelijk te maken. Dit zou het geval kunnen zijn in de onderzochte kern ^{124}Sb.

Behalve deze verklaring voor de hoge vervalswaarschijnlijkheid van processen die bijdragen tot de fysische achtergrond, kan het ook zo zijn dat meer complexe processen, waarbij emissie van neutronen mogelijk is, een grotere rol spelen dan verwacht. Daarbij moet nog vermeld worden dat interpretatie bemoeilijkt wordt door het feit dat de efficiëntie voor het detecteren van neutronen afhankelijk is van de energie van de neutronen en dat daar dus voor gecorrigeerd moet worden. Als bovendien de excitatie energie van de atoomkern hoog genoeg is, kan het verval plaatsvinden door emissie van meerdere neutronen (de multipliciteit van het verval is groter dan één). Ook hiervoor is gecorrigeerd. Beide correcties kunnen leiden tot systematische fouten.

Het resultaat van het ^{124}Sn(^{3}He,tn) experiment is dus negatief in de zin dat er geen monopool sterkte is waargenomen. Berekeningen van de werkzame doorsneden van de SIVM en IVGMR (het aantal verwachte coïncidenties) toonden echter aan , dat het binnen de nauwkeurigheid van het experiment mogelijk geweest zou moeten zijn om monopool sterkte waar te nemen. Er moeten in de berekening echter een aantal aannames worden gedaan met betrekking tot de breedte van de SIVM en IVGMR en de kans dat deze resonanties vervallen door middel van neutronemissie. Als de breedte van de SIVM en IVGMR groter zijn, of de kans op verval door middel van neutronemissie lager zijn dan de aannames, is het binnen de nauwkeurigheid van het experiment niet meer geheel uit te sluiten dat er toch monopool sterkte aanwezig is.

Een tweede experiment is uitgevoerd op het Kernfysisch Versneller Instituut (KVI). Dit keer is er gekeken naar coïncidenties tussen tritonen en protonen op achterwaartse hoeken. Directe aanleiding voor het experiment was dat voor lagerliggende resonanties gebleken is dat de waarschijnlijkheid voor verval door middel van (directe) proton emissie aanzienlijk is (ongeveer 14%) en dat dus hetzelfde verwacht kan worden voor verval van de SIVM en IVGMR. Een groot voordeel bij het meten van coïncidenties met protonen, is dat er niet gecorrigeerd hoeft te worden voor detectie-efficiëntie of vervalsmultipliciteit. De trefplaat bestond uit natuurlijk voorkomend Pb.

Het bleek in dit geval wel mogelijk om de SIVM en de IVGMR te identificeren. Alhoewel er nog steeds bijdragen in de coïncidente spectra aanwezig zijn ten gevolge van quasivrije processen, is het aangetoond dat deze voor zeer achterwaartse protonhoeken en excitatie energieën, die voor de SIVM en IVGMR verwacht worden, erg klein zijn. Om het aantal coïncidenties dat gevonden is (de zogenaamde werkzame doorsnede) te vergelijken met het verwachte aantal ten gevolge van de excitatie van de SIVM en IVGMR, zijn er berekeningen verricht. In deze berekeningen is aangenomen dat alle deeltje-gat toestanden die bijdragen tot excitatie van de SIVM en IVGMR volledig in fase zijn. De overgangssterkte die men berekent onder deze aanname wordt een somregel genoemd en leidt tot een voorspelling van de maximale waarde voor de werkzame doorsnede. De vergelijking tussen de experimenteel gevonden werkzame doorsnede en de berekende waarde geeft dan aan in welke mate deze somregel is uitgeput.

De interpretatie wordt bemoeilijkt door het feit dat de waarschijnlijkheid voor verval door middel van protonemissie van de SIVM en IVGMR onbekend is. Er bleek dat, als wordt aangenomen dat de vervalswaarschijnlijkheid 20% is (wat vergelijkbaar is met de resultaten voor resonanties bij lagere excitatie energieën), de somregels voor de SIVM en IVGMR volledig uitgeput worden. Meer volledige berekeningen van de overgangssterkte tonen aan, dat de aanname dat alle deeltje-gat excitaties in fase zijn zonder rekening te houden met andere invloeden, tot een overschatting van ongeveer 50% leiden. Dat zou betekenen, dat een waarschijnlijkheid voor verval door middel van protonemissie van 40% nodig is, om de gevonden werkzame doorsnede te verklaren.

Een ander probleem is dat er bij dit experiment geen onderscheid kan worden gemaakt tussen de SIVM en de IVGMR. De twee resonanties worden, afhankelijk van de energie van de binnenkomende deeltjes, in verschillende mate aangeslagen. In de experimenten die in dit proefschrift beschreven staan, wordt verwacht dat de SIVM met ongeveer een factor 3 sterker aangeslagen wordt dan de IVGMR, maar dit kan, met behulp van de experimenten die in dit proefschrift beschreven zijn, niet gecontroleerd

worden.

Er is ook onderzocht wat de mogelijke invloed is op de gevonden werkzame doorsnede van andere resonanties waarvan een gedeelte van de sterkte zich op de zelfde excitatie energie bevindt als de IVGMR en SIVM. Het bleek dat correcties op de gevonden werkzame doorsnede in de orde van 20% niet kunnen worden uitgesloten.

Het kan dus geconcludeerd worden dat monopool sterkte geassocieerd met de SIVM en IVGMR is gevonden door bestudering van de Pb(^{3}He,tp) reactie. Onzekerheden in de vervalswaarschijnlijkheid voor protonverval maken harde uitspraken over uitputting van de somregel onmogelijk. Verval door middel van neutronemissie van processen die deel uitmaken van de continuüm achtergrond maakt het vinden van monopool sterkte via de ^{124}Sn(^{3}He,tn) reactie vrijwel onmogelijk.

Dankwoord

Als liefhebber van fantasy boeken, beeld ik me altijd graag in dat kernfysici iets weg hebben van magiërs, die proberen de materie te begrijpen, manipuleren en de meest wonderbaarlijke kunsten vertonen. In één van mijn favoriete boeken[1] sticht een groepje tovenaars op een wat afgelegen eiland een academie voor magiërs. En alhoewel het soms wat moeilijk is voor te stellen (vooral in de vroege zaterdagochtend, na de 'graveyard shift', op de fiets door de regen over de Zernikelaan), heb ik het KVI altijd een beetje vergeleken met dat eiland; en mezelf als één van de aspirant tovenaars.
Het is natuurlijk een fabeltje dat de toverkunst een gave is: dat moet je leren! En zonder de hulp van en steun van vele mensen had ik in mijn vier en een half jaar op het KVI niet een klein beetje leren toveren.

Mijn grootste dank gaat uit naar mijn promotor, Muhsin, en mijn begeleiders, Sytze en Ad. Jullie inzet, kennis en doorzettingsvermogen zijn voor mij een grote bron van inspiratie. Muhsin, ik heb het altijd bijzonder gewaardeerd dat je tussen vergaderingen, beleid en andere zaken altijd wel 'even' tijd vrijmaakte voor het beantwoorden van vragen. Sytze, de aan jou eerder gegeven bijnaam 'Lupus Instrumentalis' is zeer terecht, maar doet wat mij betreft onrecht aan je andere veelzijdige vermogens. Ad, de manier waarop jij groot experimenteel inzicht en een flinke portie optimisme en humor kunt combineren is uniek. Kortom, als leerling tovenaar had ik me geen betere en plezierigere 'meester-magiërs' kunnen wensen.

Er zijn vele anderen, van wie ik veel heb geleerd. Speciale dank ben ik verschuldigd aan Siebren van der Werf en Adriaan van der Woude, die altijd geduldig mijn vragen over reuzenresonanties en reactiemechanismen hebben beantwoord. Adriaan, and the other members of the thesis committee, Prof. Fujiwara and Prof. Heyde, I wish to thank for reading the thesis manuscript and giving useful comments and suggestions. Ook mijn 'collega-leerling' Henk wil ik speciaal bedanken, niet alleen voor de plezierige samenwerking, maar ook voor het opvullen van lacunes in mijn kennis over een wel heel speciale tak van toverkunst: data-acquisitie en software.

Het 'practicum magie' oftewel de experimenten die gedaan zijn als onderdeel van dit proefschrift waren niet zo succesvol verlopen als niet vele mensen hun handen uit de mouwen hadden gestoken. For the experiment performed at IUCF, I wish to thank my overseas colleagues Joachim Jänecke, Ed Stephenson, George Berg, Don Roberts, Chuck Foster, Tom Rinckel, Tom O'Donnell, Salam Shaheen and the cyclotron crew for the pleasant cooperation and their dedication. Special thanks go to Joachim, for

[1] *Magician*, door R.E. Feist

the many interesting discussions about the analysis and outcome of the experiment, and Ed, for patiently answering my question about the K600 spectrometer.

The experiment at KVI could never have been performed without the support and excellent efforts from Henri Laurent, Alain Willis and Jacques Guillot from Orsay. Merci beaucoup! De nog niet genoemde leden van de 'faculteit spectrometrie' (of korter: de BBS-club), Hans, Volker, Fabrice en Kjelt wil ik niet alleen bedanken voor hun inzet en hulp tijdens het experiment maar ook voor de plezierige samenwerking. Dat laatste geldt natuurlijk ook voor de latere leden van de BBS-club, Vladimir en Mark. De operateurs en technici van het cyclotron wil ik bedanken voor hun magie op het gebied van deeltjesversnelling en bundelgeleiding, zonder welke er voor de experimentatoren weinig te toveren valt.

Dat laatste geld natuurlijk ook voor alle andere mensen op het KVI die, of het nu gaat om administratie, vacuumtechniek, mechanish werk, financiën, electronica, software, fysica en alle andere zaken die bij onderzoek komen kijken, altijd bereid waren om te helpen. In het bijzonder wil ik Lambertus Slatius en Roelof-Jan Dussel bedanken, die de eerste schetsen voor de 'Silicon Ball' hebben weten om te toveren tot een (uit)blinkende detector.

Ook wil ik mijn dank uitspreken aan de leden van de OR 1997-1998 en PV 'de Kern', met wie het leuk was om te werken. Dat geld speciaal voor Frits, met wie ik vele uren in de trein op weg naar de COR vergaderingen in Utrecht heb doorgebracht. Mijn mede-OIO's wil ik bedanken voor een goede tijd en de morele ondersteuning. Met mijn kamergenoten, Sjirk en daarna Teake, was het altijd prima vertoeven. Bedankt!

Er zijn natuurlijk ook vele mensen buiten het KVI en de kernfysica die op hun eigen manier aan mijn onderzoek hebben bijgedragen, ook al vroegen zij zichzelf soms ongetwijfeld af wat ik nou eigenlijk precies uitvoerde. Ik kan hier niet iedereen persoonlijk bedanken, maar zonder jullie steun was het allemaal niet zover gekomen.

Seger, soms lijkt er geen groter verschil mogelijk dan tussen het runnen van een eigen bedrijf en het doen van promotie onderzoek, maar ik realiseer me: niets is minder waar. Bedankt voor je support.

Robert en Paul, zonder dagen vol kick-off, avonden in 'de Vestibule' en nachten op de Weekend of Terror, zonder films, boeken en filosofie boven het bierglas en zonder het 'traditioneel' stukzitten, was het allemaal van geen waarde geweest: '...the point being that we know what IT is and we know TIME and we know that everything is really FINE'[2].

Door en Sjraar, dit proefschrift is aan jullie opgedragen, alhoewel geen woorden, formules en grafieken kunnen uitdrukken wat jullie voor me betekenen. De magie zit tussen de regels!

And after all these pages full of ink, I must admit that the wisest thing is not written down. Without you, Sue Chin, even the most powerfull magic is without colour.

[2]uit *On the Road* door J. Kerouac